POLITECNICO DI TORINO

Department of Mechanical and Aerospace Engineering

Master’s Degree in Biomedical Engineering

Bionanotechnologies

Study of human lactate dehydrogenase-based microreactors for anticancer drugs screening

Supervisors

Prof. Piumetti Marco

Dr. Vincenzi Chiara

Candidate

Macchello Chiara 310303

Academic Year 2024/2025

Table of contents

1. Introduction

1.1 Overview on the current cancer therapies

Cancer is among the leading causes of death worldwide. The International Agency for Research on Cancer estimates that in twenty years the rates of incidence and mortality of cancer are projected to increase by 63% and 74%, respectively [1]. The statics are shown in Figure 1.

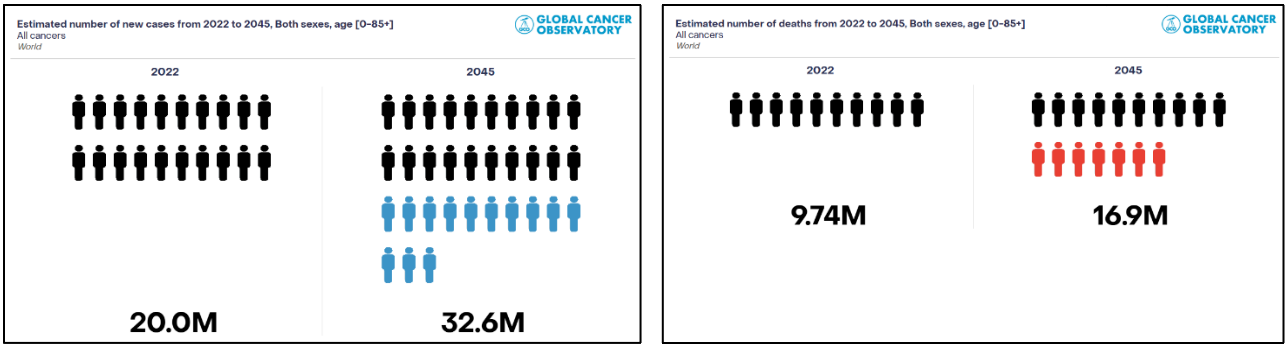

Figure 1. Visual representation of the estimated number of new cancer cases (blue) and deaths (red) from 2022 to 2045. [1]

The therapeutic approach for cancer is determined by the tumor's classification and its stage of progression. Currently the main treatment modalities can be categorized as follows [2], [3], [4]:

- Surgical intervention. Generally it involves open surgery or laparoscopic techniques. However, there are also alternative surgical methods, namely: cryosurgery, laser treatment, hyperthermia and photodynamic therapy. A primary limitation of surgical approaches is the potential inability to eradicate microscopic residual disease at the tumor margins and to remove metastasis spread in distant sites.
- Radiation therapy. It exploits high-energy radiation, primarily X-rays, to damage cancer cells' DNA, with the aim of triggering apoptosis, necrosis and senescence of tumor cells. However, radiotherapy may cause a collateral damage to adjacent healthy tissues. Moreover, it can't eradicate all neoplastic cells and it is not suitable for killing cancer cells located in hypoxic regions.
- Chemotherapy. This treatment involves the systemic administration of one or more anti-cancer drugs, often in combination. The therapy is characterized by the capability to exert a cytotoxic effect. Generally, if it is used as a monotherapy, the efficacy is limited, thus it necessitates the combination with other treatment modalities to improve the treatment's outcome. Furthermore, chemotherapy is not able to deliver systematic therapy, interacting negatively with certain medications, and systemic toxicity remains a significant concern.
- Immunotherapy. It is a type of cancer treatment that supports the patient's immune system to combat cancer. Different strategies can be applied, including immune checkpoint inhibitors, T-cell transfer therapy, immune system modulators, therapeutic cancer vaccines or monoclonal antibodies. The efficacy of immunotherapy is often restricted to a subset of patients due to inter-patient variability in treatment response. Moreover, treatment resistance and a limited repertoire of well-characterized tumor-specific antigens remain significant challenges.

Although current therapeutic strategies are well-established and widely adopted, they remain largely ineffective and insufficient in combating cancer, primarily due to the inherent complexity of the disease. Moreover, it is well recognized that most of the therapies currently in use are associated with a high incidence of adverse side effects, which further compromise the already fragile condition of patients. In light of these limitations, attention is increasingly shifting toward alternative approaches. Beyond the established therapeutic modalities, novel and promising strategies are emerging, notably the investigation of new pharmacological agents targeting cancer metabolism. Indeed, tumors are not only genetic diseases, but also metabolic disorders, a concept underscored by the well-documented Warburg effect [5]. Furthermore, metabolic reprogramming is recognized as one of the main hallmarks of cancer as malignant cells exhibit a profoundly altered metabolism, compared to normal cells [6]. In this context there is a growing interest in the Lactate Dehydrogenase (LDH) enzyme, which has emerged as a potential target in cancer metabolism.

1.2 Lactate Dehydrogenase

LDH is an enzyme belonging to the oxidoreductases family, responsible for catalyzing the reversible interconversion of pyruvate and lactate [7]. Enzymes within this group are involved in redox reactions, wherein the oxidized substrate acts as the hydrogen or electron donor, whereas the reduced substrate serves as hydrogen or electron acceptor [8]. Specifically, in the reaction catalyzed by LDH, the reduction of pyruvate into lactate occurs simultaneously with the oxidation of NADH to NAD+, as shown in Figure 2.

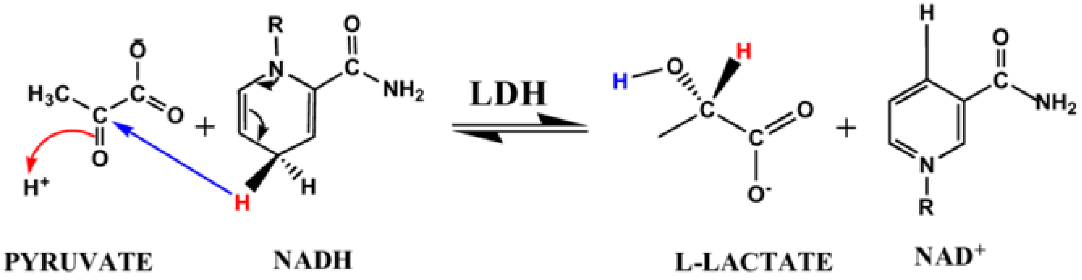

Figure 2. Schematic representation of the chemical reaction catalyzed by LDH. [58]

This conversion follows the last step of glycolysis in hypoxic conditions and it is crucial in regenerating NAD+, thereby sustaining glycolytic flux in the absence of oxygen [7]. Indeed two molecules of pyruvate are the end product of glycolysis, a fundamental metabolic process that generates energy in the form of ATP and NADH, as shown in Figure 3. Glycolysis occurs in both aerobic and anaerobic states. In the presence of oxygen pyruvate is oxidized to acetyl-CoA and enters the citric acid cycle, followed by oxidative phosphorylation, leading to the net production of 32 ATP molecules. Whereas in the absence of oxygen pyruvate is reduced to lactate with the simultaneous oxidation of NADH, exploiting the action of the LDH enzyme. Anaerobic respiration results in the production of 2 ATP molecules [9].

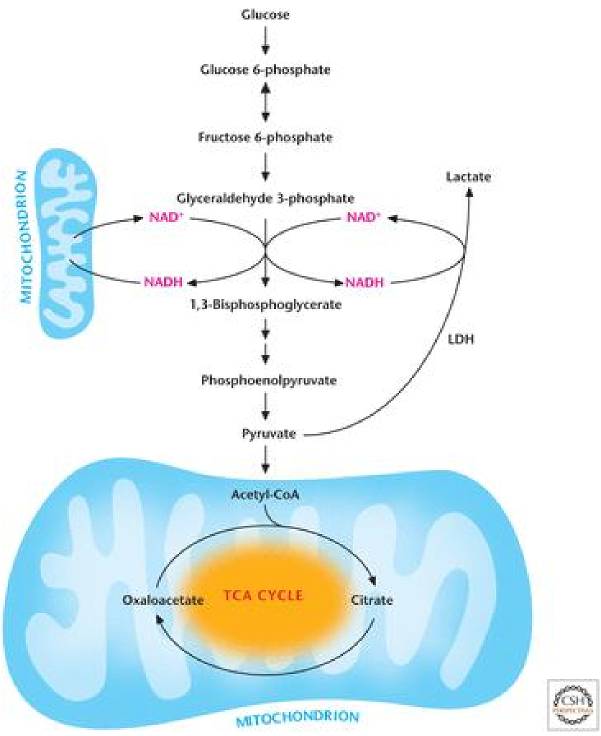

Figure 3. Schematic representation of glycolysis and of pyruvate's destiny. [59]

According to the direction of the reaction, pyruvate and lactate are respectively the substrate and the product of the reaction or the opposite. NADH and NAD+ are known as cofactors serving as redox carriers for biosynthetic and catabolic reactions [10]. LDH is the catalyst of the reaction. It has a tetrameric structure composed of two major subunits LDH-A and LDH-B, that can assemble in various configuration to form five different isoenzymes, each one with unique catalytic and physical properties. LDH-A is predominantly expressed in anaerobic tissues, like liver and skeletal muscle, while LDH-B is more abundant in aerobic ones, like the cardiac muscle [7]. Structurally, LDH is constituted of 40% alpha helices and 23% beta sheets, as shown in Figure 4. The active site is located within the substrate-binding pocket and includes key catalytic residues such as His-193, that works as proton acceptor, along with Arg-106, Asp-168 and Thr-246 [11]. A visual representation of the active site is shown in Figure 5.

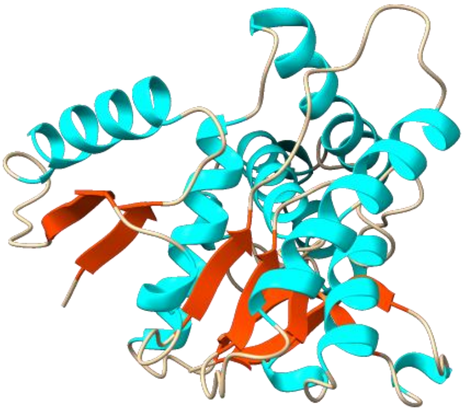

Figure 4. LDH structure. Alpha helices highlighted in light blue and beta sheets highlighted in orange. Obtained from protein visualization in ChimeraX.

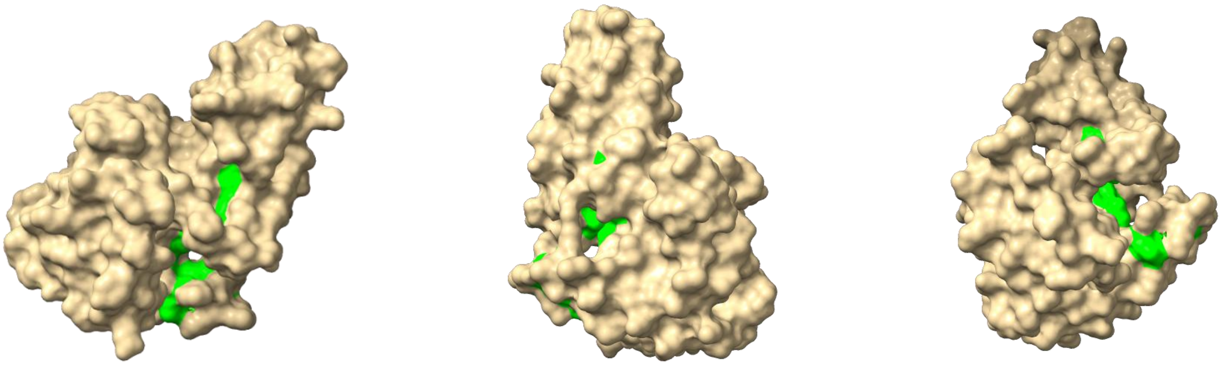

Figure 5. Different views of the 3D surface of LDH. The binding pocket is evidenced in green. Obtained from surface visualization in ChimeraX.

1.3 LDH-A's role in cancer and Warburg effect

LDH-A has an incredibly high expression in a variety of malignancies and it is associated with tumor progression and poor clinical outcomes. Solid tumors are characterized by three tissue regions: the normoxic, the hypoxic and the necrotic, as shown in Figure 6. Among these, the presence of hypoxic regions, characterized by a reduced oxygen availability, are a hallmark of many solid tumors and primarily result the aberrant and inefficient vasculature that develops to supply oxygen in response to the massive proliferation of cancer cells [12].

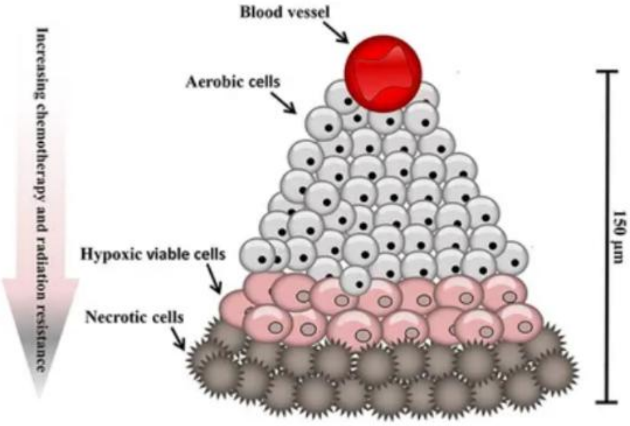

Figure 6. Normoxic, hypoxic and necrotic regions of solid tumors [12].

Unlike healthy tissues, which predominantly rely on mitochondrial oxidative phosphorylation for ATP production under normoxic conditions, tumors tend to adopt an altered metabolic phenotype. Even in the presence of oxygen, cancer cells often rely on an increased rate of glycolysis, followed by lactic acid fermentation, to support their energy demands. This phenomenon is called Warburg effect, also known as aerobic glycolysis. This metabolic reprogramming is facilitated by the overexpression of LDH, particularly of its isoform LDH-A, which preferentially catalyzes the conversion of pyruvate to lactate. Consequently, ATP synthesis shifts from oxidative phosphorylation towards aerobic glycolysis [7].

Despite the lower ATP yield of aerobic glycolysis (2 ATP molecules versus 32 from oxidative phosphorylation), the enhanced speed of this process is sufficient to support the growth and proliferation of tumoral mass [5]. Beyond its role in promoting aerobic glycolysis, LDH-A contributes to various critical aspects of cancer pathophysiology, namely [13]:

- Proliferation and survival. LDH-A supports tumor cell proliferation and survival by ensuring sufficient energy supply. Furthermore, it favors cancer stem cells phenotype, protects cancer cells from reactive oxygen species damage and prevents necrosis in hypoxic environment.
- Invasion and metastasis. Elevated lactic acid levels and LDH-A's regulatory effects on metastasis-associated proteins enhance tumor invasion and metastatic potential.
- Angiogenesis. It is regulated by LDH-A through the production of lactic acid which promotes the upregulation of vascular endothelial growth factor.
- Immune escape of cancer cells. This mechanism is supported by the overexpression of LDH-A, which facilitates immune evasion by inhibiting immune-mediated cytotoxicity and promoting an immunosuppressive tumor microenvironment.

The aforementioned critical aspects of cancer pathophysiology are summarized in Figure 7.

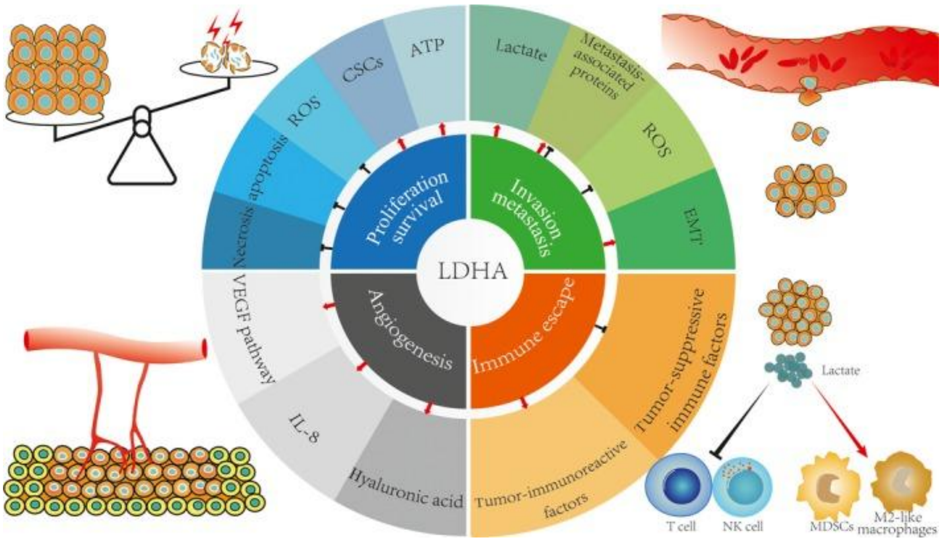

Figure 7. Overview of LDH-A's roles in hallmarks of cancer [13].

1.4 Alternative cancer therapies: LDH-A inhibitors

LDH-A is involved in cancer metabolism and plays a pivotal role in cancer cells proliferation and survival, whereas its silencing is minimally harmful to normal cells [13]. Consequently, a possible strategy to treat solid tumors, which are characterized by the overexpression of LDH-A, could be targeting this enzyme with selective inhibitors. Inhibitors can be classified into two categories: irreversible and reversible. Irreversible inhibitors covalently bind to specific residues within enzyme's active site, leading to a permanent loss of the enzymatic activity. Meanwhile, reversible inhibitors form non-covalent interaction with the enzyme, resulting only in a transient loss of the enzymatic activity [14]. Reversible inhibitors can be further classified, according to the nature of their interaction with the enzyme. To illustrate this classification, it is important to consider the enzyme's catalytic mechanism, which involves two main steps. In the first step, the substrate binds to the active site of the enzyme.

Subsequently, as second step, the bound substrate undergoes chemical transformation. Based on the interaction with these steps, reversible inhibitors can be categorized as competitive, non-competitive, or mixed-type. Competitive inhibitors interfere with the first catalytic step by competing with the substrate for binding to the active site of the enzyme. By contrast, non-competitive inhibitors bind to a different site of the enzyme, and they affect the second catalytic step. Finally, mixed-type inhibitors interfere with both steps of catalysis. A special case of mixed type-inhibition is the uncompetitive inhibition, in which the inhibitor binds only to the enzyme-substrate complex, as the inhibitor's binding site is formed only after substrate binding. Although most inhibitors exhibit mixed-type behaviour, they are generally described as competitive or non-competitive when one effect is significantly predominant than the other [15]. Based on the mechanism of action, LDH-A inhibitors can be classified as: pyruvate-competitive, NADH-competitive, pyruvate and NADH-competitive, and free enzyme-binding [13]. Key examples of LDH-A inhibitors with diverse mechanisms of action are:

- Galloflavin. It is a free enzyme-binding inhibitor, discovered in 2012 by Manerba et al [16]. It is a synthetic compound, specifically a gallic acid derivative [17], that inhibits both human LDH isoforms, showing minimal effects on normal cellular metabolism. Galloflavin preferentially binds to the free enzyme, without competing with either the substrate or the cofactor [13]. Galloflavin's structure is shown in Figure 8.

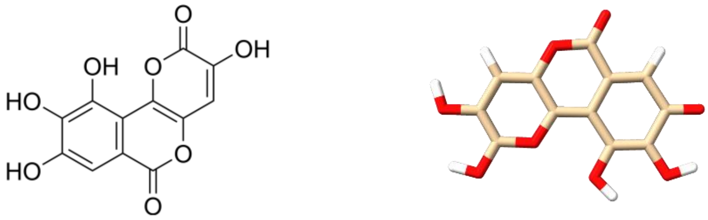

Figure 8. 2D [60] and 3D structure of Galloflavin. 3D structure obtained from compound visualization in ChimeraX.

- Oxamate. It is the salt of the half-amide of oxalic acid. It is an isosteric pyruvate form and thus acts as a pyruvate-competitive inhibitor [18]. Although its effectiveness has been validated through in vitro tests, its limited cell membrane permeability results in a required effective dose that is too elevated for practical *in vivo* administration [13]. Oxamate's structure is shown in Figure 9.

Figure 9. 2D [61]and 3D structure of Oxamate. 3D structure obtained from compound visualization in ChimeraX.

- Gossypol. It is a natural phenol derived from cottonseed oil. Its inhibitory effects on tumor growth have been demonstrated in mammary, colon, breast, melanoma and colorectal cells [19]. It is a NADH-competitive inhibitor [20]. Gossypol's structure is shown in Figure 10.

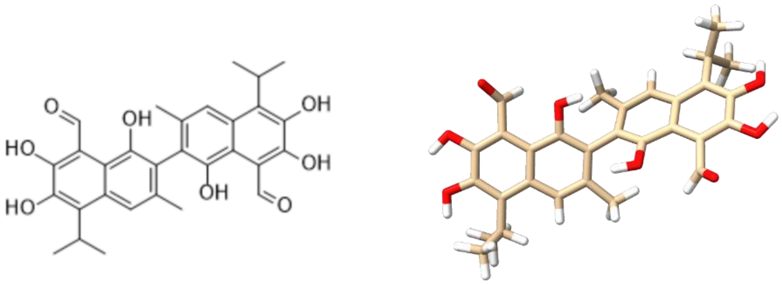

Figure 10. 2D [55] and 3D structure of Gossypol. 3D structure obtained from compound visualization in ChimeraX.

- FX-11. It is a NADH-competitive inhibitor, analogue of gossypol. It has demonstrated preclinical efficacy in lymphoma, pancreatic, and prostate cancer [21]. Although it shows a certain therapeutic potential, the highly reactive catechol moiety of FX-11 limits its suitability as a candidate drug for further development [13]. FX-11's structure is shown in Figure 11.

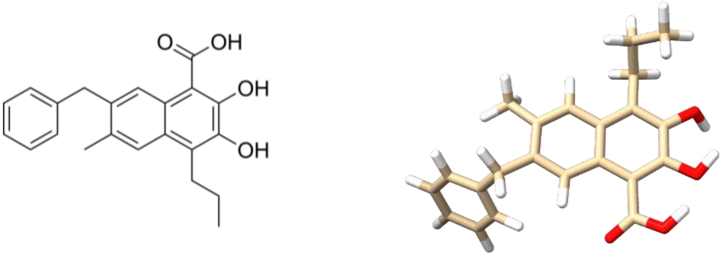

Figure 11. 2D [62] and 3D structure of FX-11. 3D structure obtained from compound visualization in ChimeraX.

- NHI-2. It is an inhibitor that competes with both the substrate and the cofactor. Cellular assays with NHI compounds have demonstrated their ability in impeding cancer cell proliferation [13]. Furthermore, studies have shown its effectiveness in altering cell cycle progression and inducing apoptosis in various glioblastoma (GBM) cell lines [22]. NHI-2's structure is shown in Figure 12.

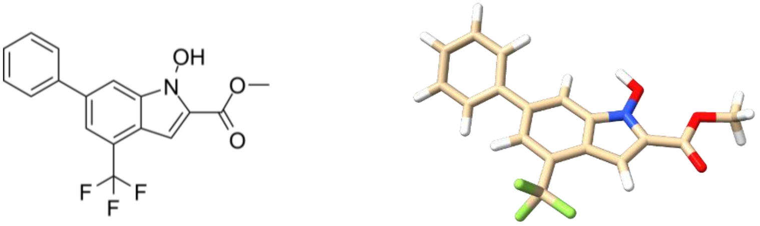

Figure 12. 2D [63] and 3D structure of NHI-2. 3D structure obtained from compound visualization in ChimeraX.

1.5 Enzyme kinetics

To investigate the inhibitory properties of compounds and their effects on enzyme behaviour, enzyme kinetics represents a powerful, quantitative and valuable approach. This method enables the measurements of the rate or velocity of enzyme-catalyzed reactions, allowing for the analysis of the factors that influence enzymatic activity and catalytic efficiency. Enzyme kinetics is typically studied through enzymatic assays, which quantify enzyme activity within a given sample. Several methodological approaches are available for conducting enzymatic assays, among which spectrophotometric monitoring of absorbance variation during the enzymatic reaction is widely employed. In fact, enzymatic activity is commonly estimated from spectrophotometric measurements, by calculating the slope of the linear portion of the reaction curve, which reflects the rate of change in the concentration of substrate or product monitored. As conventionally defined, “reaction rates in enzyme kinetics refer always to initial reaction rates where the maximum catalytic potential of the enzyme is expressed” [15]. These initial rates are essential to accurate determine the enzyme activity. The kinetic curve is obtained exploiting the spectrophotometer’s ability to detect changes in the light absorbance or scattering within the reaction solution. The majority of the tests are performed using a UV/visible spectroscopy, which typically operates within the wavelength range of 100-1100 nm. The wavelength selected for the analysis should allow a clear distinction between reactants and products, while minimizing interferences from other chemicals [23]. In this Master thesis, the enzymatic activity of LDH is assessed by leveraging a widely used spectrophotometric approach based on the specific absorbance properties of NADH. Notably, NADH absorbs ultraviolet light only in its reduced form, making it a reliable indicator of enzymatic oxidation-reduction processes.

The foundational hypothesis of enzyme catalysis was proposed by Michaelis and Menten, who described the process as a two-steps mechanism, represented as follows [24]:

$$\mathrm{E} + \mathrm{S} \underset{k_{-1}}{\overset{k_1}{\rightleftharpoons}} \mathrm{ES} \overset{k_2}{\rightarrow} \mathrm{E} + \mathrm{P}$$

where E is the enzyme, S is the substrate, ES is the enzyme-substrate complex, and P is the product. Firstly, the substrate bonds in the active site of the enzyme. Subsequently the amino acid residues within the active site chemically convert the substrate into the product, which is then released, regenerating the free enzyme. The first step is typically much quicker than the second one, consequently the formation of the ES complex is commonly assumed to be at equilibrium.

Based on this assumption, the Michaelis-Menten equation is derived to describe the initial reaction velocity (V_0) as a function of substrate concentration:

$$V_0 = \frac{V_{max} * [S]}{K_m + [S]}$$

Equation 1.

Where:

- V_{max}: maximum reaction velocity the enzyme can reach when the substrate is saturated (μmol min^{-1})
- [S]: substrate concentration (mM)
- K_m: Michaelis-Menten constant, which is the substrate concentration required to achieve half V_{max} (mM)

The graphical representation of the typical Michaelis-Menten's behaviour is provided in Figure 13.

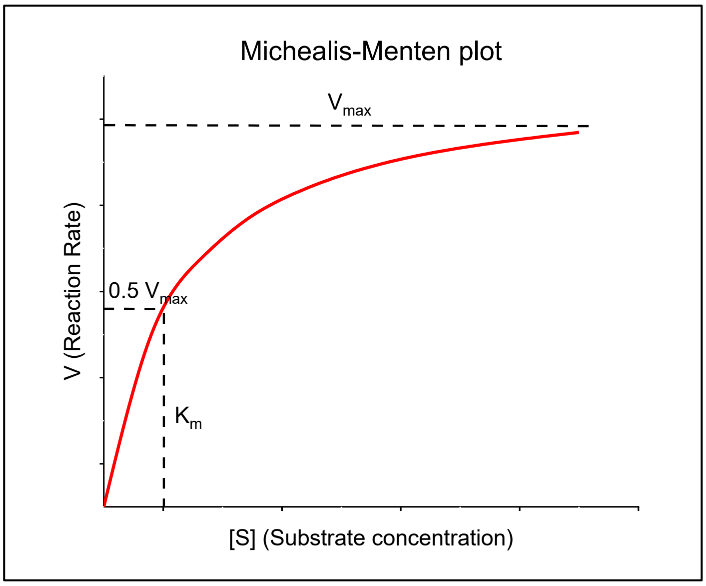

Figure 13. Graphical representation of the Michaelis-Menten plot and the associated parameters.

Beyond the classical Michaelis-Menten model, enzyme kinetics can also be described using the Hill equation:

$$V_0 = \frac{V_{max} * [S]^n}{K_m^n + [S]^n} \qquad \text{Equation 2.}$$

Where:

- V_{max}: maximum reaction velocity the enzyme can reach when the substrate is saturated (μmol min^{-1})
- [S]: substrate concentration (mM)
- K_m: Michaelis-Menten constant, which is the substrate concentration required to achieve half V_{max} (mM)
- n: the Hill coefficient, which represents the cooperativity level of the protein (-)

The equation was first introduced to describe the relationship of equilibrium between oxygen tension and the percent saturation of haemoglobin, but it is also applicable to enzyme kinetics that exhibit a sigmoidal curve in response to variations in the input concentrations. Mathematically, the Michaelis-Menten equation is a special case of the Hill equation, where n=1 [25]. The graphical representation of the typical Hill's behaviour is provided in Figure 14.

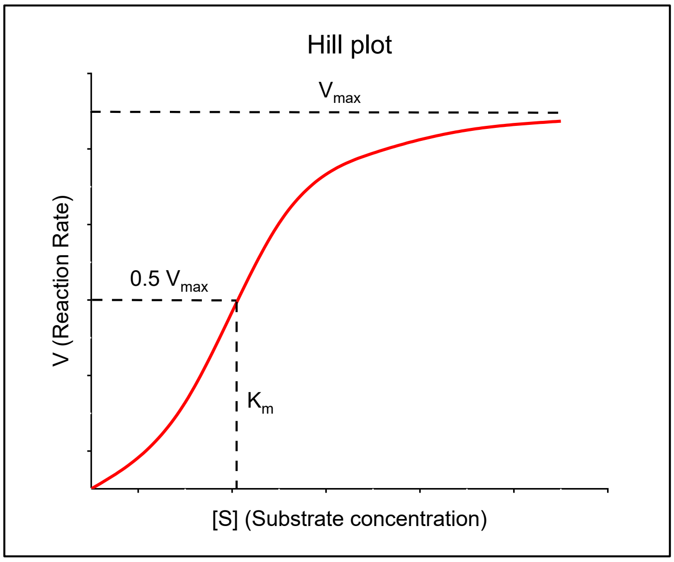

Figure 14. Graphical representation of the Hill plot and the associated parameters.

In order to determine the kinetic parameters of the aforementioned equations, various linearization methods have been developed. Among these the Lineweaver-Burk plot is frequently used.

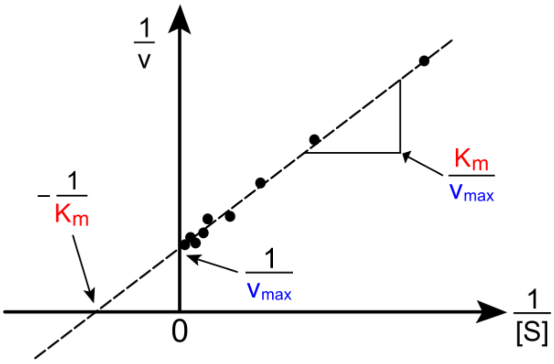

Figure 15. Graphical representation of the Lineweaver-Burk plot and the associated parameters.

The Lineweaver-Burk plot, shown in Figure 15, is a double reciprocal plot of $1/V_0$ versus 1/[S], with the slope corresponding to K_m/V_{max}, while the intercept on the Y-axis is the reciprocal of V_{max}. This is the only linearization approach in which independent and dependent variables are separated. However, a notable limitation is its tendency to amplify experimental errors, especially at low substrate concentration. For this reason, alternative linearization techniques that offer a more uniform error distribution, such as the Hanes-Woolf plot, are frequently employed. This type of linearization is shown in Figure 16.

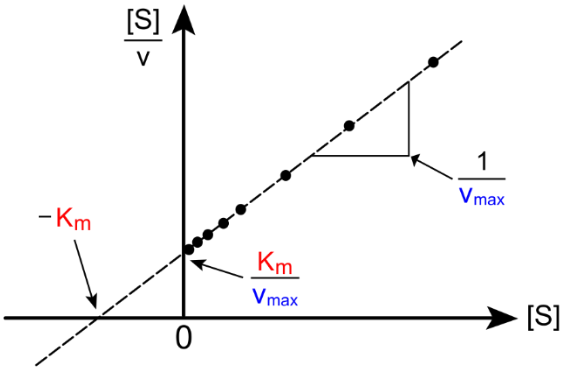

Figure 16. Graphical representation of the Hanes plot and the associated parameters.

This method plots $[S]/V_0$ against [S], yielding a slope equal to the reciprocal of V_{max}, while the intercept of the Y-axis is K_m/V_{max}. While it offers a more uniform error distribution, its main limitation lies in the placement of the independent variable on both axes, potentially complicating data interpretation [15].

Kinetic curves change due to inhibition and this change depends on the inhibition type. Reversible inhibition can be identified by analyzing how increasing inhibitor concentrations affect the relationship between reaction rate and substrate concentration. The linearization methods previously discussed are particularly valuable in elucidating the mechanism of inhibition.

A common and insightful approach involves Lineweaver-Burk linearization, plotted on the same graph for different inhibitor concentrations, as shown in Figure 17.

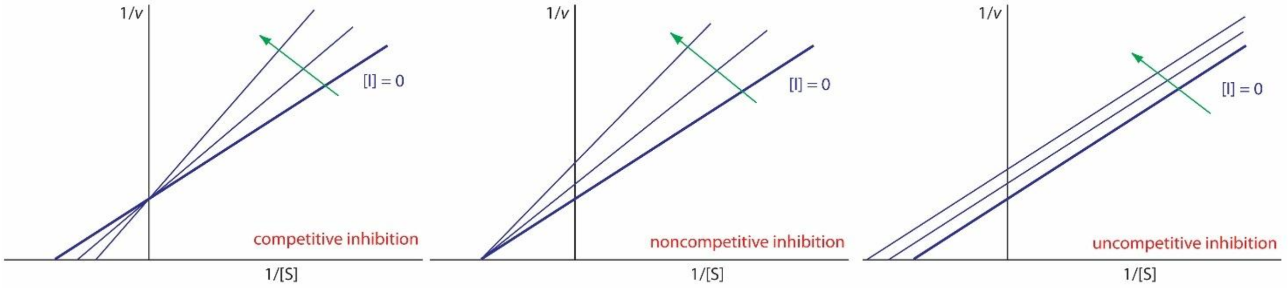

Figure 17.Linweaver–Burk plots for competitive, noncompetitive, and uncompetitive [26].

In each plot, the thick blue line represents the enzyme kinetic in the absence of inhibitor, while the thin blue lines depict the effect of increasing inhibitor concentrations, indicated by the direction of the green arrow.

In competitive inhibition, the inhibitor reversibly binds to the active site of the enzyme, directly competing with the substrate. As a result, the maximum velocity remains unaltered, since sufficiently high substrate concentrations can completely displace the inhibitor. This is reflected in the Lineveawer-Burk plot by an unchanged y-intercept ($1/\ V_{max}$). However, the apparent Michaelis constant increases, indicative of a reduced substrate affinity, which manifests as an increase in the slope and a leftward shift of the in the x-intercept's value.

In non-competitive inhibition, the inhibitor binds to an allosteric site on the enzyme, separate from the substrate-binding site. This implies that increasing the substrate concentration will not relieve the inhibition. In fact, an increase in the inhibitor concentrations result in a reduction of V_{max}, as evidenced by the increase of the y-intercept. Notably, K_m remains unchanged, implying that substrate binding affinity is not affected. Consequently, the x-intercept remains constant across inhibitor concentrations.

In the case of uncompetitive inhibition, the inhibitor binds exclusively to the enzyme-substrate complex, stabilizing it and enhancing the binding of substrate. Consequently, K_m is reduced. Meanwhile, the inhibitor-bound complex forms mostly under concentrations of high substrate. The enzyme-substrate-inhibitor complex is then unable to release product while the inhibitor remains bound, leading to a reduction in V_{max}. In the Lineweaver–Burk plot, this results in a family of parallel lines, each with increased y-intercepts and x-intercepts, reflecting decreased maximum velocity and enhanced substrate binding, respectively [26].

In mixed-type inhibition, the inhibitor exhibits the ability of binding both to the free enzyme and to the enzyme-substrate complex. As a general feature, V_{max} consistently decreases in this inhibition type. However, the effect on K_m is variable, as it can either increase or decrease [27]. An increase in K_m, indicating a diminished affinity of the enzyme for its substrate, suggests that the inhibitor preferentially binds to the free enzyme. Conversely, a decrease in K_m, implying enhanced substrate apparent affinity, signifies a preferential binding of the inhibitor to the enzyme-substrate complex.

A comprehensive summary of the effect of various inhibitor types on the kinetic parameters is provided in Table 1.

Table 1. Summary of the effect of different mechanism of inhibition on the kinetic parameters of the enzyme.

	Mechanism of inhibition			
	Competitive	Non-competitive	Uncompetitive	Mixed-type
V_{max}	Constant	Decrease	Decrease	Decrease
K_m	Increase	Constant	Decrease	Increase/Decrease

1.6 Research and development of new drugs

The pharmaceutical research and development (R&D) pipeline is a systematic and highly regulated process aimed at identifying potentially therapeutic drugs, demonstrating their safety and efficacy, and ultimately ensuring their accessibility to patients.

This process comprises several key stages, each contributing crucially to the identification and validation of drug candidates. The key steps are listed as follow [28]:

- Drug target identification. This step marks the initial phase of the pipelines and involves the selection of a biological molecule, most often a protein or gene, which is associated with the pathogenesis of a particular disease. The ideal drug target should be disease-specific, biologically relevant, and accessible to potential therapeutic agents.
- Drug screening and design. It follows the identification of the target. This phase involves the high throughput screening of large compound libraries to identify molecules that can bind effectively to the chosen target and modulate its activity. Identified molecules can be further modified and designed to improve their specificity, binding affinity and pharmacokinetic properties.
- Preclinical Testing. It represents the stage in which screened and selected drug candidate undergoes extensive laboratory investigations, including in vitro assays and in vivo studies, including animal models. These experiments aim to characterize the pharmacological profile of the compound, assess its toxicity and side effects, and gather preliminary data on its efficacy.

Only candidates demonstrating an acceptable safety margin and therapeutic promise move forward to the following step.

- Clinical Trials. It identifies the transition from laboratory research to human studies. This multi-phase process begins with Phase I trials, which assess the safety and tolerability of the drug in a small group of healthy volunteers or patients. Phase II trials focus on evaluating the efficacy and optimal dosing regimen in a larger patient population, while Phase III trials involve large-scale testing across diverse populations to confirm effectiveness, monitor adverse effects, and compare the new therapy to standard treatments.
- Regulatory Approval: Throughout the entire drug discovery process, the potential drug must adhere to stringent standards established by regulatory agencies. Notable examples include the Food and Drug Administration (FDA) in the United States and the European Medicines Agency (EMA) in the European Union. They require comprehensive documentation of all preclinical and clinical findings before a drug can be approved for commercial use. These agencies ensure that new therapies meet rigorous standards for quality, safety, and efficacy, and they continue to monitor approved drugs through post-marketing surveillance.

The process of identification, development and approval of novel chemical entities is fraught with significant scientific, logistical and economic challenges. The process is not only inherently complex, involving iterative cycles of testing and optimization, but also time-intensive and costly. A statistical report by the Tufts Centre for the Study of Drug Development (CSDD), indicates that the overall cost for a single new drug discovery, from initiation to approval, can reach $2.6 billion, with the entire drug development pipeline often requiring up to 14 years of research and tests [29].

These challenges underscore the growing necessity to develop innovative techniques that can streamline drug discovery and reduce development costs. Indeed, as highlighted in Figure 18, the initial phase is characterized by the highest costs and longest duration. In this context, molecular modelling, which enables the in-silico prediction of molecular interaction, and biosensors, which allow real-time, sensitive detection of biological and chemical interactions, have emerged as particularly promising tools for accelerating the identification of viable therapeutic candidates.

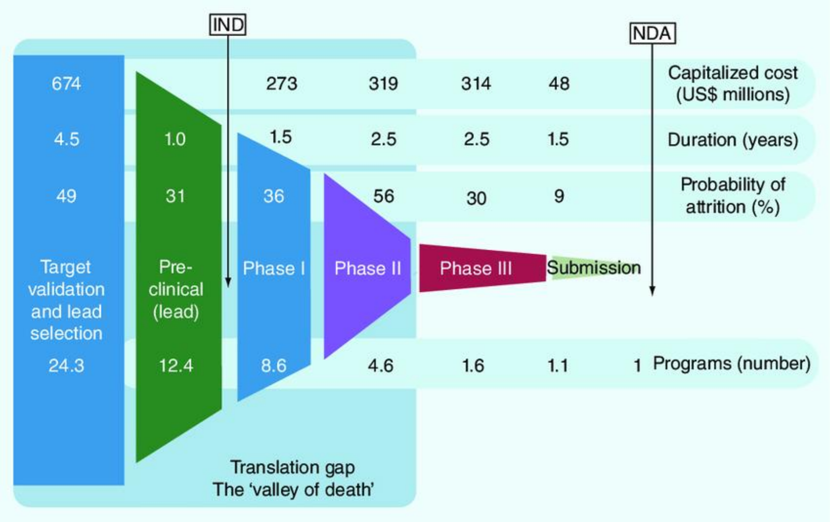

Figure 18. The drug-development life cycle, duration of each one of the stages, capitalized costs, and the probability of failure [64].

1.6.1 Molecular Modelling

The advent of high-performance computing has significantly facilitated in silico virtual experimentation, serving as a crucial bridge between laboratory-based research and theoretical models.

Among the most powerful computational techniques is molecular modelling which enables the generation, the visualization and the manipulation of the 3D structures of chemical and biological molecules. This approach provides valuable insight into chemical and physical properties of the molecules, enables structural comparison between different compounds, and the visualization of molecular interactions between different molecules/macromolecules, with the resulting formed complexes. Furthermore, it can be employed to predict the conformations of novel or related molecules [30]. As a computational technique, molecular modelling is both a cost-effective and efficient approach. Two of the principal techniques within this field are: molecular docking and molecular dynamics (MD) simulation, each offering unique advantages depending on the specific research objectives.

Molecular docking is a structure-based technique designed to predict the preferred orientation of a small molecule (ligand) when bound to a macromolecule. This method simulates the interaction between ligand and receptor within the target's binding site. It requires a high-resolution 3D representation of the target protein, which can be obtained exploiting techniques like Nuclear Magnetic Resonance Spectroscopy and X-ray crystallography [31]. The docking process considers various non-covalent interactions, including electrostatic interactions, Van der Waals, Coulombic and hydrogen bonds. The interactions between the analysed structures are summed and the result is approximated by a docking score which gives an indication of their bonding potential. The prediction is achieved by the algorithm following two main steps. In the first one conformational space is explored and the algorithm identifies potential binding poses. In the second step, the binding free energy is estimated to evaluate the affinity and the stability of each ligand conformation. The resulting docking score reflects the predicted binding potential, with lower energy values typically indicating more favourable interactions [32].

MD simulation is a computational technique employed to investigate the time-dependent behaviour of molecular systems. This technique models the motion of atoms and molecules by solving Newton's equations of motion, using force fields that describe bond stretching, angle bending, torsional rotations and non-bonded interactions. The process involves several key steps: system preparation, energy minimization, equilibration of the system, and finally the running of the simulation for a specific period of time, during atomic coordinates are iteratively updated over time based on calculated forces [33].

Molecular docking and molecular dynamics (MD) simulations each address distinct purposes within computational studies. The choice between these methods largely depends on the research objectives, available computational resources, and the nature of the system under investigation. During the initial phases of drug discovery, molecular docking is typically the preferred choice due to its speed and suitability for high-throughput virtual screening. Indeed, docking enables rapid identification of compounds with high binding potential with the target molecule which is especially valuable for designing enzyme inhibitors or receptor agonists, offering a practical way to quickly identify promising drug candidates. Conversely, molecular dynamics (MD) simulation is more appropriate when the aim is to investigate binding stability between ligands and proteins, mimic intricate interactions within complex biological systems, or explore the impacts of solvents and the surrounding environment. MD thus offers a more realistic and detailed representation of molecular behaviour over time, making it indispensable for fine-tuning drug candidates and validating docking results [33].

1.6.2 Biosensor for anticancer drug screening

A biosensor is an analytical device designed to convert a biological or chemical reaction response into a quantifiable and detectable signal [34]. The generated signal is typically proportional to the concentration of the target analyte within the analyzed sample. Generally, a biosensor consists of an analyte, a bioreceptor, a transducer, an electronic system and a display unit, as illustrated in Figure 19. The analyte refers to the substance of interest, typically a specific biomolecule or chemical, while the bioreceptor is the component responsible for recognizing and binding the analyte. Common types of bioreceptors include enzymes, nucleic acids (DNAs or RNAs), cells, aptamers and engineered nanoparticles.

The interaction between the analyte and the bioreceptor initiates the biorecognition process, during which a primary signal is produced. The generated signal is then converted by the transducer into a measurable form, through a process referred to as signal transduction or signalisation. The nature of the output signal can be electrical, thermal or also optical, depending on the biosensor design, and it is generally proportional to the extent of analyte-bioreceptor interactions. The transduced signal is subsequently processed by the biosensor's electronic system, which typically performs signal processing like amplification, filtering and conversion of signals from the analogue form into the digital one. Finally, the processed data results are presented via a display interface. They can be shown in a variety of ways including numeric, graphic or tabular, according to the requirements of the end user [35].

A comprehensive scheme of the biosensor's components is shown in Figure 19.

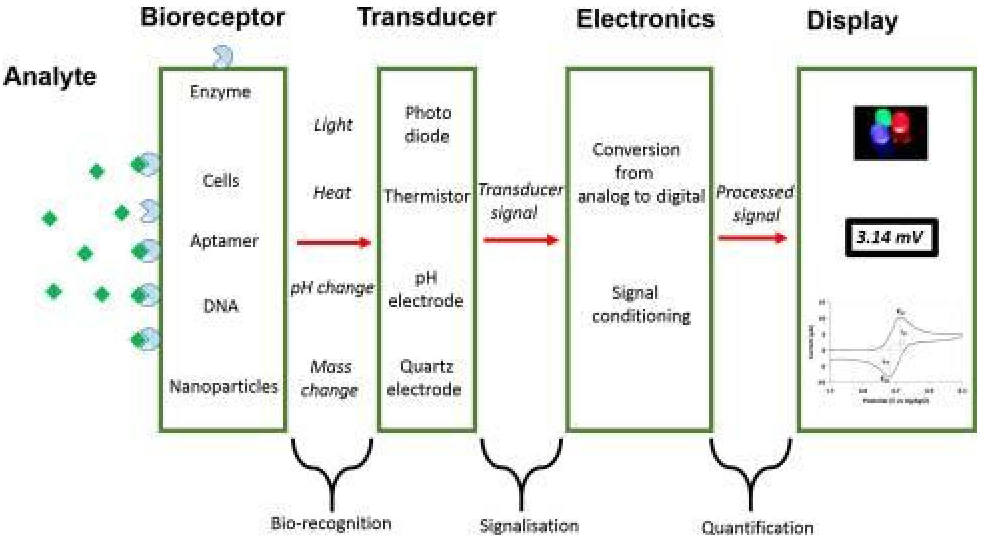

Figure 19. Schematic representation of a biosensor. [35]

Given the relevance of LDH on cancer cells metabolism, the development of a biosensor for screening new possible LDH inhibitors could be a valuable tool to discover the potential of new anticancer drugs, minimizing the cost and the time of the experiments [36]. Nowadays the methods used to perform drug screening primarily rely on structure-based ligand design and biochemical or cellular assays that asses

LDH-inhibition, protein-ligand interaction, or biological activity in cell-based systems [37]. However, the majority of these methods are time-consuming, resource-intensive and in some cases, such as cell-based biological assays, challenging to interpret [38]. These limitations underscore the potential value of a biosensor-based approach as an efficient, rapid, and cost-effective alternative for evaluating LDH-inhibitory activity in candidate compounds.

2. Materials and methods

The present work aims to a comprehensive evaluation of LDH's behaviour under various experimental conditions and in the presence of different substances. The ultimate objective is to gather fundamental knowledge, necessary for the future development of a bioreactor that will incorporate LDH for a fast, reproducible and cost-effective screening of potential anticancer drugs. In order to reach this goal, LDH would be likely used in its immobilized form. Although the immobilization process itself is not addressed within the scope of this study, understanding the enzyme's native characteristics is an essential preliminary step.

To this end, the present work focuses on the free enzyme, investigating its catalytic activity, stability, and interaction with various compounds that may be present in the reaction medium. These factors are crucial in defining the enzyme's performance and limitations in a real application context. Knowledge of how LDH responds to changes in pH, temperature, and chemical environment is indispensable for designing an immobilization strategy that preserves or enhances its functional properties.

While immobilized enzymes are commonly used in biosensor applications due to their reusability and resistance to loss in solution, such advantages can only be fully exploited if the free enzyme's behaviour is well understood.

2.1 UV-Vis Spectroscopy

To reach the aforementioned goal, ultraviolet-visible (UV-Vis) spectrophotometry was selected as the primary analytical technique. UV-Vis spectroscopy is widely employed across scientific disciplines due to its ability to measure the amount of discrete UV or visible light wavelengths absorbed or transmitted by a sample, typically in comparison to a reference or blank. The degree of light absorption is influenced by the sample's chemical composition, making this technique particularly valuable for identifying and quantifying molecular constituents. The absorption of ultraviolet and visible light is linked to specific functional groups within the molecules, defined as chromophores. Moreover, absorbance is an additive property; therefore, when multiple compounds present in a sample absorb at the same wavelength, the resulting absorbance will reflect the cumulative contributions of each individual species, potentially leading to spectral overlap and interference.

More in detail, when a beam of light passes through a sample, certain wavelengths are absorbed if their energy matches the energy required to promote electrons within the molecules from a lower to a higher electronic energy state. These electronic transitions involve $\sigma \rightarrow \sigma^*$, $n \rightarrow \sigma^*$, $\pi \rightarrow \pi^*$ or $n \rightarrow \pi^*$ excitations. Where σ, σ^*, n, π, π^* are the type of molecular orbitals involved in the electronic transitions [39].

A UV-Vis spectrophotometer comprises several essential components [40]:

- Light Source. A stable source capable of providing a broad spectrum of wavelengths is essential. Common sources include tungsten, halogen, or deuterium.
- Wavelength Selector. This component is used to isolate the specific wavelength required for analysis. This can be achieved using monochromators, absorption filters, interference filters, cutoff filters, or bandpass filters. Monochromators and filters are often combined together to narrow the selected wavelengths, improve the resolution and enhance the signal-to-noise ratio.

- Sample compartment. The selected light passes through the sample. A reference or blank sample, typically the solvent alone, is also measured to ensure accurate baseline correction and obtain the true absorbance values of the analytes. In fact, the solvent in which the absorbing species or the analyte is dissolved also as an effect on the spectrum of the species itself, shifting the absorbing peaks to shorter wavelength (blue shift) or higher ones (red shift) depending on its polarity.

  One key aspect for the sample preparation regards the sample holder material. In liquid-phase spectroscopy, cuvettes are typically used to contain the sample solution during measurements. It is essential to consider the optical properties of the cuvette material, as they can significantly affect the accuracy and reliability of the absorbance data. Cuvettes are typically made of plastic materials or quartz. Plastic cuvettes are unsuitable for ultraviolet absorption measurements because plastic tends to absorb UV light, interfering with the detection of analytes in this region. Quartz, instead, is transparent across a broad range of UV and visible wavelengths.

  Moreover, the surrounding environment can also influence UV measurements. For instance, air can act as a natural filter: molecular oxygen absorbs light below approximately 200 nm, which limits the measurable spectral range under normal atmospheric conditions. To access wavelengths shorter than 200 nm, specialized instrumentation is needed, typically involving an optical system enclosed and purged with inert gases such as pure Argon.
- Detector. After interacting with the sample, the light reaches a detector, which converts the optical signal into a readable electronic signal. Detectors commonly rely on photoelectric coatings or semiconductors to capture the signal.
- Computer Interface. The electronic signal generated by the detector is recognized, processed, and visualized via dedicated software, allowing real-time monitoring and data acquisition.

A schematic representation of a UV-Vis spectrophotometer's internal parts is provided in Figure 20.

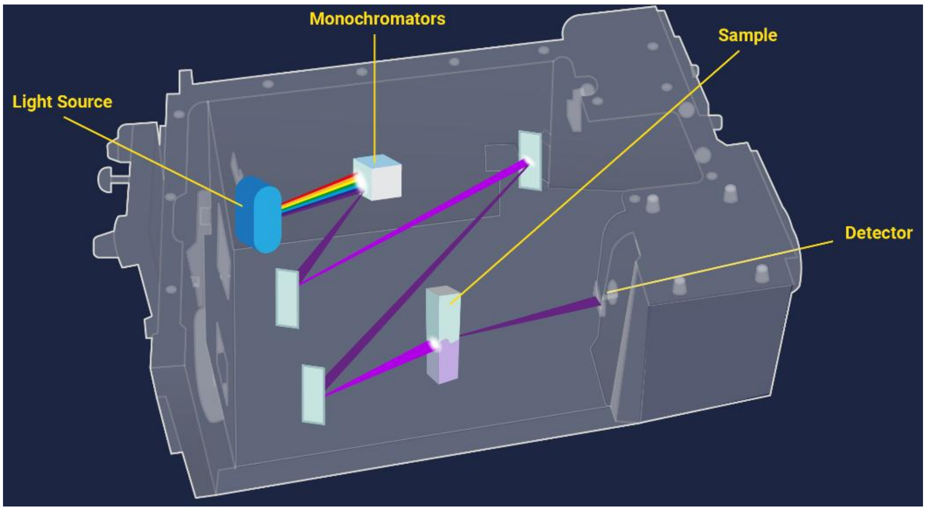

Figure 20. Schematic diagram of UV-Vis spectroscopy system [40].

This technique offers several significant advantages, that make it especially suitable for biochemical studies, such as the objective of the present Master's Thesis. These advantages include being non-destructive, rapid, user-friendly, requiring minimal sample processing and being relatively low-cost, compared to other analytical methods.

.

2.1.1 Absorption Spectra

Identifying the specific wavelength at which a substance exhibits maximum absorbance is essential for accurately setting the spectrophotometer. In fact, in UV-Vis spectroscopy, the analytical wavelength is typically set at the point of maximum absorbance for the target substance, as this enables maximum sensitivity and selectivity in monitoring the analyte [40]. Consequently, the initial phase of this Master's thesis involved acquiring the UV-Vis absorption spectra of all compounds participating in the LDH-catalyzed enzymatic reaction: pyruvate, NADH, NAD+, and lactate. The primary objective of this preliminary analysis was to identify an optimal wavelength for subsequent spectrophotometric measurements.

The absorption spectra were recorded using a “Jasco V-730” spectrophotometer set in "Spectra Measurements" mode. The wavelength was change in the range within 220 nm and 750 nm. Measurements were conducted using quartz cuvettes, selected for their superior transparency across the UV and visible regions, which ensures accurate detection throughout the scanned range.

Prior to sample analysis, a baseline measurement was performed. For the acquisition of the baseline 3 mL of 0.1 M pH 7.4 potassium phosphate buffer [41] were placed in the quartz cuvette, as it represents the dilution solvent in which the subsequent kinetic tests were performed Once acquired, the baseline data was subtracted from all subsequent measurements to effectively eliminate the background noise or any signal due only to the buffering solution. After the acquisition of the baseline, all the substances were individually tested. A proper amount of solution of each of the substance was added to the quartz cuvette, in order to reach the desired concentration. In each case, the total volume contained in the cuvette was equal to 3 mL. To ensure reliable measurements, each solution was thoroughly mixed before analysis until no visible inhomogeneities were observed, thereby promoting consistent absorbance readings across the cuvette.

Table 2 summarizes the concentrations of the tested compounds.

Table 2. Summary of the of the compound concentration used for every test during the spectra measurements.

Compound	Pyruvate	NADH	Lactate	NAD+
Concentration (mM)	1.63	0.23	0.23	0.23

The pyruvate concentration was selected based on prior studies [42], which indicated that lower concentrations did not support sufficient enzymatic conversion. This choice also offered the advantage of simplifying weighing procedures. This choice also offered the advantage of easier handling and weighing. The NADH concentration was likewise determined from previous studies [42], as higher concentrations led to saturation during spectrophotometric detection. The same concentration of NADH was used for NAD+, assuming full conversion of NADH in NAD+ under reaction condition. Finally, The lactate concentration of 0.23 mM was selected according to stoichiometric consideration related to the enzymatic reaction mechanism. In the LDH-catalyzed reaction, NADH and pyruvate are consumed in equimolar amounts to produce NAD+ and lactate, according to the hereafter reported reaction:

$$Pyruvate + NADH \ \leftrightarrow Lactate + NAD^{+}$$

This 1:1 stoichiometric relationship implies that for each mole of NADH consumed, one mole of lactate is produced. In the tested conditions, NADH was present at a lower concentration than pyruvate (0.23

mM vs. 1.63 mM), and therefore clearly acts as the limiting reagent. Since pyruvate is in excess, all of the NADH can, in principle, be converted. As a result, the maximum concentration of lactate that can be formed is directly determined by the initial concentration of NADH. Thus, complete conversion of NADH would yield an equivalent concentration of lactate. Based on spectral data and for reasons better detailed in the Results section, 340 nm was selected as the optimal wavelength for analysis. This specific wavelength will be used in all subsequent kinetic assays to evaluate biocatalytic activity.

Whenever a new substance is introduced in the reaction medium, it is essential to evaluate its potential effect on measurements. For this reason, in this context, absorption spectra were also acquired for Dimethyl sulfoxide (DMSO), since it was used as solvent for the inhibitors tested on LDH in the kinetic assays. Finally, the absorption spectra were acquired also for all the tested inhibitors, namely: Galloflavin, Oxamate, Gossypol, FX-11, and NHI-2. These aforementioned steps were crucial to identify any potential spectral overlap at the previously selected wavelength between different compounds. This potential overlap could interfere with affecting the accuracy of absorbance-based quantification measurements and the interpretation of reaction outcomes.

The acquisition procedure is the same detailed for just reagents and products of the enzymatic reaction.

Table 3 summarizes the concentrations of the DMSO and of the inhibitors tested.

Table 3. Summary of the quantity of buffer and tested inhibitor used for every test during the spectra measurements.

Compound	DMSO	Galloflavin	NHI-2	Oxamate	FX-11	Gossypol
Concentration (µM)	46780	20	40	40	20	40

The DMSO concentration refers to the concentration of the pure solvent within the cuvette. Conversely, the inhibitor concentrations correspond to the maximum concentrations evaluated in the subsequent kinetic assays, ensuring that spectral measurements reflect the most critical conditions for evaluating interference at the chosen wavelength.

To complete this series of measurements, NADH absorption spectra were recorded at varying concentrations, ranging from 0.005 mM to 0.1 mM. A complete list of the tested concentration is provided in Table 4.

This specific concentration range was crucial as these low values will constitute the initial data points for the enzyme kinetic assay. At these low concentrations, even a minimal absorbance contribution from an inhibitor absorbing at 340 nm could significantly perturb the accuracy of the measurements. Therefore, confirming the absence of such overlap was essential to ensure the accuracy and reliability of the subsequent kinetic measurements.

Table 4. Summary of the quantity of buffer and tested cofactor used for every test during the spectra measurements.

NADH concentration (mM)	0.005	0.01	0.015	0.025	0.05	0.1

2.1.2 Enzyme activity

The enzyme activity was evaluated through the “Time course” mode of the spectrophotometer “Jasco V-730”, set at a wavelength of 340 nm. This method exploits the property of NADH to absorb UV light at the specified wavelength only in the reduced form and not in the oxidized one. Consequently, it was possible to quantify the activity of LDH, which uses NADH as cofactor, by tracking the decrease in absorbance over time. This absorbance variation directly indicated the consumption of the cofactor as the enzyme reaction proceeds.

A computer interface allowed for real-time data visualization, displaying the variation of absorbance over approximately 120 s, due to NADH consumption, at defined concentration of substrate and cofactor.

As anticipated, the complete kinetic curve was obtained by varying either the substrate or cofactor concentration while keeping the other fixed (pyruvate at 1.63 mM and NADH at 0.23 mM). In order to have reliable, precise results, and assess errors associated with experimental results, all the experiments were conducted in triplicate. The final value for each condition corresponds to the average of the three replicates and associated error bars represents the standard deviation. The resulting data were plotted as kinetic curves, showing the initial reaction velocity, corresponding to the product formation rate, as a function of the varied cofactor or substrate concentration.

To determine the reaction velocity, the initial linear portion of the NADH absorbance decay curve was considered, applying the following equation [43] to calculate the activity of the free enzyme:

$$A_{FE} = \frac{\Delta A}{\varepsilon * L} * \frac{V_C}{V_e} * \frac{1}{C_p}$$ *Equation 3.*

Where:

- ΔA: absorbance slope (-)
- ε: NADH molar extinction coefficient (6.22 mM^{-1} cm^{-1})
- L: optical path (1 cm)
- V_C: volume solution in the cuvette (3.01 mL)
- V_e: enzymatic solution volume (0.1 mL)
- C_p: concentration of the enzymatic solution (0.01 mg mL^{-1})

Enzymatic activity, typically expressed in International Units (IU), refers to the amount of enzyme required to catalyze the conversion of 1 micromole of substrate per minute under defined conditions of temperature, pH, and substrate concentration. This value is often normalized per gram or milligram of biocatalyst to express specific activity.

However, in this thesis, enzymatic activity was not expressed in IU per mg of protein but rather reported directly as the rate of product formation in micromoles per minute (μmol/min), based on the initial linear portion of the NADH absorbance curve.

Kinetic experiments were conducted to characterize the enzyme's intrinsic biocatalytic activity and to investigate the effects of DMSO and various inhibitors. For each tested condition, kinetic curves were generated by varying either the substrate or the cofactor concentrations. Experimental data were interpolated using Michaelis-Menten equation in the case in which pyruvate concentration was varied. While varying cofactor concentration instead, the most representative equation was the Hill's one. Data interpolation and fitting were performed using Origin software, which also enabled the extraction of kinetic parameters. For the curves obtained by varying the substrate concentration, thus fitting the Michaelis–Menten model, kinetic parameters were validated through both Lineweaver–Burk (Equation

4) and Hanes–Woolf (Equation 5) linearization, in order to confirm the consistency and reliability of the calculated K_m and V_{max}.

Kinetic parameters were calculated to evaluate enzyme intrinsic characteristics and the inhibitor's effect on enzyme kinetics and to compare the compounds' different impacts. The linearizing equations are presented below:

$$\frac{1}{V_0} = \frac{K_m}{V_{max} * [S]} + \frac{1}{V_{max}} \qquad \text{Equation 4.}$$

$$\frac{[S]}{V_0} = \frac{[S]}{V_{max}} + \frac{K_m}{V_{max}} \qquad \text{Equation 5.}$$

Where:

- V_{max}: maximum reaction rate the enzyme can reach at substrate saturation conditions (μmol min^{-1})
- V_0: enzymatic reaction rate (μmol min^{-1})
- [S]: substrate concentration (mM)
- K_m: Michaelis-Menten constant, which is the substrate concentration required to achieve half V_{max} (mM)

2.1.2.1 Intrinsic activity of the enzyme

The intrinsic biocatalytic activity of the enzyme was initially evaluated to establish baseline kinetic curves, which served as reference data for assessing the influence of varying experimental conditions and the presence of potential inhibitors.

To assay the biocatalytic activity, 0.1 M pH 7.4 potassium phosphate buffer was prepared [41]. This buffer was utilized to solubilize the reaction cofactor (NADH) and the substrate (pyruvate). Both the cofactor and substrate solutions were thoroughly mixed using a vortex mixer to ensure homogeneity.

For the enzyme solution preparation, a 21 μL aliquot of the enzyme was thawed at room temperature for 30 minutes. Subsequently, a proper amount of 0.1 M pH 7.4 buffer was added to achieve a final enzyme concentration of 0.01 mg/mL. Once the three solutions were prepared, the kinetic assays were carried out.

As previously described, the spectrophotometer was set in “Time course” mode and the variation of the absorbance at 340 nm over time was recorded. The cuvette for the analysis contained cofactor, substrate, and enzyme. Specifically, for the test, the blank and the sample PMMA cuvette contained the following components:

- 2.71 mL of 0.1M pH 7.4 potassium phosphate buffer
- 100 μL of NADH solution
- 100 μL of pyruvate solution

For the kinetic curve obtained by varying pyruvate concentration, the initial NADH stock solution was prepared at 7 mM, resulting in a final concentration of 0.23 mM in the cuvette, and the substrate concentration ranged from 0.005 mM to 1 mM. Conversely, for the curve generated by varying NADH concentration, the pyruvate stock solution was prepared at 49 mM, yielding a final concentration of 1.63 mM in the cuvette, with a cofactor concentration ranging from 0.005 mM to 0.3 mM. NADH concentration did not exceed 0.3 mM to avoid signal saturation of the spectrophotometer. Each data point was obtained in triplicate.

The reaction was initiated by the addition of the enzyme solution to the sample cuvette. Magnetic stir bars were included in both the blank and sample cuvettes to maintain uniform mixing throughout the analysis.

All assays were performed at a temperature of 37°C and at a 7.4 pH, to mimic physiological conditions commonly employed in most cellular assays.

In multi-substrate enzyme reactions, such as the one under examination, conventional kinetic measurements often yield apparent kinetic parameters, that depend on specific experimental conditions, including pH, temperature, and fixed concentrations of other reactants. To determine the true kinetic parameters of LDH, that are independent from these constraints, a more comprehensive kinetic analysis, involving the use of secondary plots, was conducted.

Before utilizing secondary plots, a thorough understanding of the reaction mechanism was crucial. The LDH catalyzed reaction proceeded via a sequential mechanism, meaning all substrates bound to the enzyme before the catalytic reaction took place. Furthermore, it exhibited an ordered sequential mechanism, where substrate binding occurred in a predetermined sequence. Specifically, for LDH-catalyzed reactions, NADH bound first [44], followed by pyruvate.

Figure 21. Schematic representation of sequential ordered mechanism.

A general scheme for a sequential ordered mechanism is illustrated in Figure 21, where A and B represented the substrates, and Y and Z are the products. In the context of LDH, A corresponded to NADH (due to its initial binding), and B represented pyruvate.

$$v = V_{AP} * \frac{a}{K_{AP} + a} = V'_{AP} * \frac{b}{K'_{AP} + b} \qquad \text{Equation 6.}$$

$$\frac{1}{v} = \frac{K_{AP}}{V_{AP}} * \frac{1}{a} + \frac{1}{V_{AP}} = \frac{K'_{AP}}{V'_{AP}} * \frac{1}{b} + \frac{1}{V'_{AP}} \qquad \text{Equation 7.}$$

Where:

- a, b: first and second substrate concentration (mM)
- V_{AP}: maximum reaction rate as function of b (μmol min^{-1})
- V'_{AP}: maximum reaction rate as function of a (μmol min^{-1})

- K_{AP}: Michaelis-Menten constant as function of b (mM)
- K'_{AP}: Michaelis-Menten constant as function of a (mM)

The Equations 6 and Equation 7 represent the kinetic equation of the sequential mechanism and the subsequent linearization. This linearization was instrumental in enabling the generation of the secondary plots.

Secondary plots are graphical tools used to correct for the influence of varying substrate or cofactor concentrations on the apparent kinetic parameters. This method involves performing enzymatic assays at different fixed concentrations of one reactant (termed the "b parameter") while varying the other. The apparent kinetic parameters derived from each condition are then plotted as a function of the b parameter (or its reciprocal), allowing for the extrapolation of the true kinetic constants based on the intercepts of the resulting linear regressions.

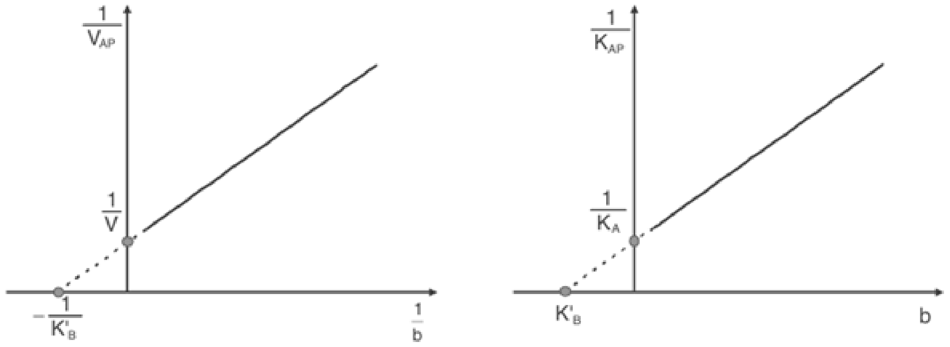

Figure 22. Secondary plots for the determination of kinetic parameters in sequential ordered mechanisms [15].

The secondary plots shown in Figure 22 are characteristic of a sequential ordered reaction mechanism. If the mechanism had instead followed a random binding order, different patterns in the secondary plots would have been observed, requiring alternative analytical models.

To generate these secondary plots, LDH activity measurements were replicated by systematically varying the fixed concentration of either the cofactor or the substrate (referred to as the b parameter in Figure 22). Therefore, the kinetic assays were conducted with three additional fixed concentrations of both cofactor and substrate. The specific concentrations tested are summarized in Table 5.

Table 5. Summary of the fixed concentrations applied to find the real kinetic parameters.

“b” parameter	
Fixed NADH concentration [mM]	Fixed pyruvate concentration [mM]
0.05	0.5
1	1
0.23	1.63
0.3	3

All assays were conducted under the same pH and temperature conditions used for the determination of the apparent kinetic parameters, ensuring consistency and comparability of results. For each experimental condition, individual data points were measured in triplicate to ensure reproducibility and statistical reliability. Moreover, when NADH concentration was fixed, the substrate concentration was varied in the range of 0.005 mM to 1 mM. Conversely, when pyruvate concentration was fixed, the NADH concentration was varied between 0.005 mM and 0.3 mM.

To ascertain the true V_{max} value, the reciprocal of parameter b was plotted on the x-axis while the apparent V_{max} values, obtained from each primary kinetic analysis, were plotted on the y-axis. The linear regression of these data yielded a straight line, whose y-intercept allowed the calculation of the real V_{max}.

In an analogous manner, to determine the true K_m value, parameter b was plotted on the x-axis against the apparent K_m values on the y-axis. The resulting linear plot provided a y-intercept, whose reciprocal value allowed the determination of true K_m.

2.1.2.2 Effect of DMSO on the activity of the enzyme

Following the initial characterization, the impact of DMSO on the enzyme's intrinsic activity was evaluated. This step was crucial as the inhibitors under investigation required DMSO for solubilization.

The rationale for using DMSO as a solvent lies in its ability to dissolve both hydrophobic and hydrophilic compounds, a property that makes it particularly useful in drug discovery studies. It is common practice to use DMSO at low concentrations, however, at high concentration it is known to potentially affect protein conformation and consequently impair the catalytic activity [45].

Therefore, it was essential to first verify that DMSO itself did not exert any significant effect on the enzyme activity.

The range of DMSO concentrations tested varied between 0.035% v/v and 5% v/v inside the PMMA test cuvette. To reach the desired concentrations inside the cuvette, pure DMSO was previously diluted using the same 0.1 M pH 7.4 potassium phosphate buffer previously prepared.

The blank and the sample cuvette contained the following components:

- 2.7 mL of 0.1M pH 7.4 potassium phosphate buffer
- 100 µL of NADH solution
- 100 µL of pyruvate solution
- 10 µL of DMSO solution

The tested concentration of substrate and cofactor were the same as those without DMSO and all the data points were obtained in triplicate.

Analogous to the experiments conducted without DMSO, measurements were initiated upon the addition of the enzyme to the sample cuvette.

The assays were conducted at 37°C and at 7.4 pH, and magnetic stirring was provided to the samples throughout the monitoring of absorbance variation.

2.1.2.3 Effect of different inhibitors on the activity of the enzyme

The impact of five different LDH inhibitors on the enzyme kinetics was then investigated. Understanding the type, whether competitive, non-competitive or mixed, and strength of inhibition is crucial. This knowledge is directly relevant given that the biosensor's primary purpose is to aid in the screening of potential inhibitors.

The inhibitors evaluated were: Galloflavin, NHI-2, Oxamate, FX-11, Gossypol. Each of the tested compound was first solubilized in DMSO and the inhibitor solutions were subsequently added to the reaction mixture under the same experimental conditions described previously.

The composition of the blank and sample cuvettes was as follows:

- 2.7 mL of 0.1M pH 7.4 potassium phosphate buffer
- 100 µL of NADH solution
- 100 µL of pyruvate solution
- 10 µL of inhibitor solution in DMSO

The range of inhibitors concentrations tested varied between 1 µM and 40 µM for Oxamate, Gossypol and NHI-2; for FX-11 and Galloflavin the range was between 1µM and 20 µM.

The experimental protocol employed in this set of experiments was consistent with the procedures previously described.

These measurements were crucial not only for generating kinetic curves and observing how kinetic parameters changed in the presence of various inhibitors, but also for calculating the inhibition constant (K_i). K_i is a thermodynamic parameter, describing the binding affinity between an inhibitor and the enzyme and serves as a quantitative indicator of an inhibitor's potency. In fact, it represents the concentration represents the concentration at which the inhibitor ligand occupies 50% of the receptor sites. A lower K_i value signifies a greater binding affinity and, consequently, a lower amount of inhibitor needed to effectively inhibit the enzyme [46]. Thus, K_i is a valuable parameter for comparing the inhibitory potential of different compounds.

In the present work, K_i was calculated using two complementary methods: an analytical approach and one non-linear regression method.

In the analytical approach K_i was calculated exploiting the Equations shown in Figure 23. This method was applied after the elucidation of the inhibition mechanism, determined through changes in the kinetic parameters (V_{max} and K_m) and corroborated by molecular docking.

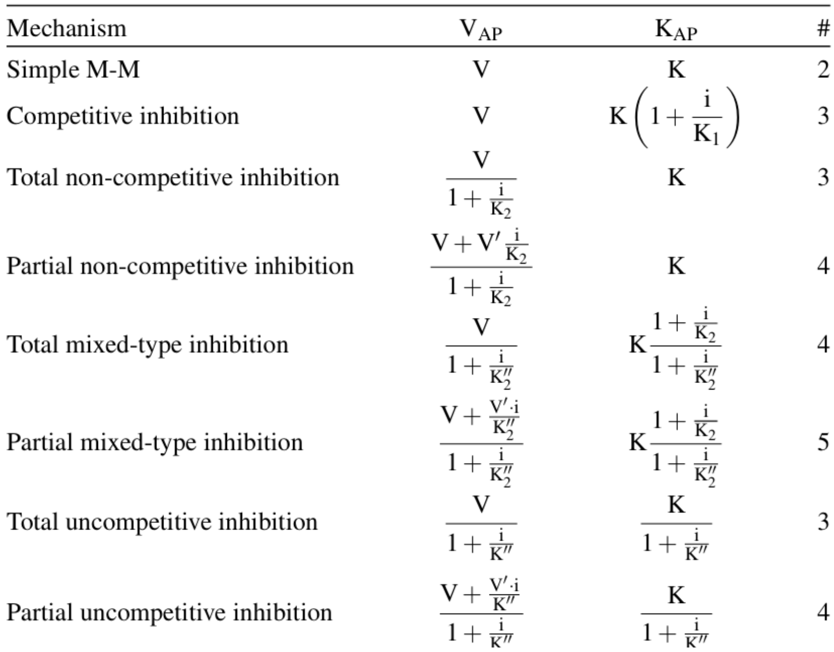

Mechanism	V_{AP}	K_{AP}	#
Simple M-M	V	K	2
Competitive inhibition	V	$K\left(1+\frac{i}{K_1}\right)$	3
Total non-competitive inhibition	$\frac{V}{1+\frac{i}{K_2}}$	K	3
Partial non-competitive inhibition	$\frac{V+V'\frac{i}{K_2}}{1+\frac{i}{K_2}}$	K	4
Total mixed-type inhibition	$\frac{V}{1+\frac{i}{K''_2}}$	$K\frac{1+\frac{i}{K_2}}{1+\frac{i}{K''_2}}$	4
Partial mixed-type inhibition	$\frac{V+\frac{V'\cdot i}{K''_2}}{1+\frac{i}{K''_2}}$	$K\frac{1+\frac{i}{K_2}}{1+\frac{i}{K''_2}}$	5
Total uncompetitive inhibition	$\frac{V}{1+\frac{i}{K''}}$	$\frac{K}{1+\frac{i}{K''}}$	3
Partial uncompetitive inhibition	$\frac{V+\frac{V'\cdot i}{K''}}{1+\frac{i}{K''}}$	$\frac{K}{1+\frac{i}{K''}}$	4

Figure 23. Values of apparent kinetic parameters for different kinetic models [15].

In Figure 23, K_2 and K_1 correspond to K_i, V_{AP} and K_{AP} represent the V_{max} and K_m associated with each inhibitor concentration tested, while V and K represent the V_{max} and K_m without the inhibitor. Consequently, five K_i values were obtained for each inhibitor, reflecting the number of inhibitor concentrations examined. This approach therefore yielded a range of K_i values rather than a single value.

In contrast, the non-linear regression approach involved fitting the experimental data with a model consistent with the previously identified inhibition mechanism. The data were organized as an XY data table, where the substrate/cofactor concentration represented the X column while the enzyme activity, at a specific inhibitor concentration, including a control, namely 0 µM inhibitor, corresponded to the Y columns. Each column was labelled with the corresponding inhibitor concentration. This fitting was performed using GraphPad Prism, a scientific 2D graphing and statistical analysis software. The aforementioned structure of the dataset was detailed in GraphPad Prism manual [47]. As distinct from the previous approach, this method yielded a single K_i value per inhibitor, summarizing its overall inhibitory effect under the tested conditions.

2.1.3 Incubation

To further investigate the enzyme's overall behaviour, incubation experiments were performed to evaluate the time-dependent effects of temperature and DMSO exposure on enzyme kinetics. These studies aimed to simulate long-term reaction environments and assess enzymatic stability or possible inactivation. Enzyme inactivation is the process in which the native structure of the enzyme becomes completely unfolded, leading to a loss of activity and consequently to an inactive form of the enzyme.

The enzyme thermal inactivation is the consequence of the weakening of the intermolecular interactions that are essential for the integrity of their tertiary structure, thereby causing a reduction in their catalytic activity. Enzyme inactivation by exposure to the reaction temperature is often unavoidable, since enzyme activity increases with temperature, but enzyme stability decreases. Consequently, the operation temperature should be chosen balancing the two factors [15]. Concerning the impact of DMSO on the enzyme, exposure to high DMSO concentrations induces alterations in the enzyme's conformation, thereby diminishing its catalytic activities. [45]. Given that the tested inhibitors were solubilized in DMSO, it was crucial to investigate the overtime effects of the solvent on the enzyme activity.

For both incubation assays, the enzyme was stored for up to three days and measurements were taken at specific time points with progressively increasing intervals. During temperature incubation test, the enzyme was kept at 37° and the composition of the blank and sample cuvettes was as follows:

- 2.71 mL of 0.1M pH 7.4 potassium phosphate buffer
- 100 µL of 0.23 mM NADH solution
- 100 µL of 1.63 mM pyruvate solution

At defined time step, an aliquot of 100 µL of the enzyme solution were collected from the 37°C water bath and inserted in the cuvette to measure the enzyme’s activity.

The DMSO incubation test was performed in the same conditions and the DMSO concentration was 46.78 mM. This concentration was chosen under the assumption that, as in the kinetic experiments, the 10 µL of added solution contain only pure DMSO. By using this volume, it is assumed that in future experiments involving enzyme-inhibitor interactions, the maximum DMSO concentration the enzyme may be exposed to corresponds to the scenario in which no inhibitor is actually dissolved in the DMSO. This approach establishes a conservative upper limit for DMSO exposure. The blank and the sample cuvette contained the following components:

- 2.7 mL of 0.1M pH 7.4 potassium phosphate buffer
- 100 μL of 0.23 mM NADH solution
- 100 μL of 1.63 mM pyruvate solution
- 10 μL of inhibitor solution in DMSO

The measurement procedure followed the methodology described previously.

The residual enzymatic activity at each time point was calculated from the collected data using the following equation:

$$Residual\ activity = \frac{A_{LDH\,incubated}}{A_{LDH,initial}} * 100 \qquad \text{Equation 8.}$$

Where:

- $A_{LDH\,incubated}$: absorbance slope registered at every time step (-)
- $A_{LDH,initial}$: absorbance slope before incubation (-)

The absorbance values of Equation 8 refer to the initial slope of the absorbance variation curve registered by the spectrophotometer.

Subsequently two models of enzyme inactivation were applied to fit the data collected:

$$A = A_0 * e^{-k_D * t} \qquad \text{Equation 9.}$$

$$A = A_0[(1-\alpha) * e^{-k_D * t} + \alpha] \qquad \text{Equation 10.}$$

Where:

- A_0: initial activity (-)
- k_D: deactivation constant (h^{-1})
- t: time (h)
- α: residual activity at infinite time (-)

In the first model, the inactivation is described by a hypothetical irreversible chemical reaction in which the first order inactivation rate constant is k_D [15]. This model allows to correlate (Equation 9) the experimental data with time using one parameter, namely deactivation constant, or k_D, and the obtained inactivation curve is an exponential decreasing curve that asymptotically tends to zero. Whereas the second model introduces another parameter: the residual activity at infinite time (α), accounting for a non-zero residual activity at infinite time. The Equation 10 describes a rapid initial loss of activity followed by a plateau or a much slower decline towards this residual value.

Understanding enzyme inactivation under process-relevant conditions is essential for evaluating long-term enzyme performance. Even for highly stable enzymes could undergo inactivation during extended reaction operation, due to unavoidable thermal or solvent-induced denaturation, leading to a significant reduction of the initial activity.

2.2 Molecular docking

Molecular docking enabled the identification of specific residues involved in ligand binding and corroborated the expected mechanism of inhibition, considering the characteristics of the molecules and the type of interactions formed with the enzyme.

A comprehensive analysis of the interactions between LDH and its ligand, namely pyruvate, NADH, DMSO and the five different inhibitors also tested during the enzymatic assays, was performed using UCSF ChimeraX [48]. ChimeraX is a highly extensible software for interactive visualization and analysis of molecular structures and related data, including density maps, docking results and conformational ensembles. This software enables the generation of high-quality images and animations. It has a core that provides visualization and basic services. In addition, it is possible to implement extensions with higher-level functionality like ViewDock and Volume Viewer [49].

In order to perform the docking analysis an extension called Autodock Vina [50] was added to ChimeraX. It is one of the fastest and most widely used open-source docking engines, recognized for its speed and accuracy of results. The computational docking program is based on a simple scoring function and on rapid gradient-optimization conformational search. "Docking consists in generating multiple poses of the molecule at the surface of the target and determining the most favourable pose in terms of ligand-target interaction energy, conformational energy and possibly also desolvation energy. Ideally, but not necessarily, the docking software can estimate the small molecule binding free energy for the target to facilitate the identification of potential ligands. This predictive modelling approach speeds up the drug discovery process and reduces experimental costs" [51].

The methodology for determining the optimal docking configuration can be summarized as follows:

1) Protein ID and structure retrieval from the protein database, like the Protein Data Bank, as a PDB file.
2) Visualization of the protein structure in UCSF Chimera.
3) Preparation of the target protein and the ligand for docking. The preparatory stage includes:
    - Removal of water molecules to avoid interference with the docking.
    - Addition of missing polar hydrogen atoms, necessary to identify atom types for scoring purposes.
    - Assignment of partial charges to the atoms.

    These preparatory steps were performed automatically within UCSF ChimeraX.

4) Docking of the target protein and the ligand using Autodock Vina. This step is characterized by the definition of a grid box around the target protein. In this way the possible coupling will be searched only in the predefined area.
5) Interpretation and analysis of the docking outcome.

The output consists of a list of root-mean-square deviation (RMSD) values, calculated relative to the most favourable binding pose and considering only movable heavy atoms. The RMSD is a way to measure the degree of similarity of two protein three-dimensional structures The RMSD is a widely accepted metric in structural biology, used to quantify the degree of similarity of two protein three-dimensional structures, by comparing atomic coordinates [52]. A lower value of RMSD indicates a better fit or agreement between the two structures considered. Two variants of RMSD metrics were reported: RMSD lower bound (rmsd/lb) and RMSD upper bound (rmsd/ub), which differ in how the atoms are matched in the distance calculation. The RMSD values generated a list of ten distinct ligand poses, ordered by increasing RMSD. From this set, only the top pose, characterized by the lowest RMSD value, was retained for further analysis. Subsequently, the "Hbonds" functionality within ChimeraX was used to identify intermolecular hydrogen bonds between LDH and the ligand. This identification of hydrogen bonds proved crucial for pinpointing the specific residues involved in the binding interaction.

3. Results

3.1 Spectrophotometric analysis results

The initial findings from the spectrophotometric are illustrated in Figure 24.

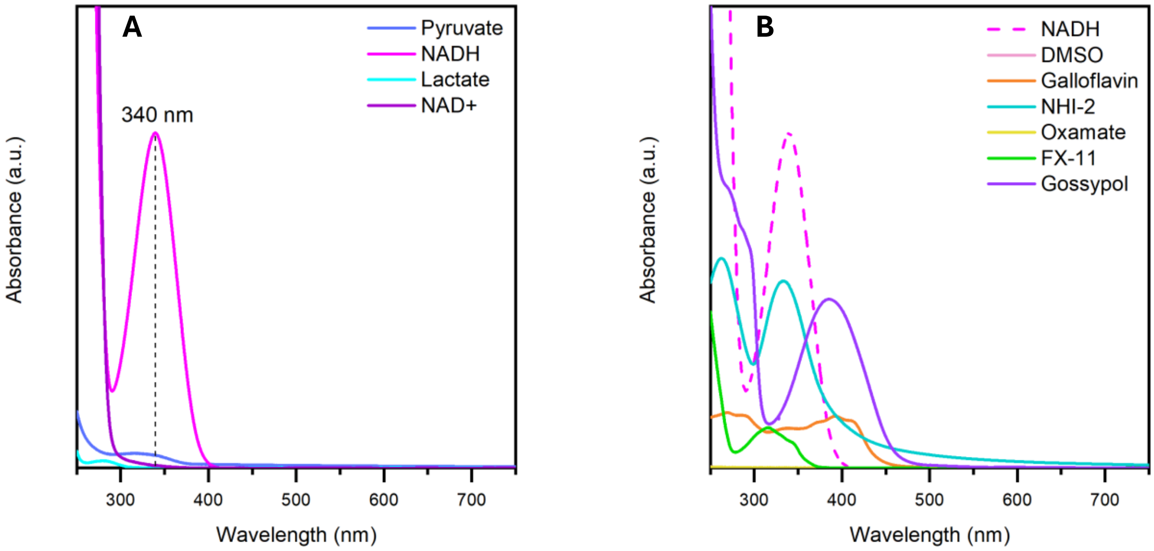

Figure 24. Absorbance spectra of the different compound tested.

Figure 24A displays the absorbance spectra of the main compounds involved in the LDH-catalyzed reaction. These measurements were crucial for determining the optimal wavelength for subsequent kinetic assays. It was immediately evident that NADH exhibits a distinct absorbance peak at 340 nm. Conversely, NAD+, and lactate did not show absorbance at this wavelength. Pyruvate exhibited minimal absorbance, but, given the absorbance intensity, it is reasonable to assume that it can be neglected. Since no interference between main reactants or product was evident at 340 nm, this wavelength was therefore selected for all future measurements to ensure maximum sensitivity and the strongest measurable response. As clarified in “Materials and Methods” section, the molar ratio between NADH consumption and lactate production is equal to 1, so NADH can effectively be the analyte, whose concentration allows to monitor the proceeding of the enzymatic reaction.

Figure 24B presents the absorbance spectra of NADH alongside those of DMSO and the inhibitors. Having established that NAD+, lactate and pyruvate do not exhibit significant absorbance within the analyzed spectral range (Figure 23A), the spectrum in Figure 23B focuses on potential spectral overlap between NADH and the possible inhibitors. As observed, neither DMSO nor Oxamate produced a significant signal. The lack of absorbance at 340 nm observed for both DMSO and Oxamate can be attributed to the absence of extended conjugated systems or aromatic chromophores in their molecular structures. DMSO, in fact, absorbs only in the far-UV region due to n→σ transitions involving the sulfur–oxygen bond, typically below 265 nm [53]. Galloflavin displayed minor absorbance in the UV-Vis visible range, consistent with its flavonoid-like structure containing aromatic rings and hydroxyl groups [54]. Also FX-11 showed only a small absorbance at 340 nm when compared to NADH's signal. Even if it contains aromatic rings, it lacks complex conjugation, so its UV absorbance is limited. By contrast, Gossypol, being a polyphenolic aldehyde, exhibited a broad absorption spectrum, due to its extensive conjugated aromatic system and multiple hydroxyl groups, with a peak at 400 nm [55]. Despite the peak not being centred at 340 nm, the tail of the absorption band extends into the 340 nm region, resulting in a measurable, albeit weaker, signal. NHI-2, however, showed substantial absorbance at 340 nm. Although no detailed UV-visible spectrum is available in the literature, the observed spectral data are coherent with the presence of extended conjugation or chromophoric groups within NHI-2 molecular structure, absorbing in this region. This absorption peak could indicate a potential for interference with the NADH signal. To further assess this interference, absorbance spectra of NADH at lower concentrations were also measured, with the results detailed in Figure 25.

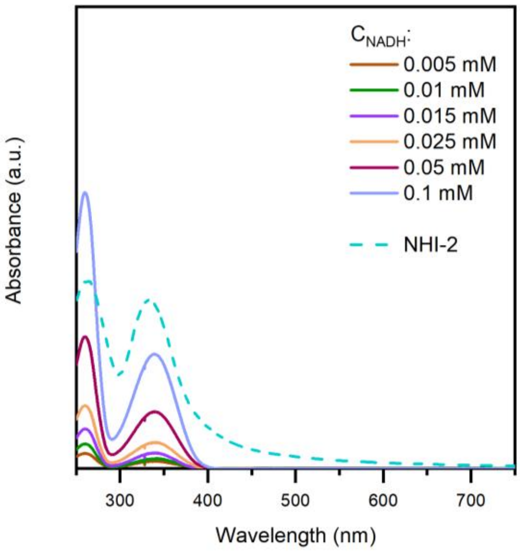

Figure 25. Absorbance spectra of NHI-2 and of NADH at different concentrations.

Figure 25 reveals significant interference from NHI-2. Indeed, NHI-2 absorbance signal exceeded those of NADH at all tested concentration, except for the 0.1 mM NADH. This finding suggested that during enzyme catalytic activity measurements, when NADH concentrations will be varied in the presence of NHI-2, absorbance readings at lower NADH levels might be significantly distorted. Conversely, when catalytic activity will be measured in the presence of NHI-2 by varying pyruvate concentration at a fixed NADH concentration of 0.23 mM, interference from NHI-2 may still occur, but is expected to be less pronounced. It is also important to note that NADH exhibited a second absorption peak at 260 nm, which, in principle, could have been used to monitor the reaction. However, this peak overlapped with that of NAD+ [56], creating potential complications in the interpretation of the data. Specifically, during the reaction, the decrease in NADH concentration would lead to a reduction in absorbance at 260 nm, while the simultaneous formation of NAD+ would cause an increase in absorbance at the same wavelength. These opposite effects would compromise accurate assessment of the reaction progress. Furthermore, the 260 nm peak was not observable in Figure 24A due to the high NADH concentration used in the experiment and in the subsequent enzymatic assays, which saturated the spectrophotometer.

3.2 Enzyme activity and molecular docking results

3.2.1 Apparent parameters of the intrinsic activity of the enzyme

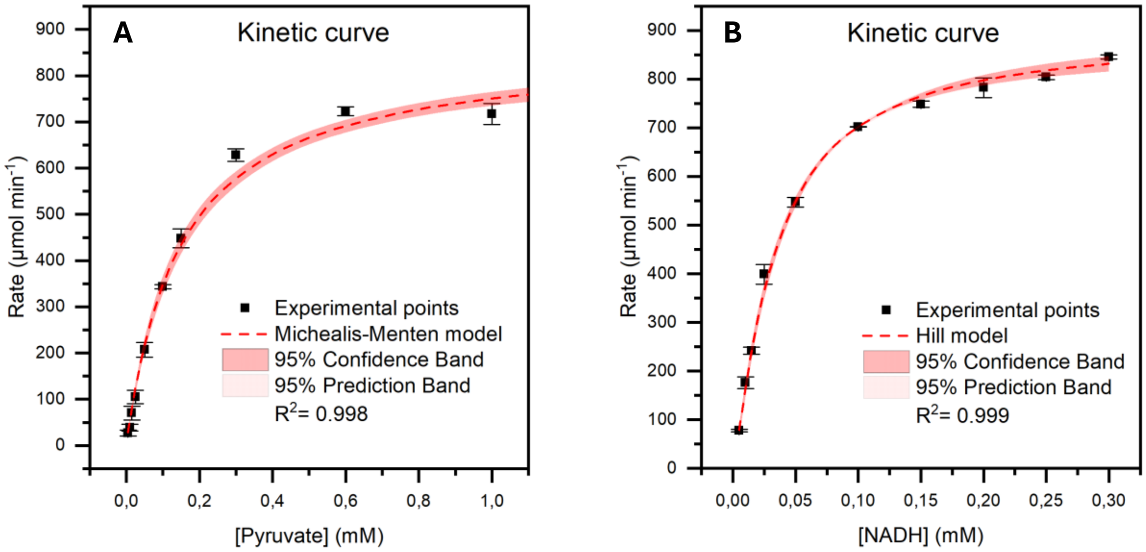

Figure 26. Visual representation of the kinetic curves of LDH at a fixed cofactor concentration (22A) and at a fixed substrate concentration (22B).

Figure 26 illustrates the preliminary kinetic curves of LDH activity. The kinetic curves are plotted as initial velocities, representing the rate of product formation as a function of substrate or cofactor concentration.

Figure 26A was obtained at a fixed cofactor concentration of 0.23 mM and it was fitted using Michaelis-Menten model. Conversely, Figure 26B shows the curve generated at a fixed substrate concentration equal to 1.63 mM, fitted with the Hill model. The high R^2 values observed in both cases underscore excellent agreement between the model and the experimental data. These curves were crucial, as they served as the foundational reference for all subsequent measurements.

Data analysis and curve fitting were performed using OriginPro software, which also facilitated the derivation of the kinetic parameters summarized in Table 6.

Table 6. Kinetic parameters of the curves function of pyruvate and function of NADH.

	Pyruvate kinetic parameters	NADH kinetic parameters
V_{max} [μmol min^{-1}]	861 ± 5	891 ± 6
K_m [mM]	0.147 ± 0.004	0.034 ± 0.001
n [-]	-	1.21 ± 0.02

Table 6 reveals a Hill coefficient (n) greater than one, indicative of positive cooperativity between enzyme and NADH. LDH is a tetrameric enzyme, with each subunit containing an active site for both pyruvate and NADH. A positive cooperativity implies that the binding of NADH to one subunit of the enzyme enhances the affinity of the remaining subunits for the binding of subsequent ligands [57].

For the curves obtained by varying substrate concentration, which were fitted to the Michaelis-Menten model, kinetic parameters were validated using both Lineweaver-Burk (Equation 4) and Hanes-Woolf (Equation 5) linearization methods. This was done to confirm the consistency and reliability of the calculated K_m and V_{max} values. Figure 27 presents the two linearizations, while Table 7 shows the subsequent kinetic parameters derived.

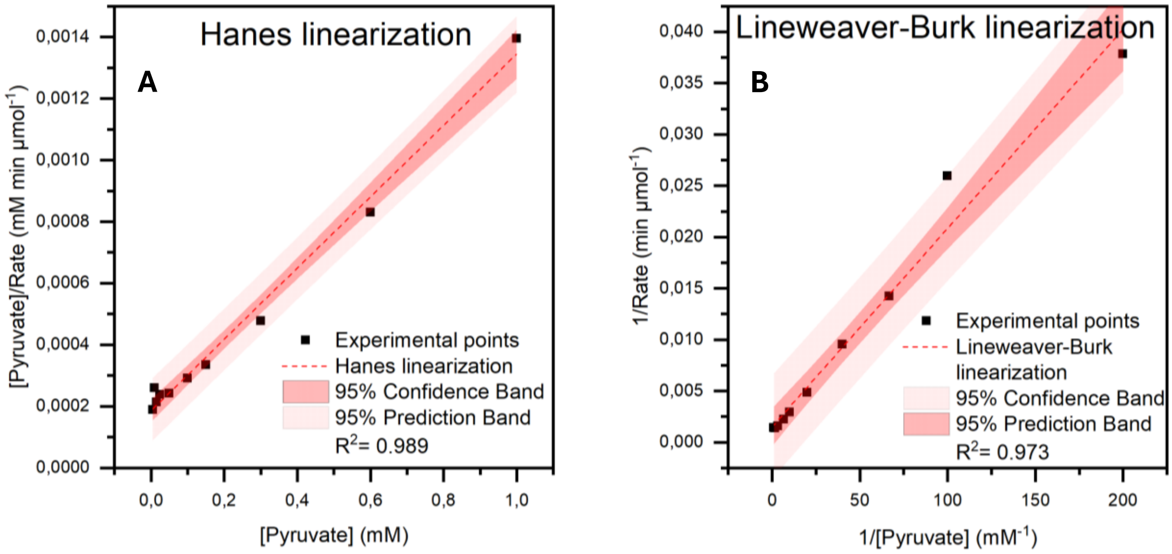

Figure 27. Hanes and Lineweaver-Burk linearizations.

Table 7. Kinetic parameters derived with Hanes-Woolf and Lineweaver-Burk linearization methods.

	Hanes-Woolf	Lineweaver-Burk
V_{max} [μmol min^{-1}]	864	678
K_m [mM]	0.160	0.131

As shown in Table 7, the Hanes-Woolf linearization method yielded values in good agreement with those derived from the non-linear regression performed with OriginPro. However, the parameters from Lineweaver-Burk linearization showed considerable discrepancies.

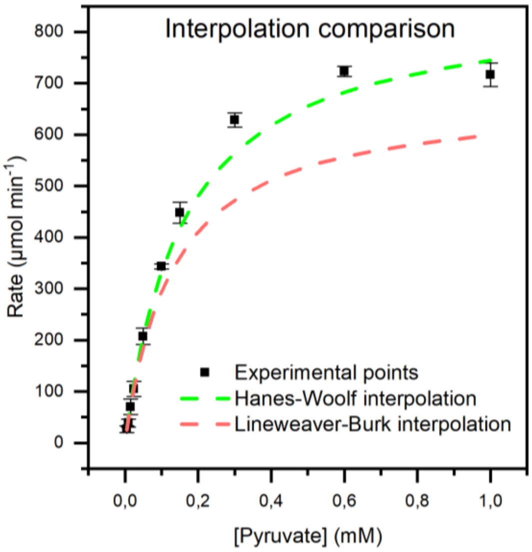

Figure 28. Interpolation with Hanes-Woolf and with Lineweaver-Burk derived parameters.

Figure 28 provides further evidence supporting the previous statements. This figure compares experimental data points with interpolated curves derived from the parameters obtained with two different linearization methods. While the Hanes-Woolf derived interpolation accurately followed the experimental progression, the Lineweaver-Burk method did not.

As will be discussed later, the Lineweaver-Burk method does not appear to be the optimal linearization for deriving these kinetic parameters. In fact, Lineweaver-Burk linearization method is known to be less reliable for the determination of kinetic parameters, particularly at low substrate concentrations. In this region, experimental errors become more significant due to limitations in measurement precision. These errors are disproportionately amplified due to the double reciprocal plot, often leading to distorted estimates of K_m and V_{max}. This limitation is evident in the discrepancies observed when comparing the parameters obtained via Lineweaver-Burk with those derived from nonlinear regression or alternative linearization methods such as Hanes-Woolf.

In the case of NADH, kinetic parameters were not validated through any form of linearization, as the Hill model is a three-parameter equation. Linearization of this model would require fixing at least one parameter, typically the Hill coefficient, which could introduce bias and compromise the accuracy of the parameter estimates. Therefore, nonlinear regression was deemed the most appropriate method for analyzing these data.

Molecular docking simulations were performed to better understand the binding interactions of LDH with pyruvate and NADH. The docking results are shown in Figure 29 and Figure 30. As ChimeraX exclusively identifies hydrogen bonds, the visualized interactions in the docking results are limited to this type of bonding and do not include other non-covalent interactions such as van der Waals forces or π–π stacking.

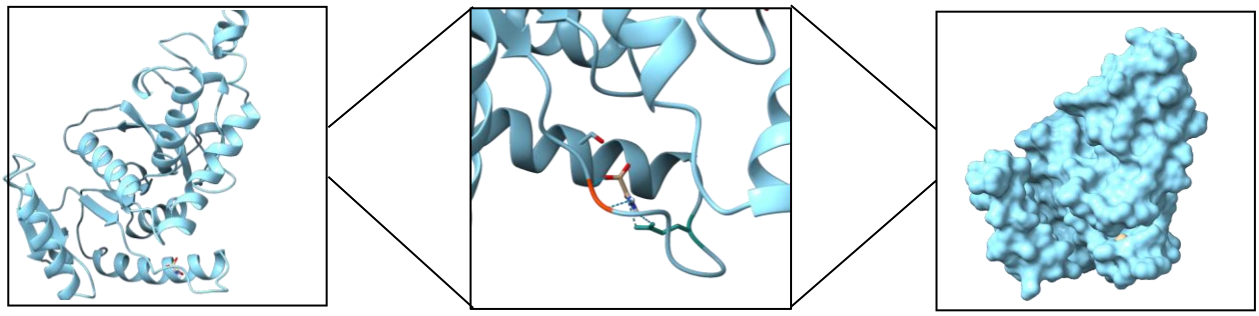

Figure 29. ChimeraX views of the binding between LDH and pyruvate.

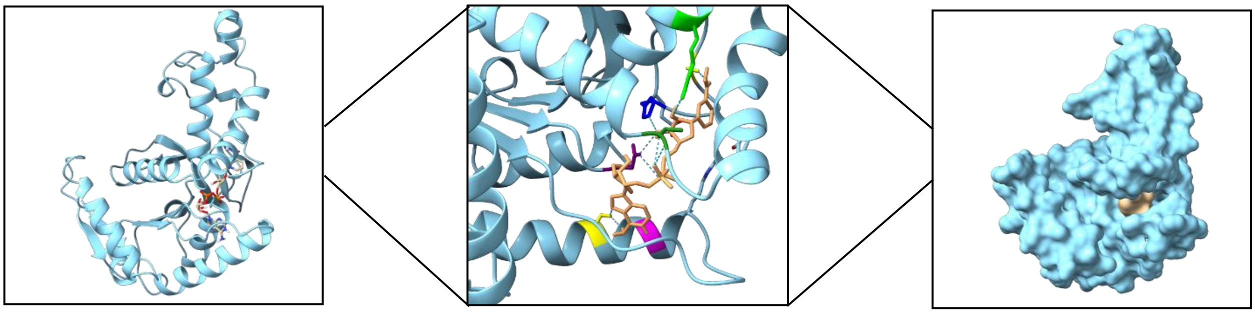

Figure 30. ChimeraX views of the binding between LDH and NADH.

Figure 29 and Figure 30 illustrates the binding of LDH with pyruvate and NADH, respectively. Pyruvate was observed to interact primarily with Methionine 53 (orange) and Glutamine 59 (water green) residues, while NADH with Arginine 124 (light green), Serine 68 (yellow), Serine 152 (yellow), Threonine 203 (green), Histidine148 (blue) and Asparagine 93 (violet) residues.

3.2.2 Generic parameters of the intrinsic activity of the enzyme

Following the experimental described in the “Materials and Methods” Section, kinetic curves at other three fixed cofactor concentration were derived. The experimental points, fitted with Michaelis-Menten model, are shown in Figure 31. Subsequently, for each curve, apparent kinetic parameters were calculated and then used to create the secondary plots, shown in Figure 32.

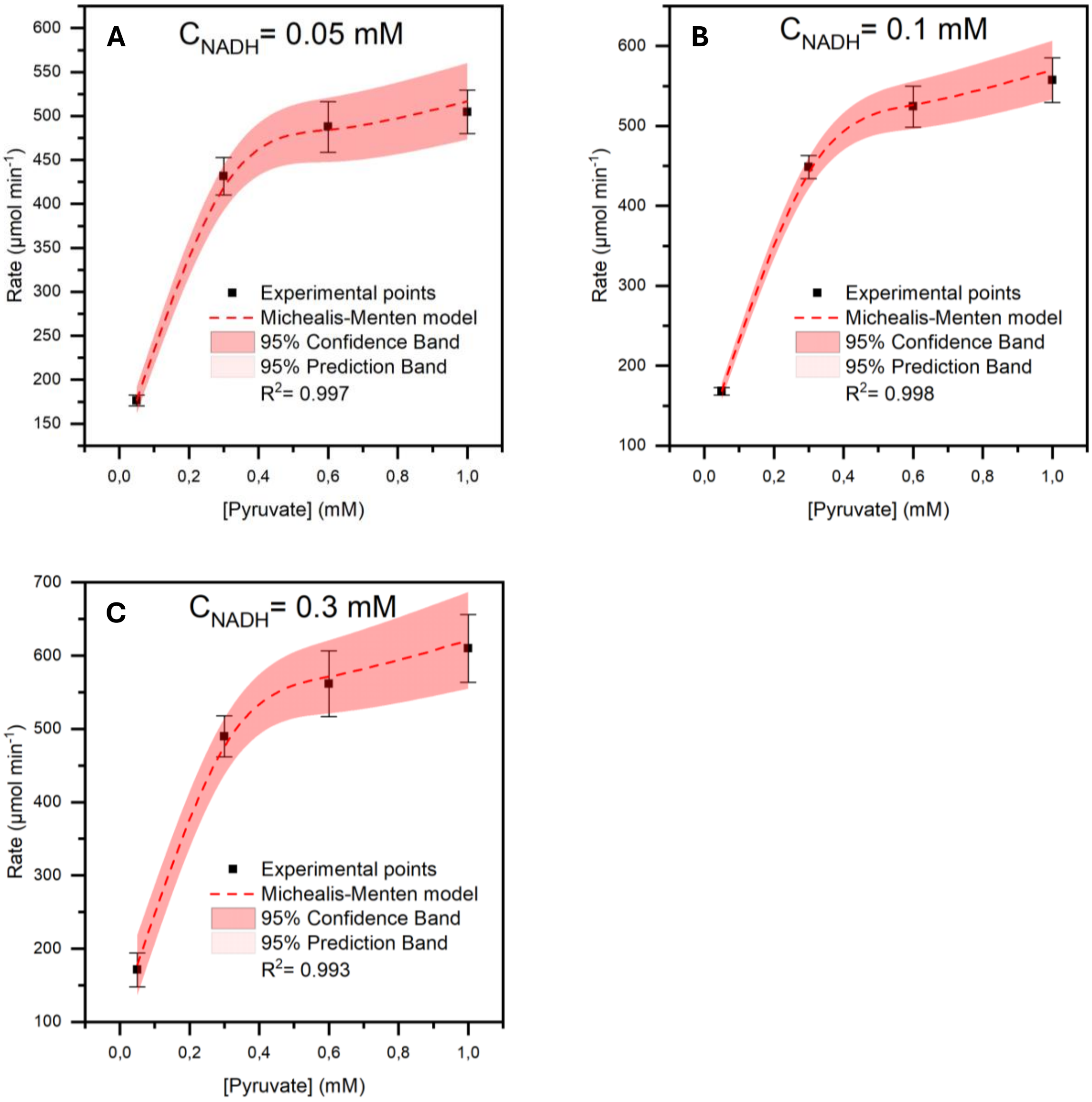

Figure 31. Kinetic curves at three different fixed cofactor concentrations of 0.05 mM (31A), 0.1 mM (31B) and 0.3 mM (31C).

Table 8. Kinetic parameters of the curves function of pyruvate at different NADH concentrations.

	Pyruvate kinetic parameters	
C_{NADH} [mM]	V_{max} [μmol min^{-1}]	K_m [mM]
0.05	575 ± 24	0.112 ± 0.01
0.1	652 ± 24	0.143 ± 0.01
0.23	861 ± 5	0.147 ± 0.004
0.3	714 ± 54	0.15 ± 0.03

Table 8 summarizes the apparent kinetic parameters used to create the secondary plots. The parameters refer to the kinetic curves as a function of pyruvate concentration and at a fixed NADH concentration.

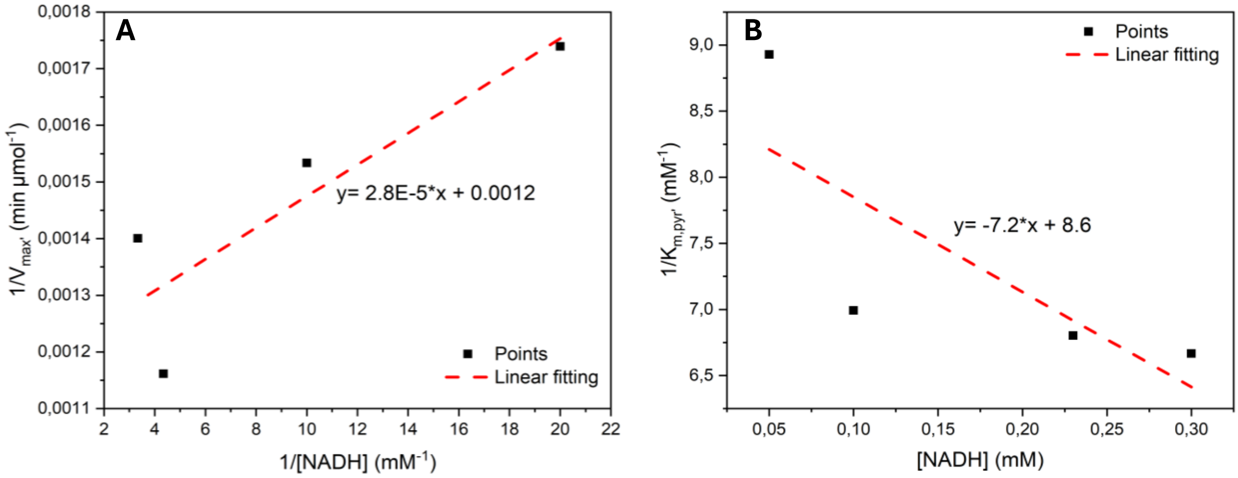

Figure 32. Secondary plots of the curves at a fixed cofactor concentration.

The plot of Figure 32 displays the linear fit of four data points, each derived from a single curve at a specific cofactor concentration. Linear regression of these data provided the equation for the dashed fitting line. The intercept of the resulting equation was subsequently used to determine the true values of V_{max} in one instance and K_m, in the other, for pyruvate.

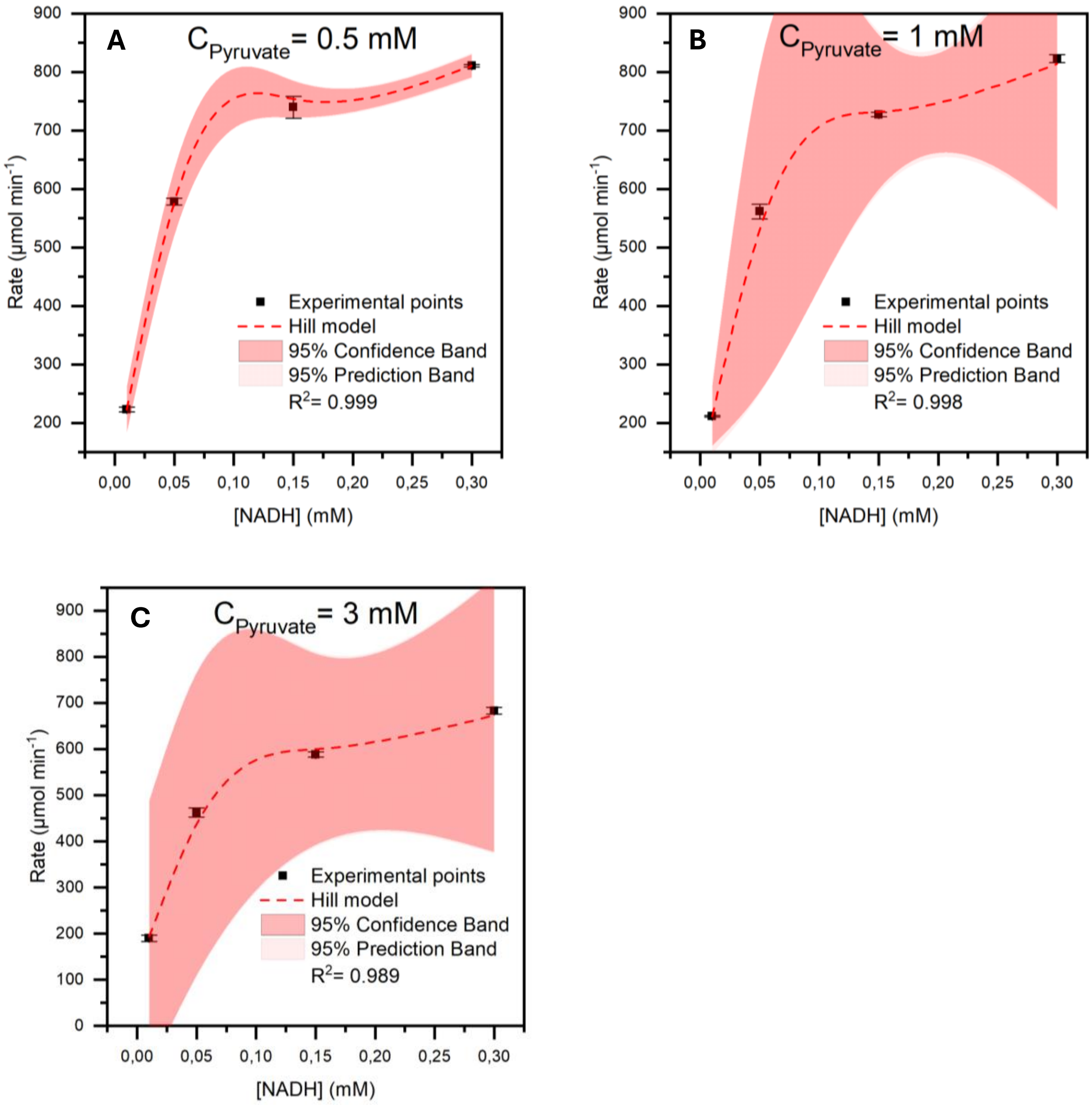

Figure 33. Kinetic curves at three different fixed substrate concentrations of 0.5 mM (29A), 1 mM (29B) and 3 mM (29C).

A similar procedure was followed to determine the actual kinetic parameters for curves with varying NADH and constant pyruvate concentrations. Figure 33 shows the resulting kinetic curves, each at a different fixed substrate concentration, fitted to a Hill model.

Table 9. Kinetic parameters of the curves function of NADH, at different pyruvate concentrations.

	NADH kinetic parameters		
$C_{Pyruvate}$ [mM]	V_{max} [µmol min^{-1}]	K_m [mM]	n [-]
0.5	869 ± 7	0.027 ± 0.001	1.08 ± 0.03
1	928 ± 24	0.037 ± 0.003	0.94 ± 0.03
1.63	891 ± 6	0.034 ± 0.001	1.21± 0.02
3	800 ± 32	0.04 ± 0.005	0.83 ± 0.05

Table 9 summarizes the apparent kinetic parameters used to create the secondary plots. The parameters refer to the kinetic curves as a function of NADH concentration and at a fixed pyruvate concentration.

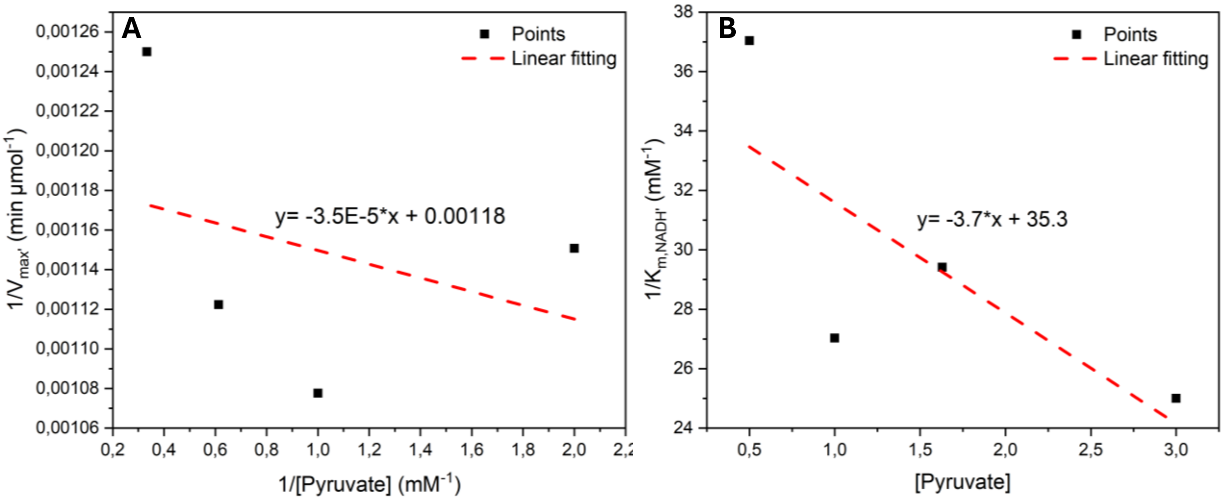

Figure 34. Secondary plots of the curves at a fixed substrate concentration.

Subsequently, the apparent kinetic parameters derived from the Figure 33 curves were used to construct the secondary plots shown in Figure 34. As previously explicate, each of the four points in these secondary plots was obtained from a single kinetic curve generated with a variable cofactor concentration and a fixed substrate concentration.

The true kinetic parameters for NADH were then derived from the y-intercepts of these graphs: Figure 34A's y-intercept provided the actual Vmax, while Figure 34B's y-intercept yielded the actual Km.

Table 10. Real LDH kinetic parameters.

	Pyruvate kinetic parameters	NADH kinetic parameters
V_{max} [µmol min^{-1}]	833	847
K_m [mM]	0.117	0.028

Table 10 presents the actual kinetic parameters derived from the secondary plots. A comparison with the values in Table 7 (apparent kinetic parameters) revealed that the true parameters were slightly lower than the apparent ones. Nevertheless, these values remained consistent and provided general insight into LDH kinetics in the presence of pyruvate and NADH.

To improve the reliability of these true parameters estimation, additional kinetic curves at fixed substrate or cofactor concentrations should be created in order to obtain secondary plots with an increased number of points to fit, thus increasing the fitting precision and the resulting kinetic constants.

3.2.3 Effect of DMSO on the activity of the enzyme

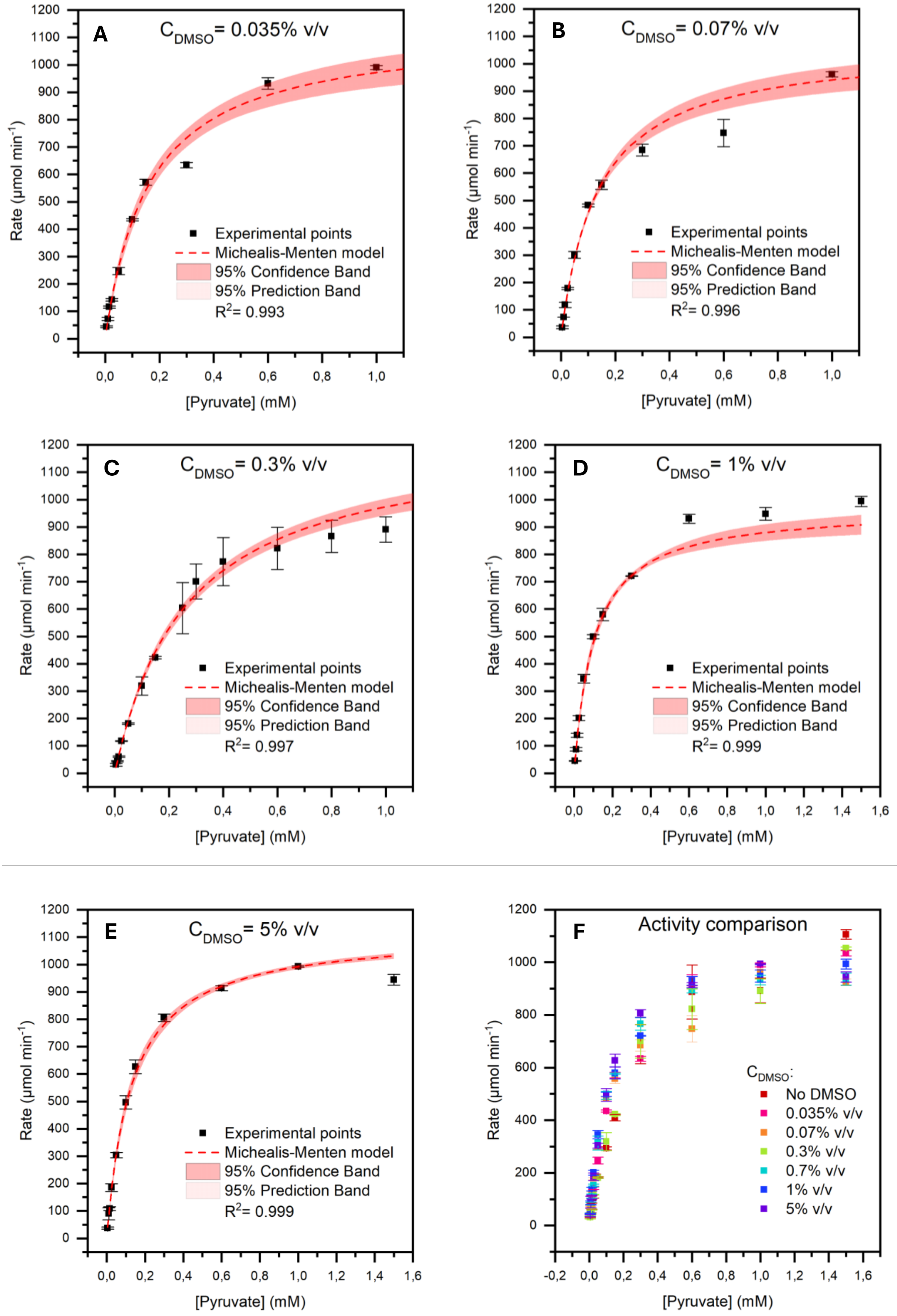

Figure 35. Kinetic curves function of pyruvate at different DMSO concentrations.

Figure 35 presents the LDH kinetic curves as a function of substrate concentration across varying DMSO concentrations. This step was crucial, as the inhibitors under investigation required dissolution in DMSO. Therefore, it was essential to first confirm that DMSO itself did not significantly affect enzyme activity. To this end, five DMSO concentrations were tested.

The concentration expected in the cuvette, when DMSO is added neat, in the same volumetric amount as the addition of the inhibitors, was 0.3% v/v, so this concentration was obviously tested and used as reference point. Additional concentrations were tested to assess whether excess DMSO would influence LDH kinetics. Concentration lower that the maximum expected in the assay were tested as well, to gain a complete overview of the solvent's impact on enzyme performances.

The experimental points were fitted with Michaelis-Menten model, which proved suitable, as indicated by R^2 values approaching 1.

Figure 35F consolidates all experimental data onto a single plot, clearly demonstrating that the kinetic behaviour at different DMSO concentrations replicated the trend observed in the absence of DMSO. Therefore, DMSO exerted no significant influence on LDH kinetics under the tested conditions.

Table 11. Summary of the kinetic parameters in presence of DMSO, obtained with OriginPro.

	PYRUVATE KINETIC PARAMETERS		
C_{DMSO} [% v/v]	**V_{max} [μmol min^{-1}]**	**K_m [mM]**	**R^2**
No DMSO	1201 ± 13	0.264 ± 0.003	0.995
0.035	1130 ± 8	0.162 ± 0.003	0.993
0.07	1068 ± 9	0.135 ± 0.001	0.996
0.3	1232 ± 7	0.265 ± 0.003	0.997
0.7	1085 ± 12	0.133 ± 0.003	0.998
1	970 ± 7	0.103 ± 0.004	0.999
5	1121 ± 5	0.130 ± 0.004	0.999

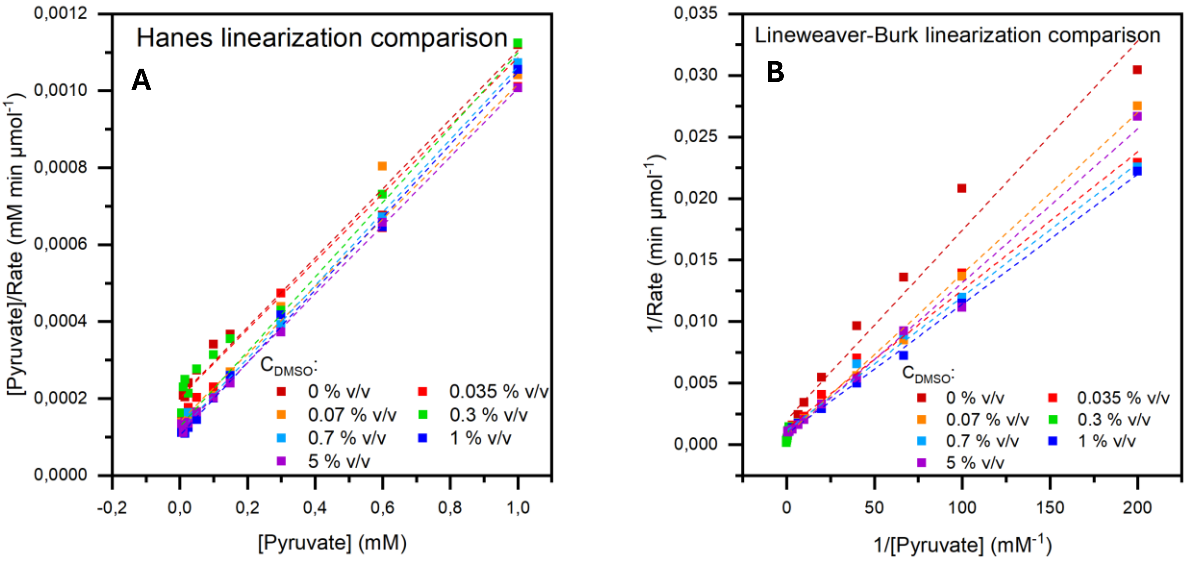

Figure 36. Hanes and Lineweaver-Burk linearizations.

Table 12. Summary of the kinetic parameters in presence of DMSO, obtained with Hanes-Woolf linearization.

	PYRUVATE KINETIC PARAMETERS					
	Hanes-Woolf			**Lineweaver-Burk**		
C_{DMSO} [% v/v]	**V_{max} [μmol min^{-1}]**	**K_m [mM]**	**R^2**	**V_{max} [μmol min^{-1}]**	**K_m [mM]**	**R^2**
No DMSO	1239	0.280	0.992	617	0.097	0.971
0.035	1144	0.161	0.996	749	0.084	0.990
0.07	1010	0.126	0.994	1320	0.173	0.997
0.3	1183	0.250	0.996	4726	3.99	0.991
0.7	1022	0.113	0.999	874	0.095	0.996
1	1065	0.110	0.999	1157	0.122	0.999
5	951	0.121	0.997	1467	0.183	0.991

Table 12 summarizes the kinetic parameters calculated with OriginPro. They revealed largely consistent Vmax values and minor variations in Km values. The parameters obtained through Hanes-Woolf linearization of Figure 36A, shown in Table 12, also demonstrated similar consistency and agreement with the OriginPro results. This observation reinforced the conclusion that DMSO, within the tested concentration range, does not interfere with LDH catalytic behaviour.

However, the Lineweaver-Burk linearization, shown in Figure 36B, yielded highly variable V_{max} and K_m values that were not comparable to those from other methods. This variability suggests the Lineweaver-Burk method is unsuitable for retrieving accurate kinetic parameters. As previously mentioned in the Introduction, its tendency to amplify experimental errors, particularly at low substrate concentrations, likely contributes to this issue.

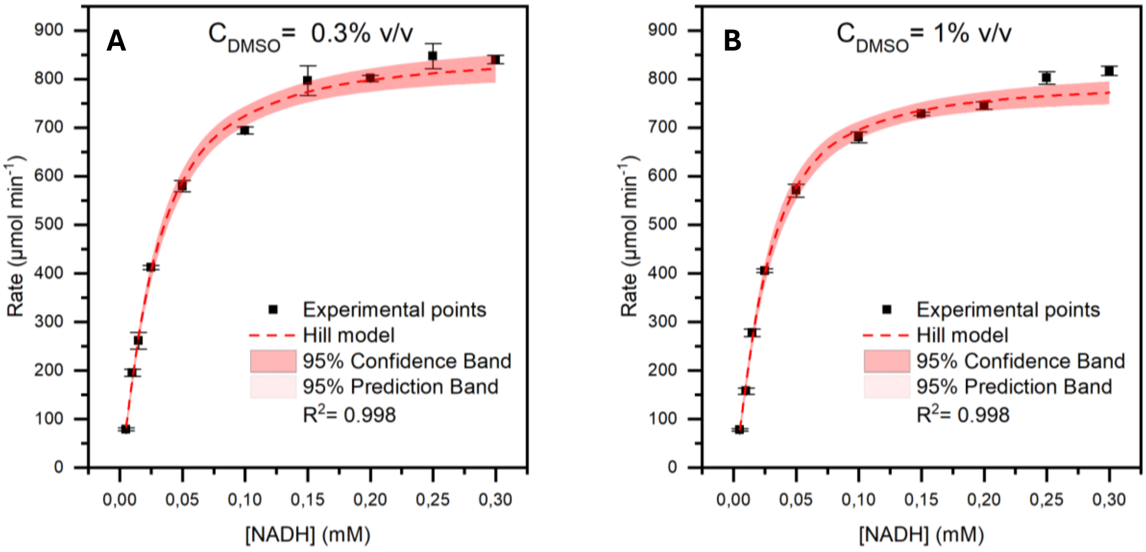

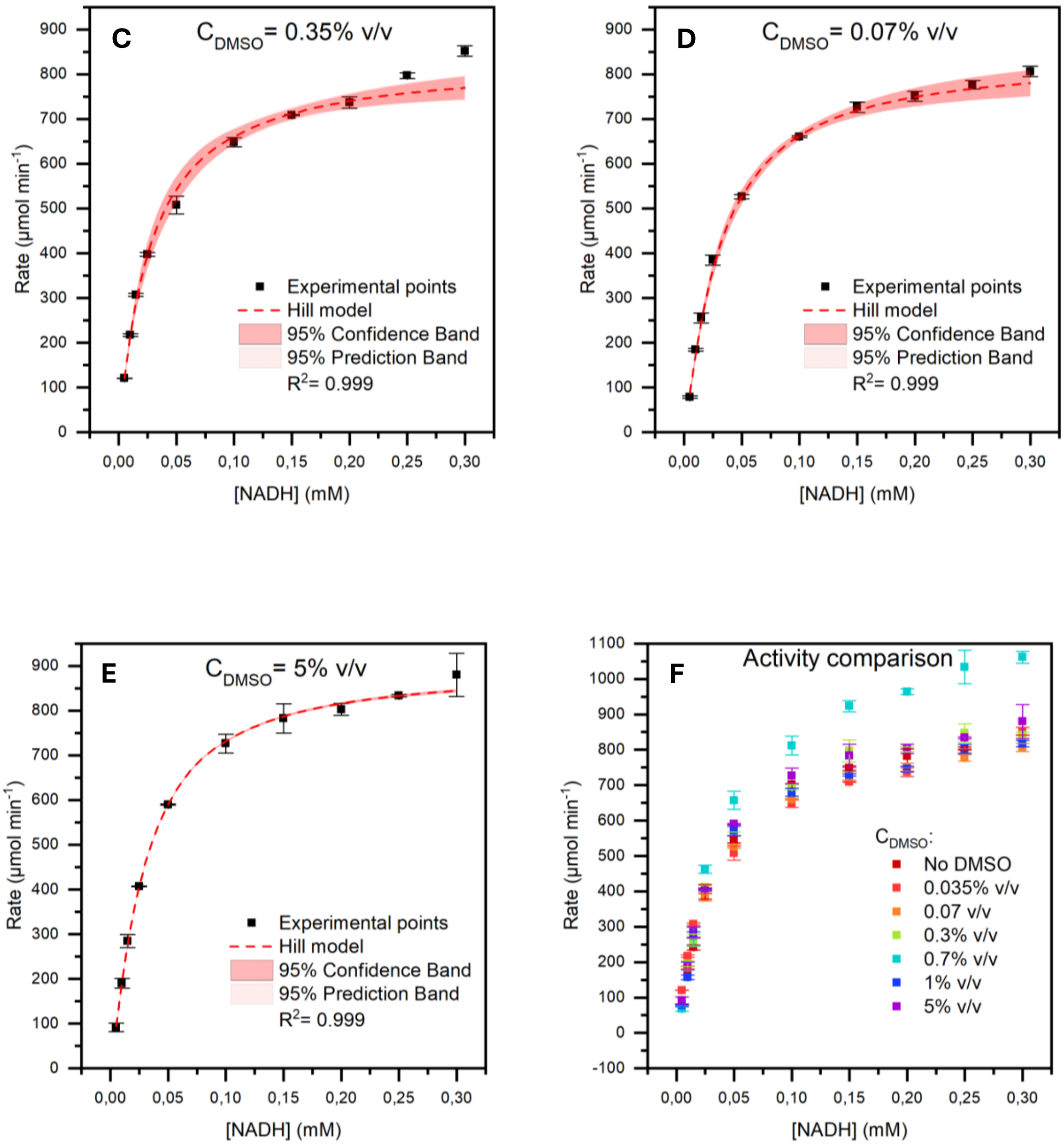

Figure 37. Kinetic curves function of NADH at different DMSO concentrations.

Figure 37 presents the LDH kinetic results as a function of cofactor concentration across different DMSO concentrations. As in the case for intrinsic kinetic curves, experimental points were fitted using Hill's model, which provided excellent fits as indicated by the high R^2 values.

Figure 37F highlights the overall kinetic behaviour observed at different DMSO concentrations. The only curve that appeared to deviate slightly from the general trend was at 0.7% v/v. Given that the expected trend was maintained at both lower and higher DMSO concentrations, so the deviation is likely attributable to experimental inaccuracies. Overall, these results confirm that presence of DMSO does not influence LDH kinetics, even when NADH concentration is the variable component.

Table 13. Summary of the kinetic parameters in presence of DMSO, obtained with OriginPro.

	NADH KINETIC PARAMETERS			
C_{DMSO} [% v/v]	**V_{max} [µmol min^{-1}]**	**K_m [mM]**	**n**	**R^2**
No DMSO	891 ± 6	0.034 ± 0.001	1.21 ± 0.02	0.999
0.035	933 ± 7	0.049 ± 0.001	1.72 ± 0.02	0.983
0.07	838 ± 10	0.031 ± 0.001	1.16 ± 0.02	0.999
0.3	857 ± 8	0.027 ± 0.001	1.30 ± 0.02	0.998
0.7	1051 ± 15	0.032 ± 0.001	1.36 ± 0.05	0.997
1	796 ± 5	0.025 ± 0.001	1.38 ± 0.03	0.998
5	894 ± 5	0.029 ± 0.001	1.21 ± 0.02	0.999

Table 13 summarizes the kinetic parameters derived from the NADH curves. As also observed in the graphical representation, the V_{max} value at 0.7% v/v was elevated compared to the other concentrations, again likely due to experimental inaccuracies. Conversely, the K_m values remained relatively constant, while the n values did not exhibit a defined trend, suggesting no systematic effect of DMSO on LDH's cooperative behaviour.

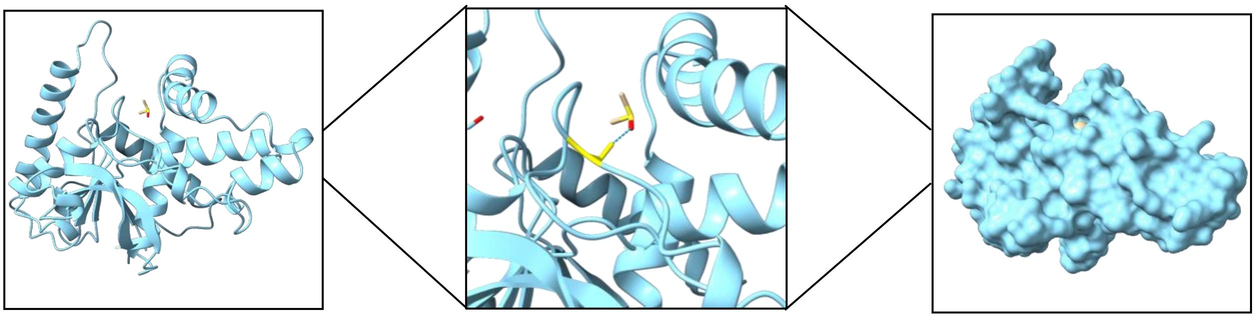

Figure 38. ChimeraX views of the binding between LDH and DMSO.

To complement the kinetic analysis, molecular docking simulations were performed. The results of DMSO docking are shown in Figure 38. DMSO interacts with Serine 151 residue, forming a hydrogen bond. As evident from Figure 39, DMSO (violet) does not interfere with the binding of pyruvate (red) and NADH (yellow). These findings collectively confirm that DMSO does not interfere with LDH kinetics, thus validating its use as a solvent for the inhibitors.

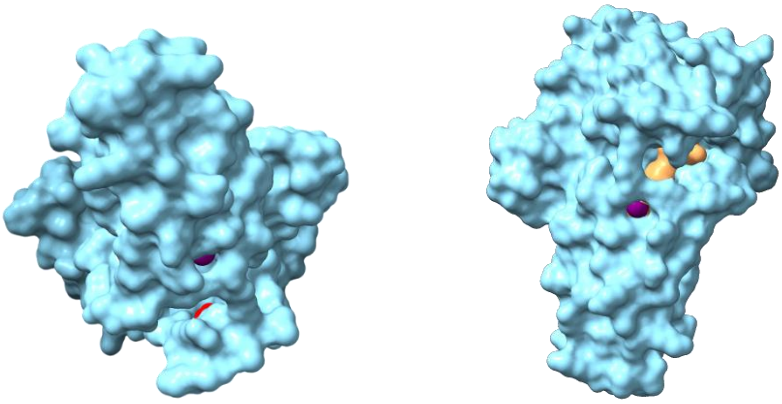

Figure 39. ChimeraX visual representation of LDH's surface with DMSO, NADH and pyruvate binding.

3.2.4 Effect of different inhibitors on the activity of the enzyme

Having established that DMSO does not significantly affect LDH kinetics and can therefore be safely used as a solvent, kinetic assays were subsequently conducted in the presence of the various inhibitors under investigation. The first to be examined was Galloflavin.

3.2.4.1 Galloflavin

Figure 40 presents the kinetic curves obtained by varying substrate concentration in the presence of increasing Galloflavin concentrations, ranging from 1 µM to 20 µM.

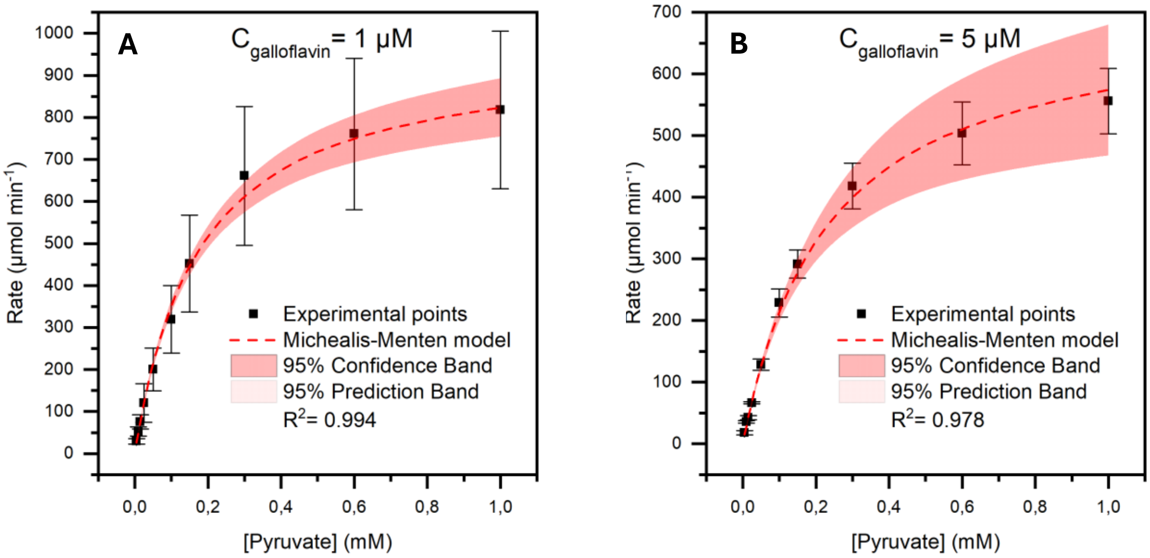

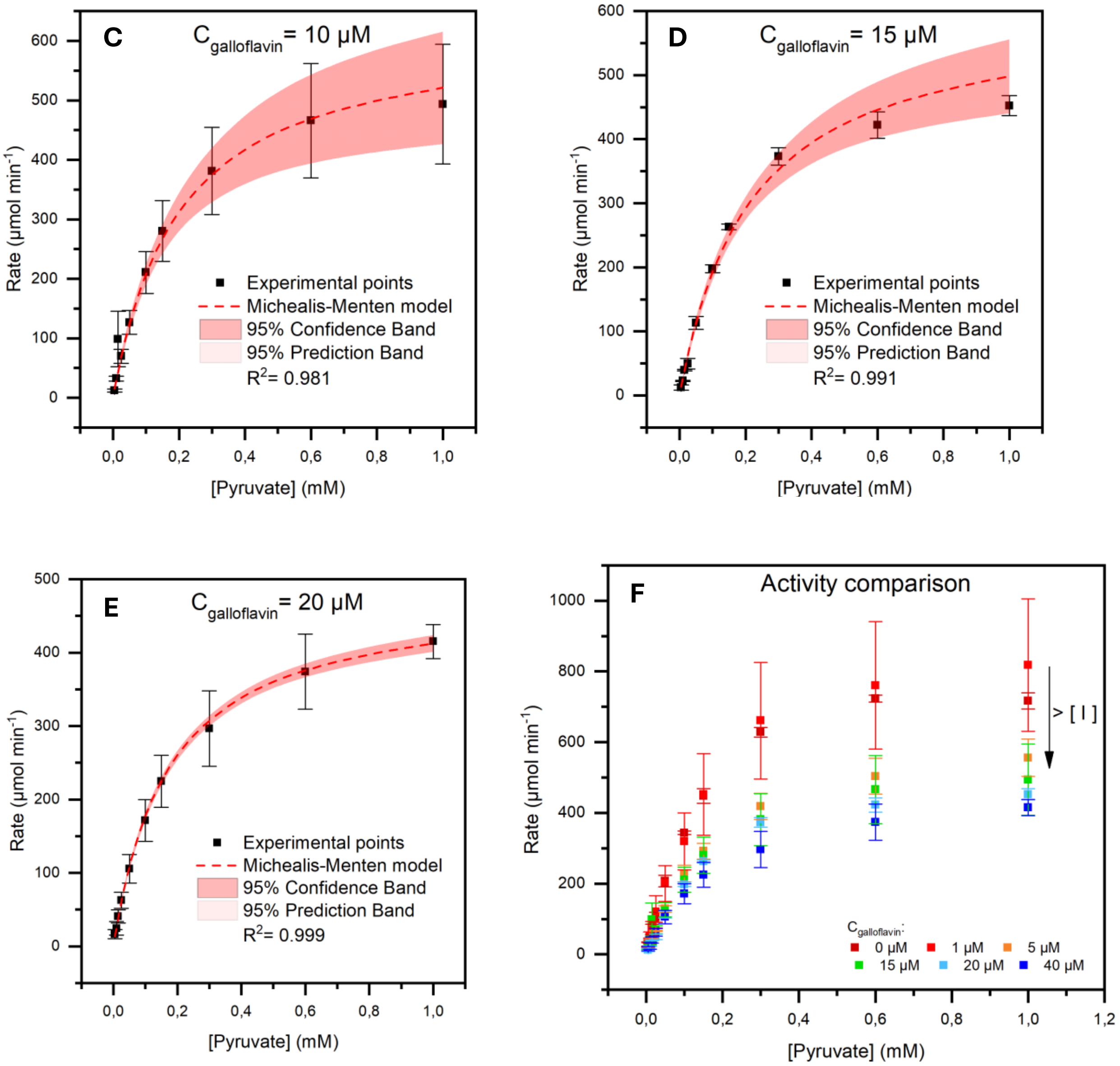

Figure 40. Kinetic results using Galloflavin inhibitor.

The experimental data displayed in Figure 40 were fitted using Michaelis-Menten model, showing a strong agreement between the experimental data and the theoretical fitting. Figure 40F specifically illustrates the effect of increasing inhibitor concentration, where a noticeable decrease in reaction rate confirms the inhibitory action.

Table 14. Summary of the kinetic parameters in presence of Galloflavin inhibitor, obtained with OriginPro.

	PYRUVATE KINETIC PARAMETERS		
$C_{galloflavin}$ [µM]	**V_{max} [µmol min^{-1}]**	**K_m [mM]**	**R^2**
No Galloflavin	861 ± 5	0.147 ± 0.004	0.998
1	969 ± 177	0.176 ± 0.045	0.994
5	707 ± 54	0.231 ± 0.021	0.978
10	626 ± 97	0.202 ± 0.042	0.981
15	606 ± 18	0.215 ± 0.010	0.991
20	484 ± 32	0.172 ± 0.026	0.999

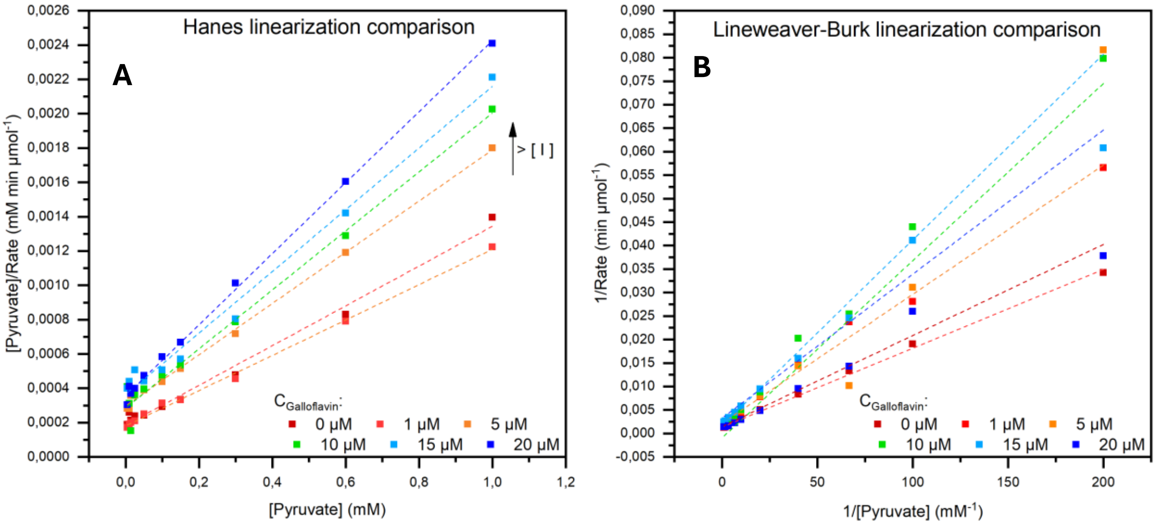

Figure 41. Hanes and Lineweaver-Burk linearizations.

Table 15. Summary of the kinetic parameters in presence of Galloflavin inhibitor, obtained with Hanes-Woolf and Lineweaver-Burk linearizations.

	PYRUVATE KINETIC PARAMETERS					
	Hanes-Woolf			**Lineweaver-Burk**		
$C_{Galloflavin}$ [µM]	**V_{max} [µmol min^{-1}]**	**K_m [mM]**	**R^2**	**V_{max} [µmol min^{-1}]**	**K_m [mM]**	**R^2**
No Galloflavin	864	0.160	0.989	678	0.131	0.973
1	971	0.176	0.997	719	0.121	0.997
5	671	0.200	0.997	461	0.127	0.992
10	581	0.166	0.984	-1090	-0.412	0.937
15	556	0.202	0.989	599	0.237	0.995
20	483	0.172	0.998	306	0.094	0.977

As shown in Table 14, the kinetic parameters determined by OriginPro indicate a reduction in V_{max}, while K_m values appeared not to have a discernible pattern. Table 15, containing parameters derived from Hanes-Woolf linearization of Figure 41A, revealed comparable trends. Furthermore, the parameter values between the two tables generally align well. The only slight deviation occurred at the 10 μM concentration, a difference likely explained by its correspondingly lower R^2 value in the Hanes-Woolf data.

Conversely, the Lineweaver-Burk linearization method proved inadequate for analyzing the experimental data. As depicted in Figure 41B, the lines interpolating the data points at varying inhibitor concentrations intersected irregularly, without exhibiting a discernible pattern. Furthermore, the kinetic parameters derived from the Lineweaver-Burk plot, shown in Table 15, did not concur with those obtained using either OriginPro software or the Hanes-Woolf linearization method. Consequently, the Lineweaver-Burk linearization approach was not considered for subsequent kinetic analyses.

Figure 42 shows the results from kinetic assays using Galloflavin as an inhibitor, with varying cofactor concentrations.

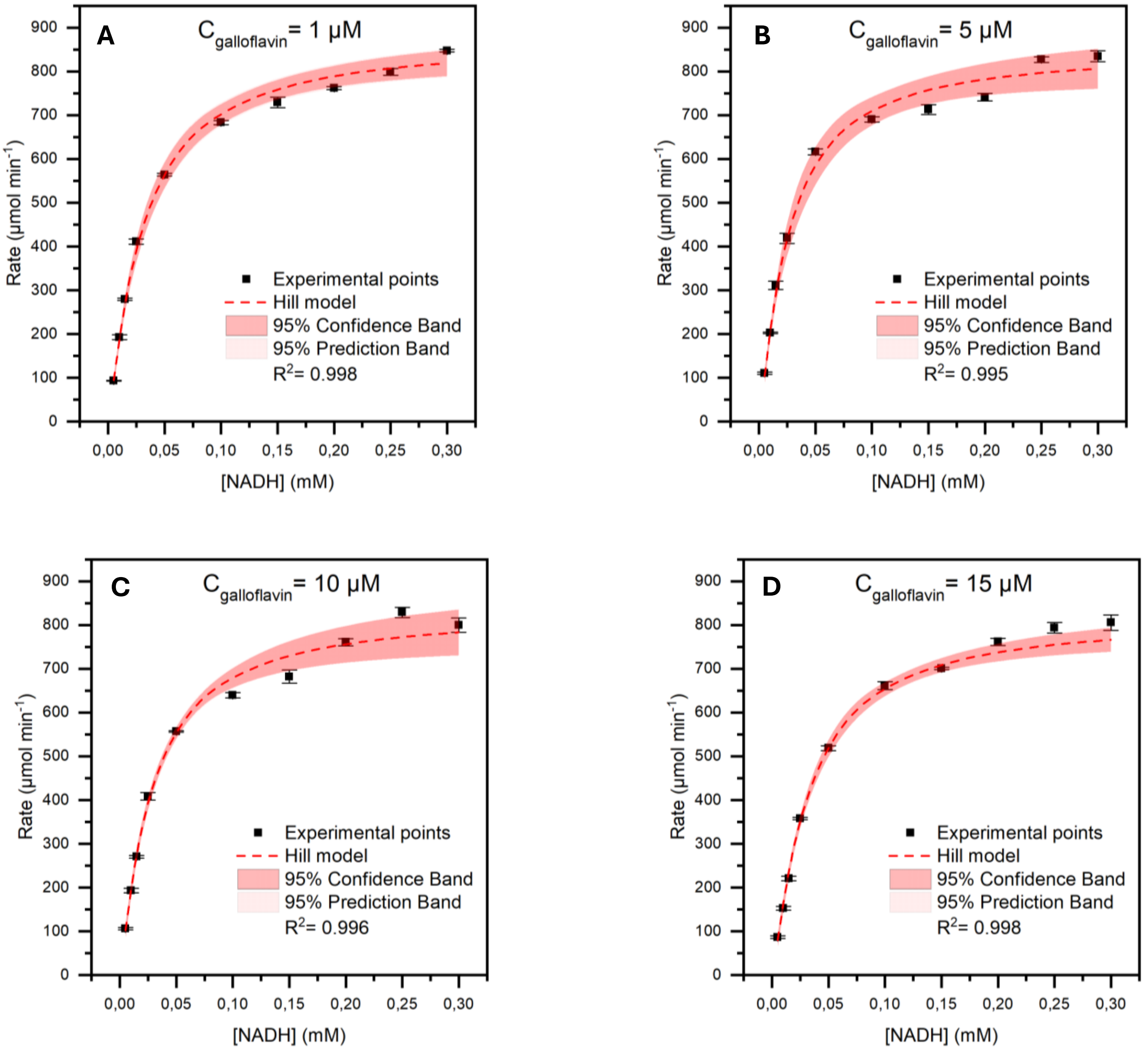

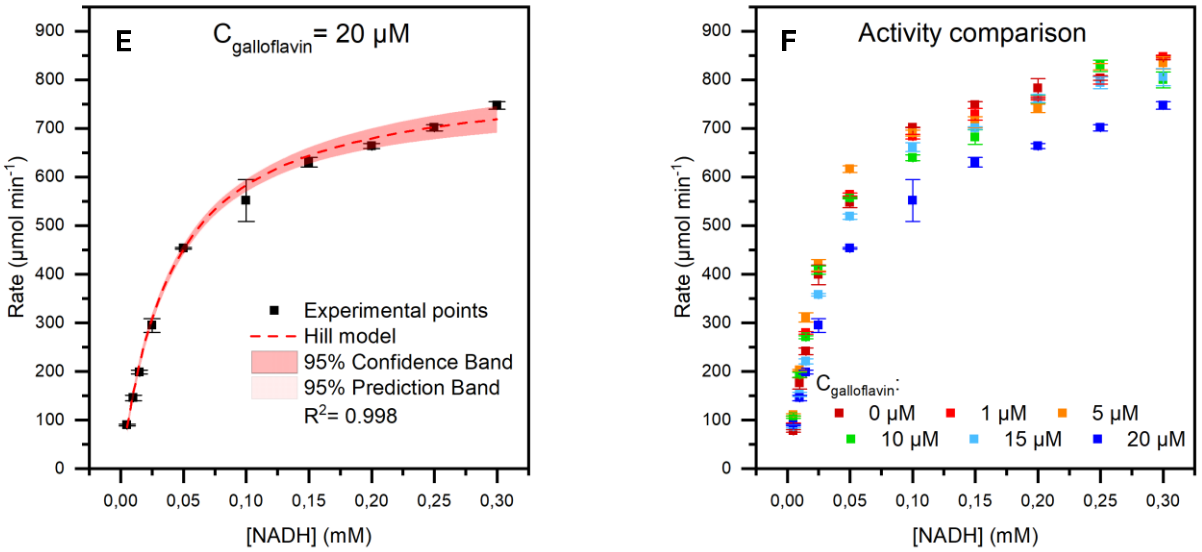

Figure 42. Kinetic results using Galloflavin inhibitor.

Experimental data were fitted using the Hill equation. This fitting also demonstrated strong agreement between the experimental results and the theoretical model. As shown in Figure 42F, increasing the inhibitor concentration led to a clear downward shift of the kinetic curves, indicating an inhibitory effect.

Table 16. Summary of the kinetic parameters in presence of Galloflavin inhibitor.

	NADH KINETIC PARAMETERS			
$C_{galloflavin}$ [μM]	**V_{max} [μmol min^{-1}]**	**K_m [mM]**	**n**	**R^2**
No Galloflavin	891 ± 6	0.034 ± 0.001	1.21 ± 0.02	0.999
1	875 ± 4	0.030 ± 0.001	1.17 ± 0.01	0.998
5	849 ± 8	0.026 ± 0.001	1.20 ± 0.02	0.995
10	834 ± 9	0.028 ± 0.001	1.15 ± 0.02	0.996
15	818 ± 8	0.032 ± 0.001	1.20 ± 0.02	0.998
20	808 ± 8	0.040 ± 0.001	1.03 ± 0.01	0.998

From Table 16, it is evident that V_{max} decreased with increasing inhibitor concentration, consistent with the visual data in Figure 42F. The K_m values exhibited slight fluctuations across increasing Galloflavin concentrations, but no clear or consistent trend emerged. These minor variations suggest that Galloflavin does not substantially alter LDH's affinity for NADH. Furthermore, the cooperativity level, represented by the Hill coefficient (n), remained relatively constant. This suggests that the binding of Galloflavin did not significantly alter the binding affinity of other ligands.

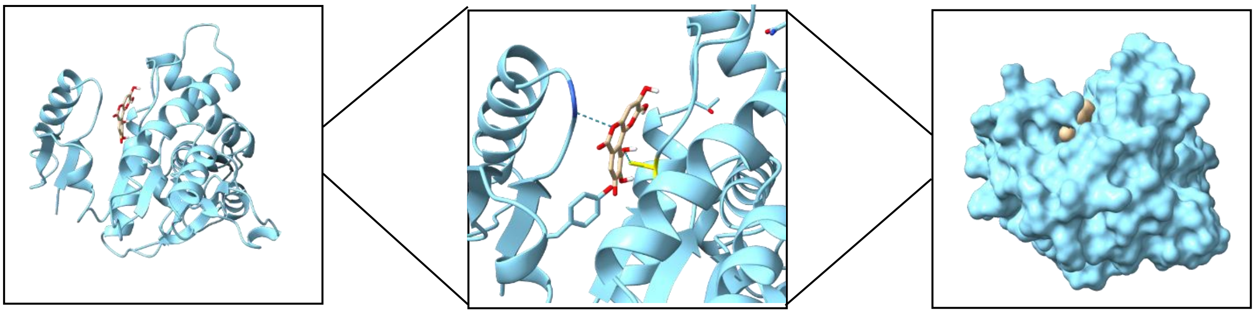

Figure 43. ChimeraX views of the binding between LDH and Galloflavin.

To further support the kinetic findings, docking simulations were conducted using ChimeraX software. As illustrated in Figure 43, Galloflavin appeared to bind to the Isoleucine 8 (blue) and Serine 50 (yellow) residues.

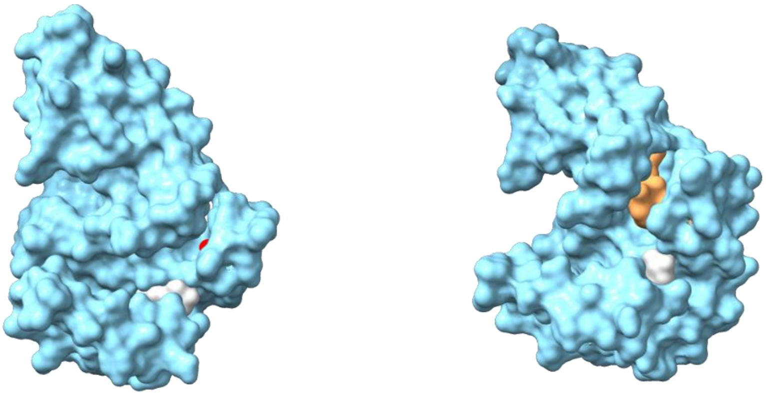

Figure 44. ChimeraX visual representation of LDH's surface with Galloflavin, NADH and pyruvate binding.

Figure 44 provides a surface representation of LDH, pyruvate (red), NADH (yellow), and Galloflavin (white), allowing for visualization of both the active site (where pyruvate and NADH bind) and the Galloflavin binding site. Notably, Galloflavin bound to an allosteric site, as its position is distinct from the substrate and cofactor binding pocket.

The integration of information from both the kinetic tests and docking simulations provided a comprehensive understanding of Galloflavin's inhibition mechanism with respect to both the substrate and the cofactor. Regarding the substrate, Galloflavin's binding site was different from that of the substrate. Furthermore, the V_{max} decreased, while no clear trend was observed for the K_m, although a slight increase was observed compared to the uninhibited condition. These observations suggested a mixed-type inhibition mechanism with a negative net effect [15]. For the cofactor, similar considerations applied, apart from the K_m values, that remained more or less constant. This indicated a non-competitive inhibition mechanism in relation to the cofactor [15].

Table 17. Summary of the identified mechanism of inhibition and the correspond values of Ki.

	Pyruvate	NADH
Inhibition mechanism	Mixed	Non-competitive
Ki [µM] (Analytical)	5 – 18	55 – 195
Ki [µM] (GraphPad Prism)	16	140

Following the identification of the inhibition mechanism, K_i was determined using the two distinct approaches detailed in the 'Materials and Methods' section. Specifically, K_i was calculated analytically and also through non-linear regression using GraphPad Prism. Notably, the values obtained from both methods were in good agreement, with the K_i derived from non-linear regression consistently falling within the range established by the analytical method.

3.2.4.2 FX-11

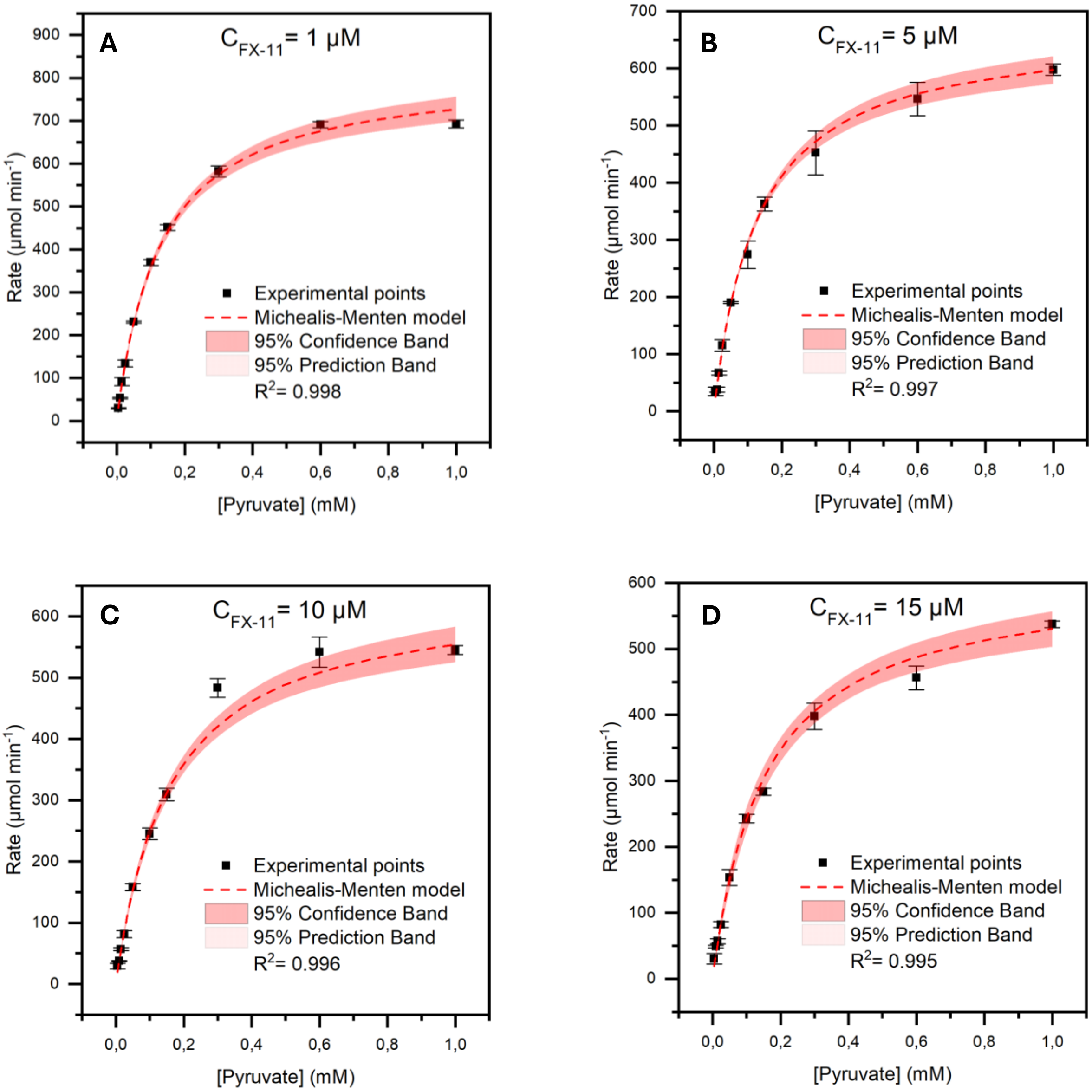

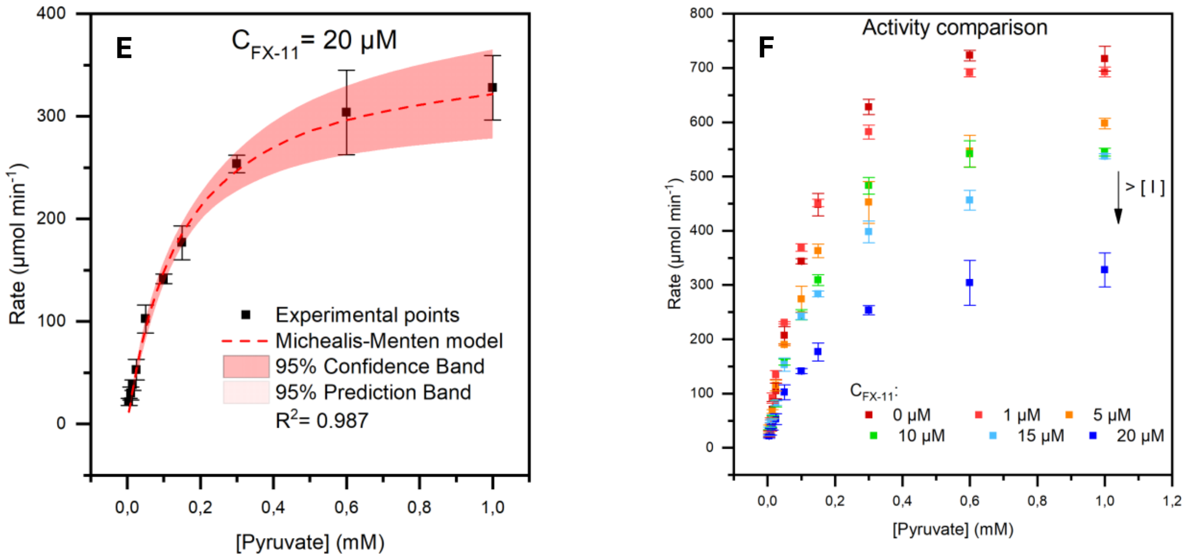

Figure 45. Kinetic results using FX-11 inhibitor.

The second inhibitor tested in this study was FX11.

Figure 45 illustrates the enzyme kinetics of LDH using pyruvate as the variable substrate across a range of FX-11 concentrations from 1 µM to 20 µM. The experimental data were well-fitted using Michaelis-Menten model, with high values of R^2, indicating a good quality of fitting. As Figure 45F reveals, increasing concentration of FX11 resulted in a progressive decrease in enzyme activity, thereby confirming the inhibitory action of FX-11.

Table 18. Summary of the kinetic parameters in presence of FX-11 inhibitor, obtained with OriginPro.

	PYRUVATE KINETIC PARAMETERS		
C_{FX-11} [µM]	**V_{max} [µmol min^{-1}]**	**K_m [mM]**	**R^2**
No FX-11	861 ± 5	0.147 ± 0.004	0.998
1	821 ± 8	0.129 ± 0.003	0.998
5	674 ± 12	0.128 ± 0.004	0.997
10	642 ± 10	0.158 ± 0.004	0.996
15	611 ± 7	0.152 ± 0.005	0.995
20	370 ± 23	0.150 ± 0.018	0.987

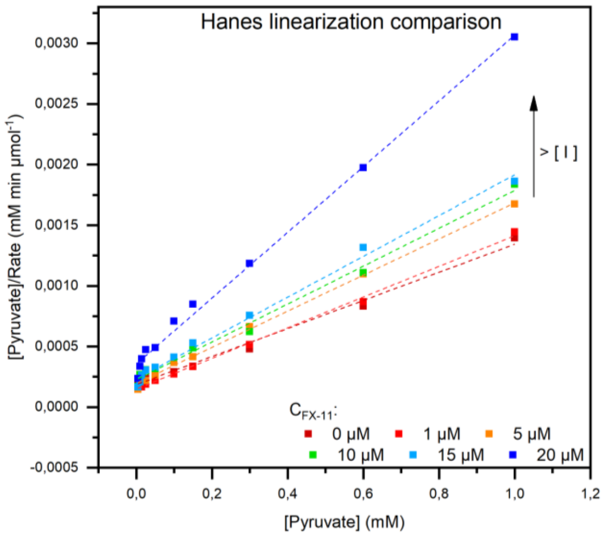

Figure 46. Hanes-Woolf linearization.

Table 19. Summary of the kinetic parameters in presence of FX-11 inhibitor, obtained with Hanes-Woolf linearization.

	PYRUVATE KINETIC PARAMETERS		
	Hanes-Woolf		
C_{FX-11} [µM]	**V_{max} [µmol min^{-1}]**	**K_m [mM]**	**R^2**
No FX-11	864	0.160	0.989
1	792	0.119	0.997
5	672	0.132	0.996
10	640	0.145	0.992
15	594	0.139	0.992
20	369	0.132	0.995

Table18 summarizes the kinetic parameters derived with OriginPro, while Table 19 contains the kinetic parameters derived from the Hanes-Woolf linearization of Figure 46. Notably, a clear concentration-dependent decrease in V_{max} value was observed, while K_m values fluctuated without a consistent trend. This inhibitory effect was evident from both the kinetic parameters obtained through non-linear regression and those derived via Hanes-Woolf linearization, confirming the consistency of the observed trend across different analytical approaches. The obtained results indicated that the effect of FX-11 on LDH kinetics, when pyruvate is the variable substrate, primarily affects the reaction rate.

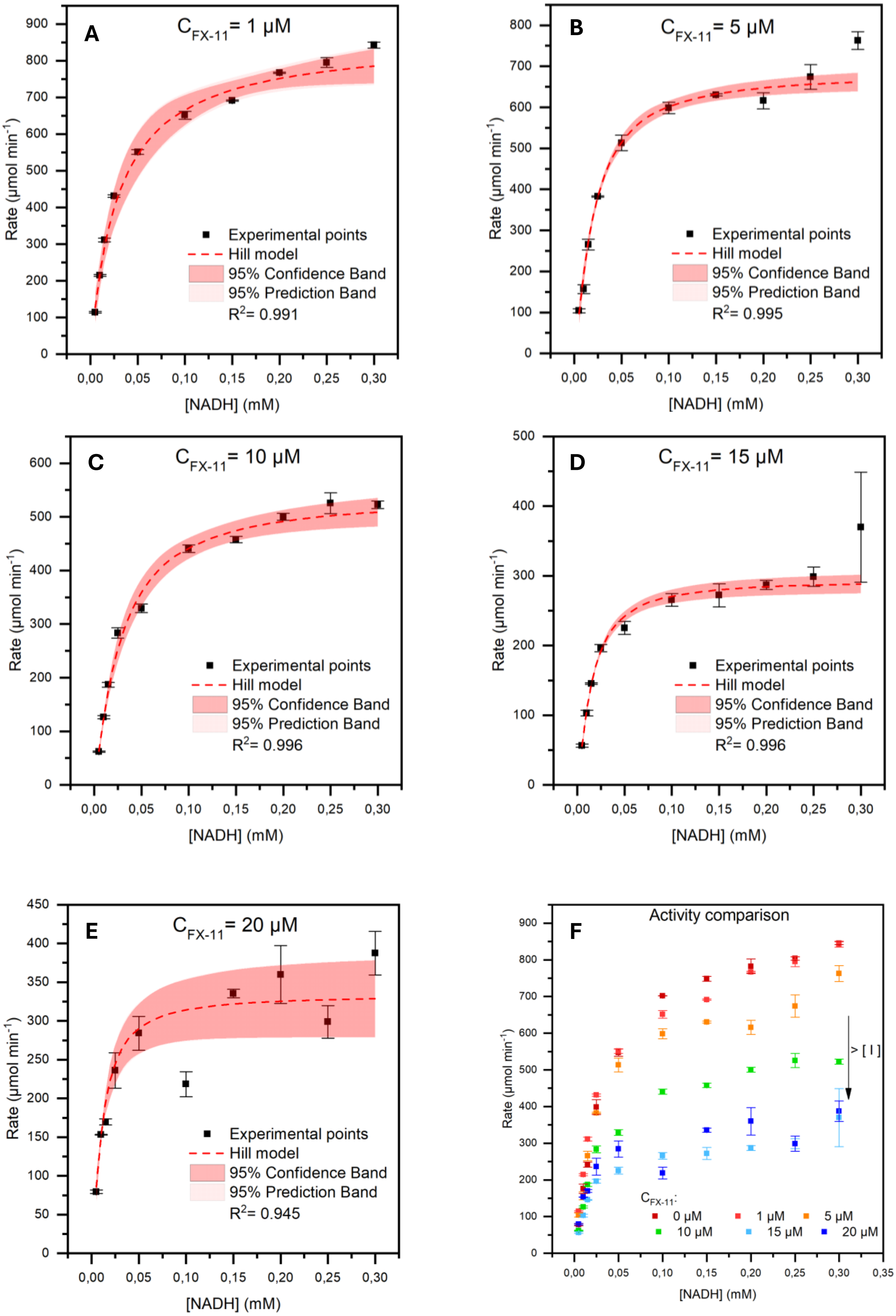

Figure 47. Kinetic results using FX-11 inhibitor.

Figure 47 reports the kinetic behaviour of LDH with NADH as the varying substrate. All experimental data exhibited good fitting to the Hill model.

Notably, in Figure 47D, the point at 0.3 mM shows an elevated error; as other data points did not have comparable errors, this deviation is likely attributable to experimental inaccuracies.

Figure 47F illustrates all the obtained kinetic curves, revealing a consistent decrease in enzyme kinetic activity, expressed ad Vmax, with rising concentrations of FX-11.

Table 20. Summary of the kinetic parameters in presence of FX-11 inhibitor.

	NADH KINETIC PARAMETERS			
$C_{FX\text{-}11}$ [μM]	**V_{max} [μmol min^{-1}]**	**K_m [mM]**	**n**	**R^2**
No FX-11	891 ± 6	0.034 ± 0.001	1.21 ± 0.02	0.999
1	864 ± 7	0.029 ± 0.001	0.98 ± 0.02	0.991
5	685 ± 6	0.021 ± 0.001	1.26 ± 0.04	0.995
10	540 ± 7	0.028 ± 0.001	1.17 ± 0.03	0.996
15	294 ± 6	0.015 ± 0.001	1.29 ± 0.05	0.996
20	334 ± 6	0.011 ± 0.001	1.28 ± 0.05	0.945

Table 20 details kinetic parameters, revealing that FX-11 influenced both V_{max} and K_m, as both values decreased with increasing inhibitor concentration. Conversely, the cooperativity level did not exhibit a discernible trend, indicating that FX-11 does not significantly alter the cooperative nature of NADH binding.

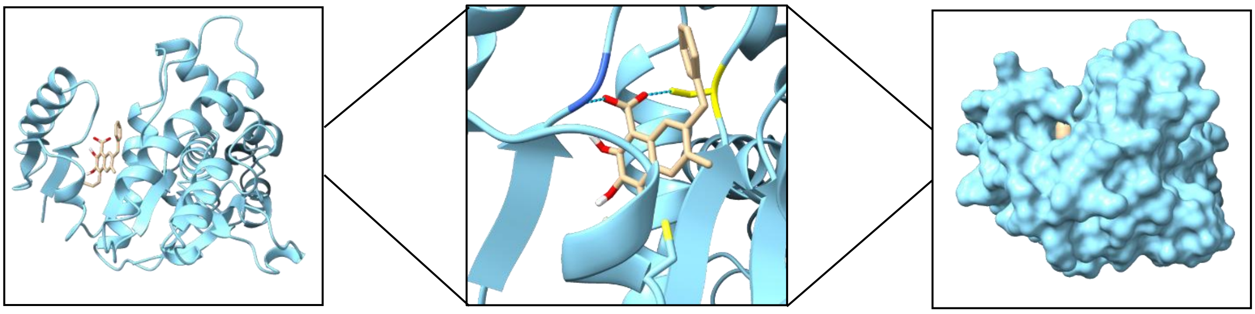

Figure 48. ChimeraX views of the binding between LDH and FX-11.

Figure 48 depicts the simulated binding interaction between LDH and FX-11, showing that FX-11 forms hydrogen bonds with the Isoleucine 6 (blue) and Serine 50 (yellow) residues.

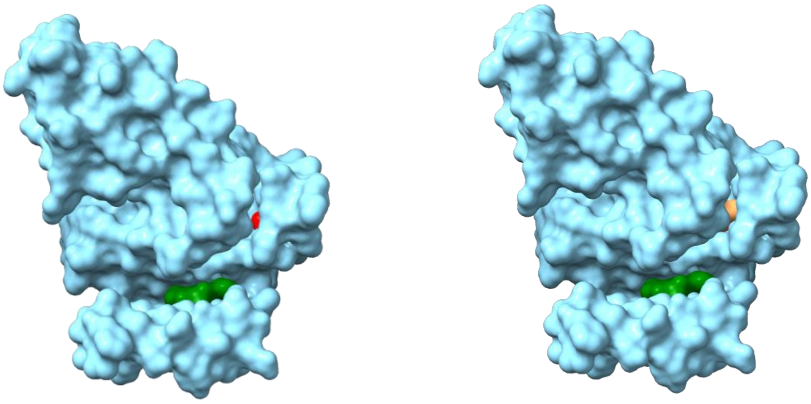

Figure 49. ChimeraX visual representation of LDH's surface with FX-11, NADH and pyruvate binding.

Furthermore, Figure 49 reveals that FX-11(green) interacts with LDH at a site distinct from the active site, namely an allosteric site. This observation unequivocally rules out a competitive inhibition mechanism for both NADH (yellow) and pyruvate (red). In addition to these findings, the kinetic parameters in Table 18 show a decrease in V_{max}, but no defined trend for K_m, when the kinetic curve is function of pyruvate, indicating a mixed-type inhibition mechanism [15]. Similarly, when NADH serves as the substrate, an increase in inhibitor concentration leads to a decrease in both V_{max} and K_m, also characteristic of a mixed-type inhibition [15]. Although a decrease in the apparent K_m suggests an enhanced affinity of the enzyme for its substrate, this effect is counteracted by a concurrent reduction in the apparent V_{max}, which indicates a lower catalytic rate. Consequently, the overall net effect appears to be inhibitory, particularly at high substrate concentrations where the influence on Vmax becomes the dominant factor.

Table 21. Summary of the identified mechanism of inhibition and the correspond values of Ki.

	Pyruvate	NADH
Inhibition mechanism	Non-competitive	Mixed
Ki [μM] (Analytical)	15 – 37	0 – 44
Ki [μM] (GraphPad Prism)	18	31

Table 21 presents the kinetic parameters determined using both the analytical method and non-linear regression. In this instance, the values obtained from the two approaches also demonstrated consistency, as the parameter derived from non-linear regression consistently fell within the range established by the analytical method.

3.2.4.3 Gossypol

The kinetic evaluation proceeded testing Gossypol as inhibitor.

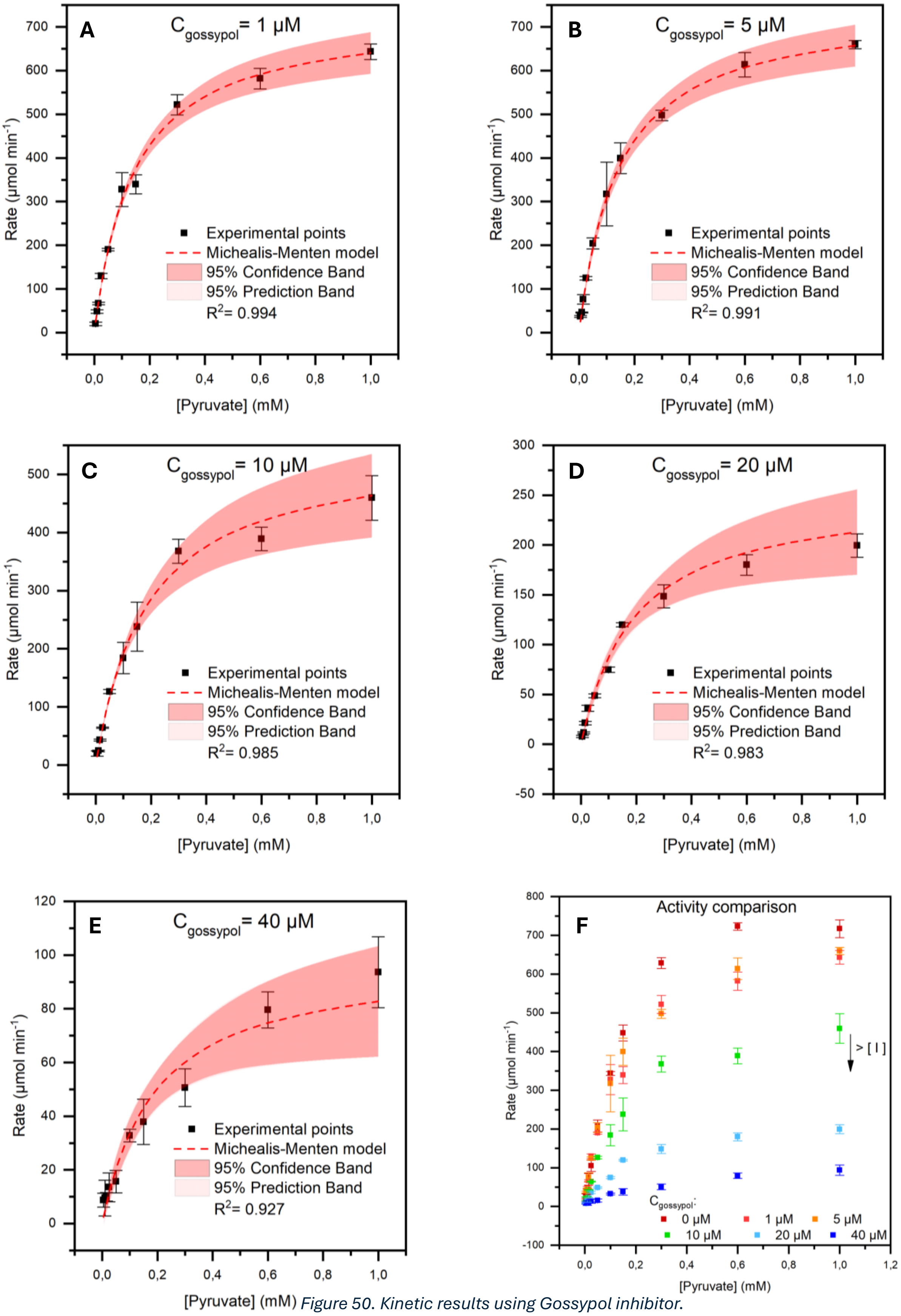

Figure 50. Kinetic results using Gossypol inhibitor.

Figure 50 displays the LDH kinetic results with pyruvate as the variable substrate and Gossypol as the inhibitor, with concentrations ranging between 1 µM and 40 µM.

All data set were fitted with Michaelis-Menten model, with overall good fitting observed at low inhibitor concentrations. However, the goodness of fit diminished at higher Gossypol concentrations, likely due to absorbance interference caused by Gossypol itself, which exhibits a non-null absorption at 340 nm, as shown in Figure 24B, which may have influenced the accuracy of the experimental measurements.

Figure 50F further illustrates a progressive decrease in the enzyme's reaction rate with increasing Gossypol concentration.

Table 22. Summary of the kinetic parameters in presence of Gossypol inhibitor, obtained with OriginPro.

	PYRUVATE KINETIC PARAMETERS		
$C_{Gossypol}$ [µM]	**V_{max} [µmol min^{-1}]**	**K_m [mM]**	**R^2**
No Gossypol	861 ± 5	0.147 ± 0.004	0.998
1	731 ± 19	0.142 ± 0.006	0.994
5	752 ± 11	0.143 ± 0.004	0.991
10	550 ± 26	0.186 ± 0.01	0.985
20	254 ± 11	0.192 ± 0.01	0.983
40	99 ± 11	0.194 ± 0.038	0.927

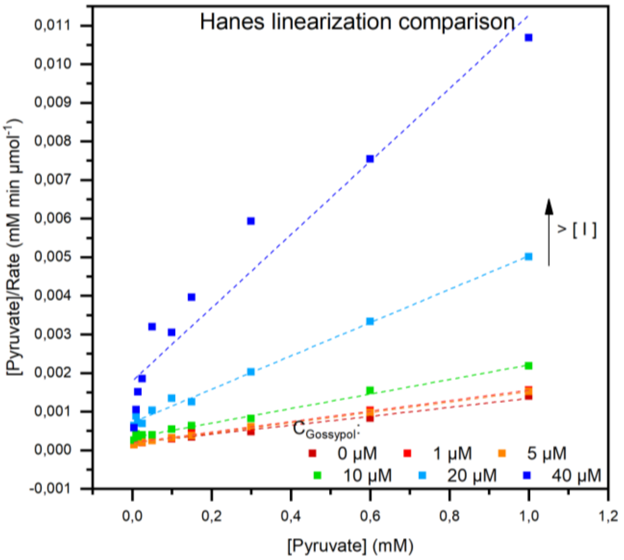

Figure 51. Hanes-Woolf linearization.

Table 23. Summary of the kinetic parameters in presence of Gossypol inhibitor, obtained with Hanes-Woolf linearization.

	PYRUVATE KINETIC PARAMETERS		
	Hanes-Woolf		
$C_{Gossypol}$ [μM]	**V_{max} [μmol min^{-1}]**	**K_m [mM]**	**R^2**
No Gossypol	864	0.160	0.989
1	735	0.146	0.995
5	743	0.130	0.998
10	530	0.173	0.991
20	232	0.166	0.993
40	106	0.190	0.928

Table 22 and 23 summarizes the kinetic parameters for this set of curves, obtained using non-linear regression in OriginPro or via Hanes-Woolf linearization of Figure 51, respectively. Both sets of results consistently show a decrease in V_{max} values. Conversely, K_m values remained relatively stable at lower concentration and showed a moderate increase only at higher concentration of inhibitor (≥ 10 μM). This pattern could suggest that Gossypol did not drastically alter the affinity of LDH for pyruvate at low concentration but may begin to interfere with substrate binding or cause conformational changes at higher concentrations, resulting in decreased affinity of LDH towards its substrate. However, the consistency between the kinetic parameters of the two tables once again demonstrates reliability of the calculated K_m and V_{max}.

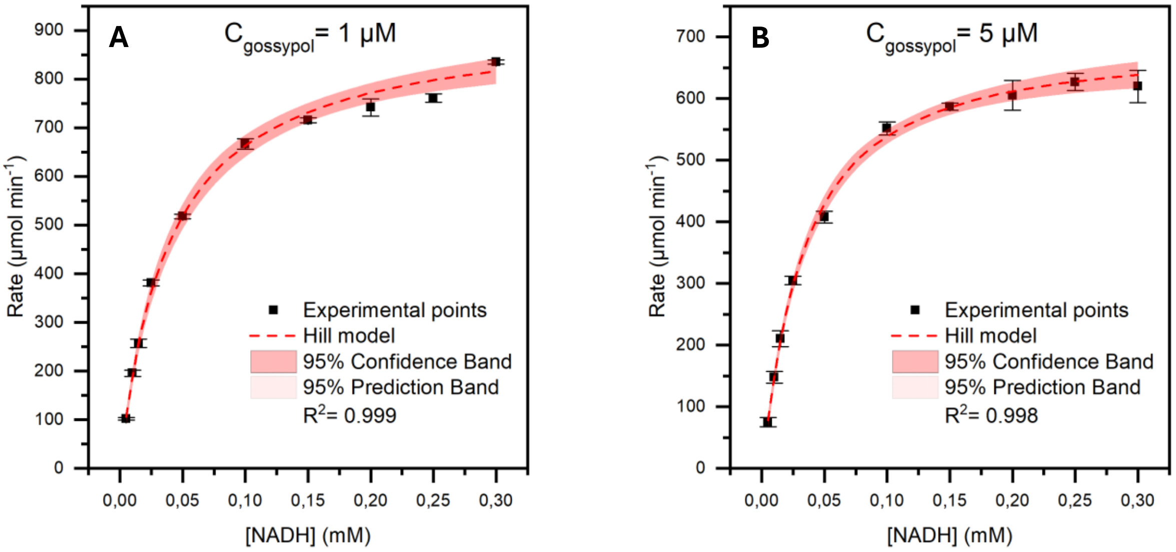

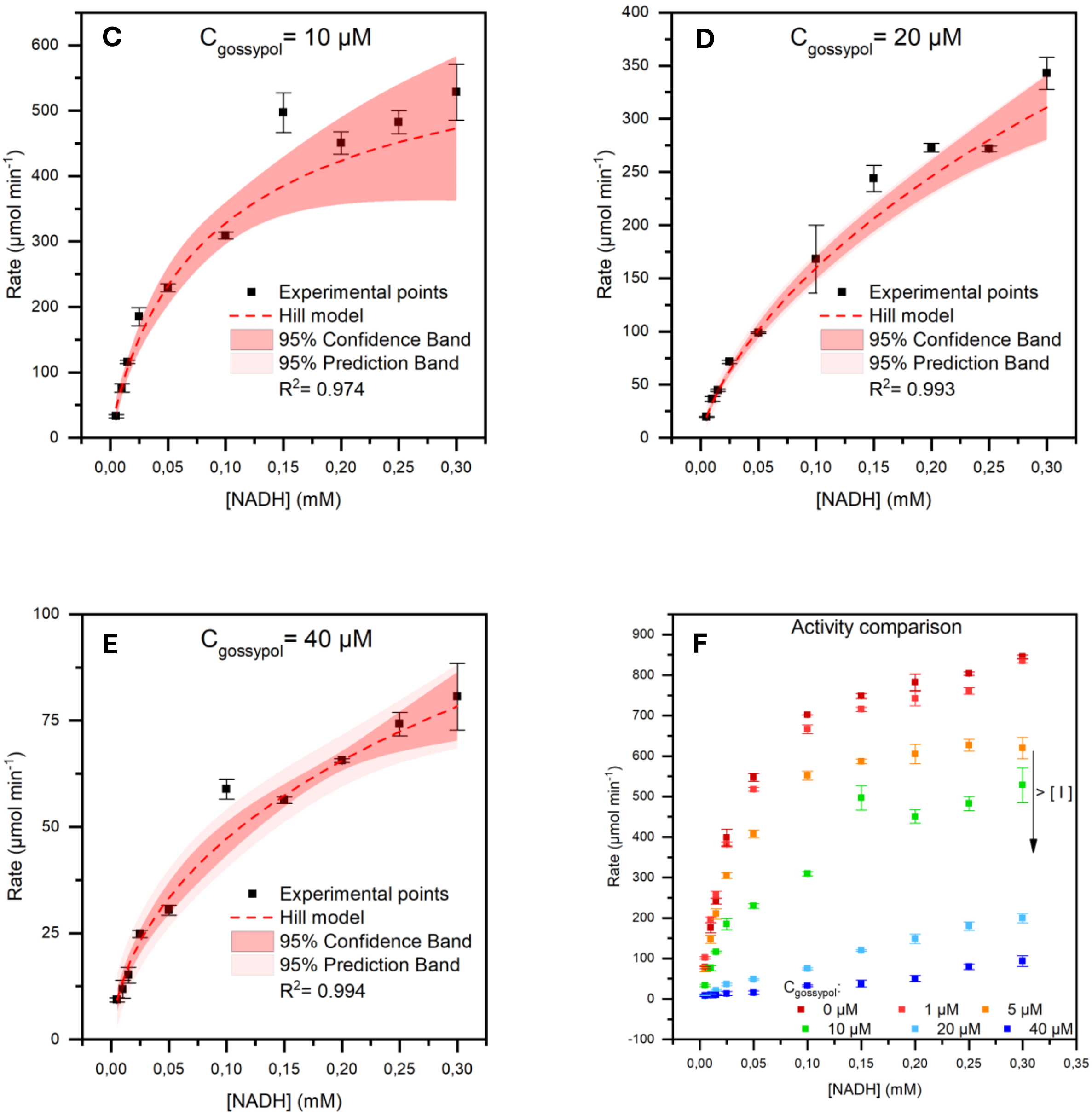

Figure 52. Kinetic results using Gossypol inhibitor.

Figure 52 displays the LDH kinetic curves, with NADH as the variable substrate, fitted to the Hill model. All curves displayed a good fit.

Figure 52F further illustrates a diminished LDH activity at higher inhibitor concentrations compared to the uninhibited activity.

Table 24. Summary of the kinetic parameters in presence of Gossypol inhibitor.

	NADH KINETIC PARAMETERS			
$C_{Gossypol}$ [μM]	**V_{max} [μmol min^{-1}]**	**K_m [mM]**	**n**	**R^2**
No Gossypol	891 ± 6	0.034 ± 0.001	1.21 ± 0.02	0.999
1	925 ± 10	0.039 ± 0.001	0.99 ± 0.02	0.999
5	693 ± 18	0.032 ± 0.002	1.21 ± 0.05	0.991
10	655 ± 59	0.100 ± 0.021	0.86 ± 0.04	0.974
20	1346 ± 213	1.558 ± 0.460	0.73 ± 0.01	0.993
40	282 ± 129	1.517 ± 1.745	0.59 ± 0.04	0.994

Table 24 summarizes the kinetic parameters derived from the preceding curves. No precise trend was observed for V_{max} and n values. Despite this, the observed n values tended to be lower, suggesting that the inhibitor reduces the cooperativity between NADH and the enzyme. Conversely, K_m values appeared to increase, even if the elevated errors at higher concentrations preclude a definitive confirmation of this trend. Nonetheless, the increase in K_m suggests a weakening of NADH binding, possibly due to interference from Gossypol.

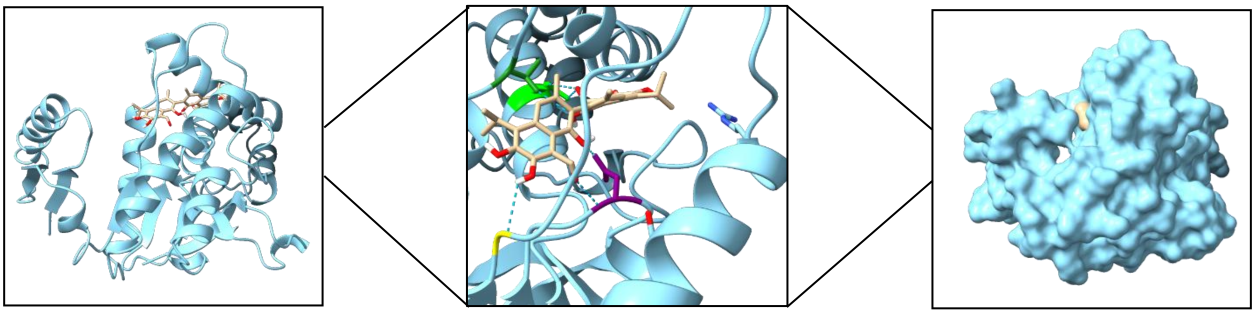

Figure 53. ChimeraX views of the binding between LDH and Gossypol.

As depicted in Figure 46, Gossypol formed numerous interactions with LDH, specifically showing two hydrogen bonds with Arginine 124 (light green), one with Serine 50 (yellow), one with Threonine 203 (green), and two with Asparagine 93 (violet) residues.

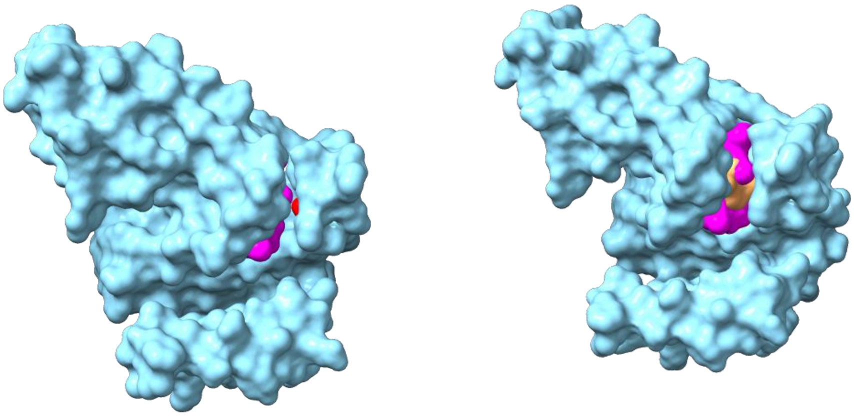

Figure 54. ChimeraX visual representation of LDH's surface with Gossypol, NADH and pyruvate binding.

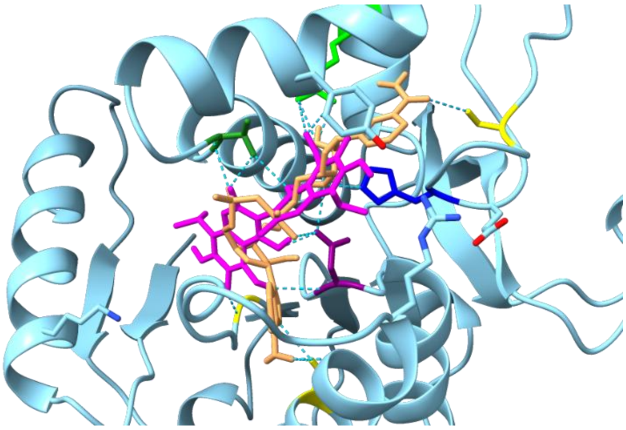

Figure 55. Enlarged view of the binding of NADH and Gossypol with LDH; obtained with ChimeraX

Figure 55 demonstrates that Gossypol (pink) did not interfere with pyruvate (red) binding to LDH, but it did interfere with NADH (yellow) binding. Indeed, the enlarged view presented in Figure 53 provides a clearer visualization of the common residues involved in the binding of both NADH and Gossypol. Both molecules were observed to interact with Asparagine 93, Arginine 124, and Threonine 203 residues.

The absence of competitive inhibition with pyruvate is supported by the kinetic parameters in Table 12, where a decrease in V_{max} and an increase in K_m suggest a mixed-type inhibition mechanism with a negative net effect [15].

Different considerations apply to the interaction between Gossypol and NADH. While simulations suggest competitive inhibition, the kinetic parameters indicate a mixed-type inhibition, as K_m increases, but V_{max} does not remain constant [15]. This discrepancy might be attributed to the NADH concentration range used, which may have been too narrow or with a maximum value too low to fully capture the saturating behaviour of the enzyme. If the tested concentrations were too low to reach enzyme saturation, the full competitive behaviour of Gossypol may not have been observed. As a result, the inhibition may appear mixed type rather than purely competitive, as in the case here reported. In fact, kinetic curve appears not to have reached saturation, suggesting a potential competitive behaviour at higher NADH concentrations. To confirm whether Gossypol is truly a competitive inhibitor with NADH, it would be necessary to repeat the experiments using higher NADH concentrations, that allows the enzyme to approach the saturation.

Table 25. Summary of the identified mechanism of inhibition and the correspond values of Ki.

	Pyruvate	NADH
Inhibition mechanism	Mixed	Mixed/Competitive
Ki [μM] (Analytical)	4 – 44	0.14 – 10 / 0.45 – 7
Ki [μM] (GraphPad Prism)	10	4.92 / 1.36

Table 25 summarizes the inhibition constants associated with the identified inhibition mechanisms. For each mechanism, the first K_i value represents a range determined analytically, while the second is a precise value obtained through non-linear regression.

Regarding NADH, two values are presented for each calculation method. This is because K_i was calculated under two different inhibition models: mixed inhibition, as indicated by the kinetic curve analysis, and competitive inhibition, as suggested by the docking simulations. Notably, the K_i values derived from both analytical and non-linear regression methods demonstrate coherence across these different methods employed.

3.2.4.4 NHI-2

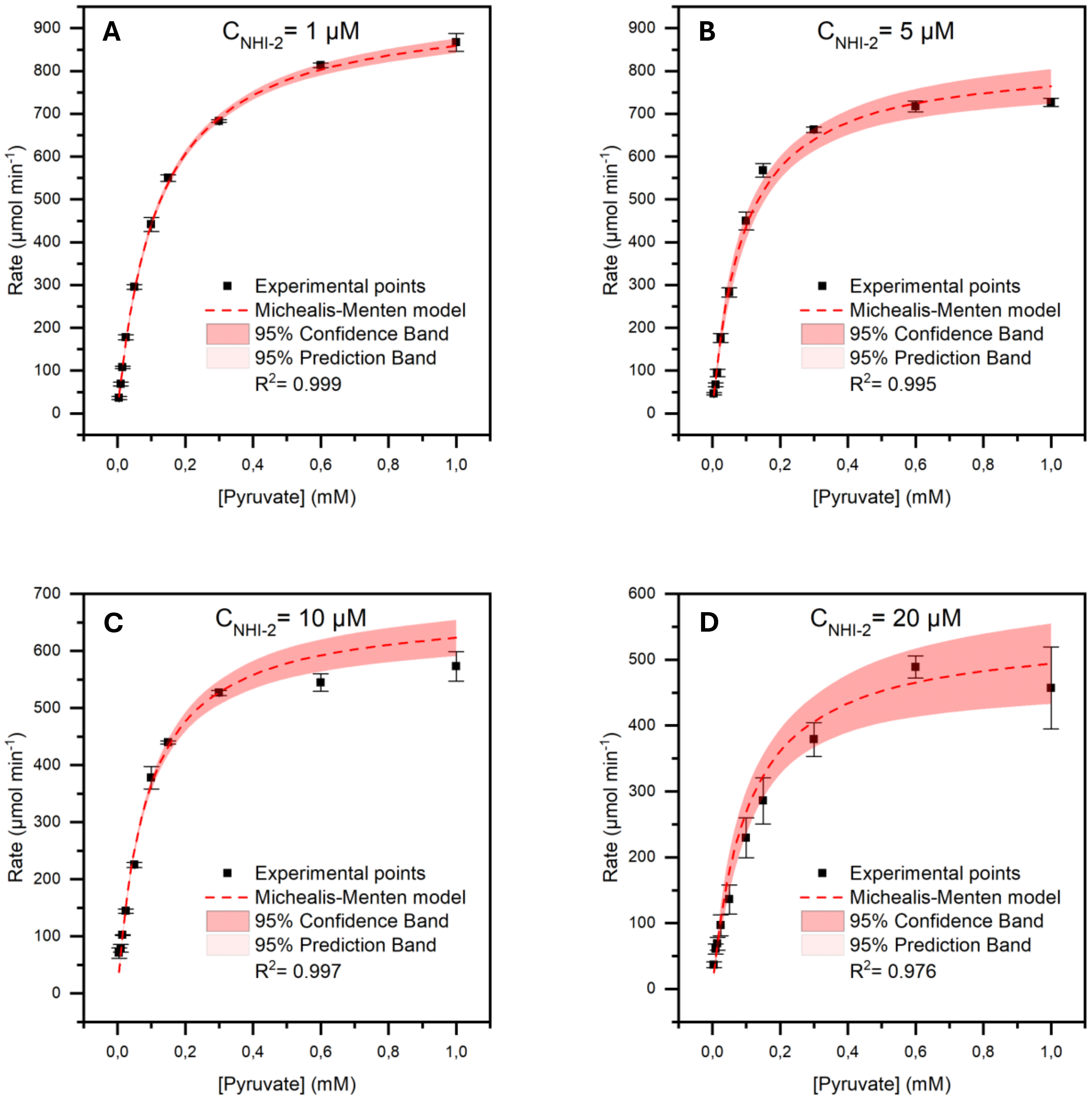

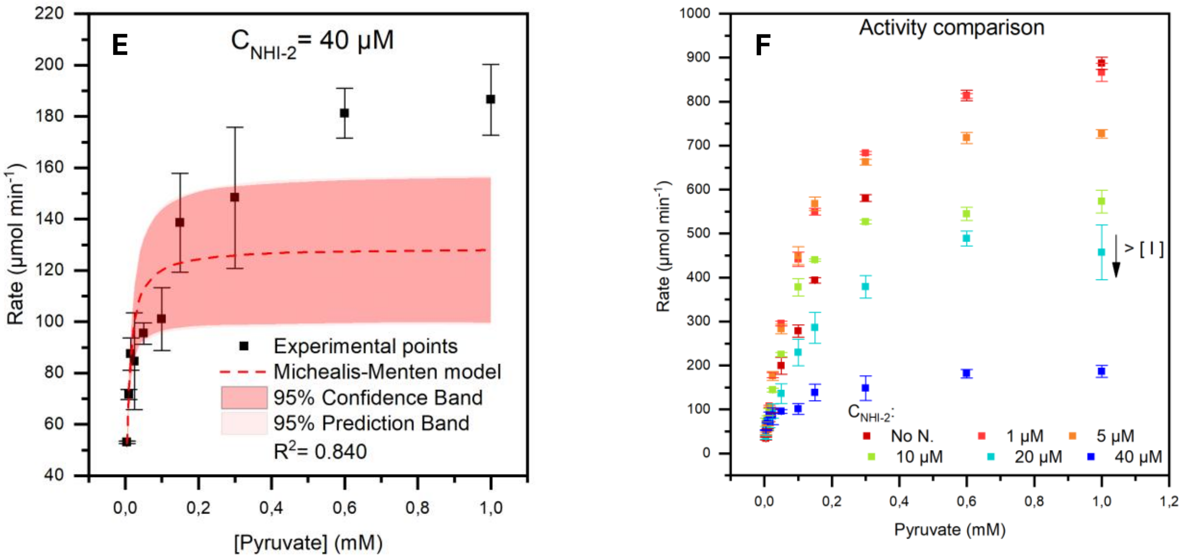

Figure 56. Kinetic results using NHI-2 inhibitor.

Figure 56 displays the experimental LDH kinetic curves, with pyruvate as the variable substrate, in the presence of another tested inhibitor, namely NHI-2, with concentrations ranging between 1 µM and 40 µM.

The data were fitted using Michaelis-Menten model. It is immediately evident that the goodness of fit at an inhibitor concentration of 40 µM was poorer compared to lower concentrations. This behaviour could be attributed to the contribution of NHI-2's absorbance peak at 340 nm, as previously highlighted in Figure 24B. Such spectral interference likely compromised the accuracy of the measurements, especially at high inhibitor concentration, preventing the data points from perfectly fitting the model.

As seen in Figure 56F, LDH activity progressively decreased as the NHI-2 concentration increased.

Table 26. Summary of the kinetic parameters in presence of NHI-2 inhibitor, obtained with OriginPro.

	PYRUVATE KINETIC PARAMETERS		
C_{NHI-2} [µM]	**V_{max} [µmol min^{-1}]**	**K_m [mM]**	**R^2**
No NHI-2	861 ± 5	0.147 ± 0.004	0.998
1	960 ± 7	0.117 ± 0.003	0.999
5	834 ± 9	0.091 ± 0.003	0.995
10	676 ± 5	0.084 ± 0.001	0.997
20	545 ± 22	0.103 ± 0.011	0.976
40	129 ± 4	0.007 ± 0.001	0.840

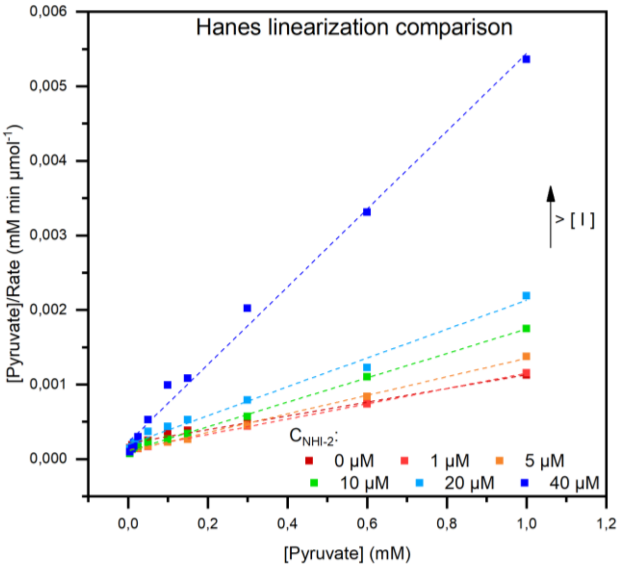

Figure 57. Hanes-Woolf linearization.

Table 27. Summary of the kinetic parameters in presence of NHI-2 inhibitor, obtained with Hanes-Woolf linearization.

	PYRUVATE KINETIC PARAMETERS		
	Hanes-Woolf		
C_{NHI-2} [μM]	**V_{max} [μmol min^{-1}]**	**K_m [mM]**	**R^2**
No NHI-2	864	0.160	0.989
1	974	0.122	0.999
5	804	0.087	0.997
10	611	0.065	0.998
20	517	0.101	0.990
40	192	0.043	0.993

Table 26 and Table 27 report kinetic parameters obtained with OriginPro software, and with Hanes-Woolf linearization shown in Figure 57, respectively. Both approaches indicate a decrease in V_{max} values. Although K_m values do not exhibit a precise trend with increasing NHI-2 concentrations, they were generally lower than the value observed in the absence of the inhibitor. This suggests that NHI-2 may enhance substrate binding affinity, under certain condition.

However, due to the variability at higher concentrations and potential measurements interferences these results should be interpreted with caution. In fact, focusing on the K_m value at 40 μM in Table 22, it appeared less reliable, not only due to its lower R^2 value but also because it did not align with the value estimated using the Hanes method.

As previously mentioned, obtaining reliable results at such high concentrations of NHI-2 was challenging due to its peak absorbance at 340 nm.

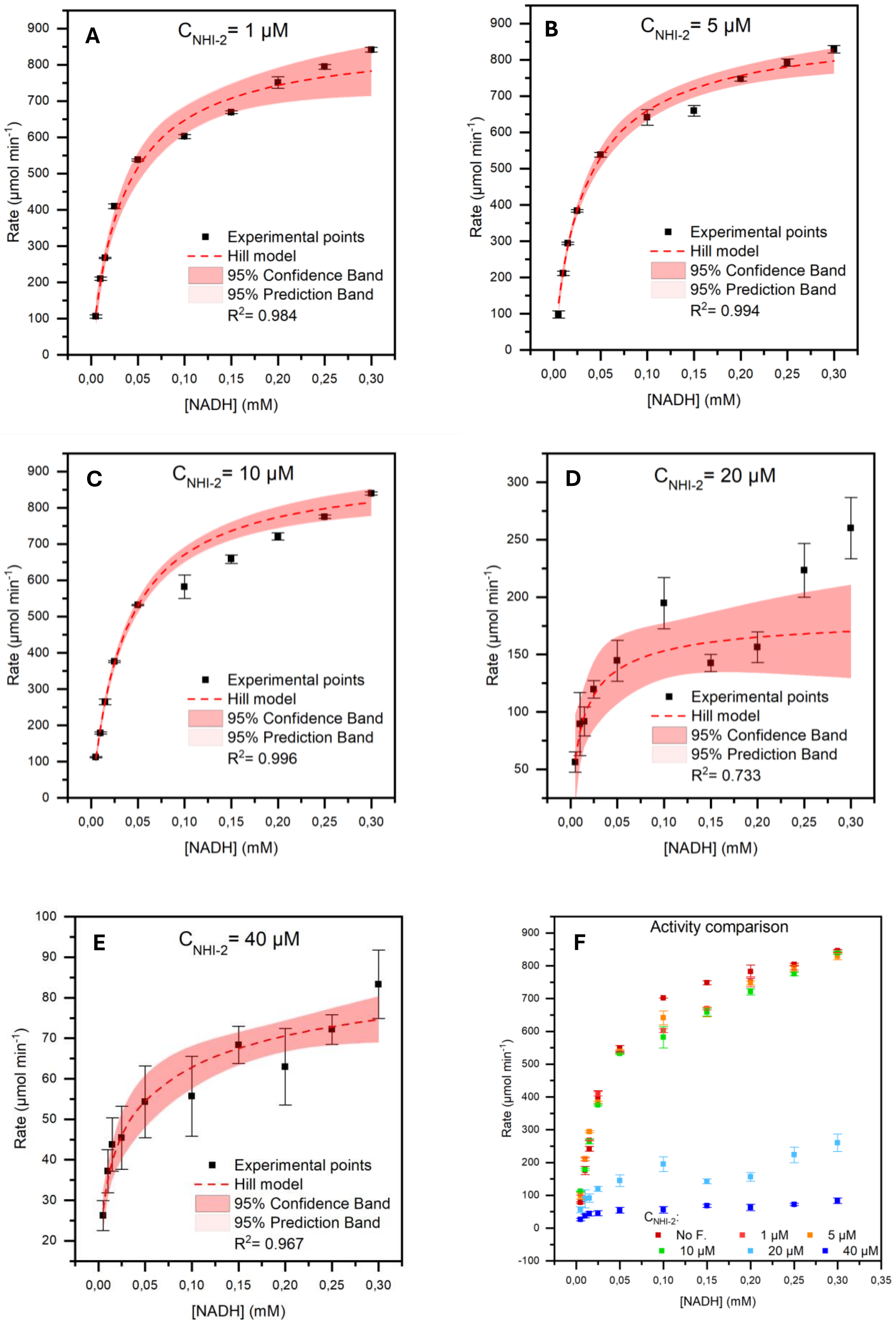

Figure 58. Kinetic results using NHI-2 inhibitor.

Figure 58 displays the LDH kinetic curves in the presence of NHI-2, with NADH as the variable substrate. All experimental points were fitted to Hill model. While most fits were satisfactory, it is evident that the results at 20 μM of NHI-2 show a suboptimal goodness of fit, in contrast to the better fit at 40 μM. This suggested that 20 μM may represent a transitional concentration at which the inhibitory effect of NHI-2 is only partially exerted, possibly resulting in heterogeneous kinetic behaviour.

Figure 58F further illustrates the decreasing trend of all curves across increasing inhibitor concentrations.

Table 28. Summary of the kinetic parameters in presence of NHI-2 inhibitor.

	NADH KINETIC PARAMETERS			
C_{NHI-2} [μM]	**V_{max} [μmol min^{-1}]**	**K_m [mM]**	**n**	**R^2**
No NHI-2	891 ± 6	0.034 ± 0.001	1.21 ± 0.02	0.999
1	881 ± 10	0.035 ± 0.001	0.96 ± 0.02	0.984
5	904 ± 17	0.034 ± 0.002	0.93 ± 0.03	0.994
10	912 ± 6	0.036 ± 0.001	1.01 ± 0.01	0.996
20	185 ± 22	0.013 ± 0.005	0.77 ± 0.23	0.733
40	102 ± 47	0.038 ± 0.001	0.48 ± 0.26	0.967

Table 28 provides the kinetic parameters of the LDH kinetic curves as a function of NADH concentration. The V_{max} values decreased sharply after exceeding a concentration of 10 μM. K_m remained generally constant, except for the drop observed at 20 μM, which again could be influenced by poor quality fit.

Finally, the cooperativity level did not exhibit a distinctive trend across the tested NHI-2 concentrations. However, a general decrease in cooperativity can be observed when compared the single value to the uninhibited condition. In the absence of NHI-2, in fact, the enzyme displays mild positive cooperativity, whereas most inhibited conditions show lower n values, falling below 1. This suggests that NHI-2 may reduce the positive cooperative interaction between LDH subunits, possibly altering the enzyme's allosteric regulation, even though in a not strict dose-dependent manner.

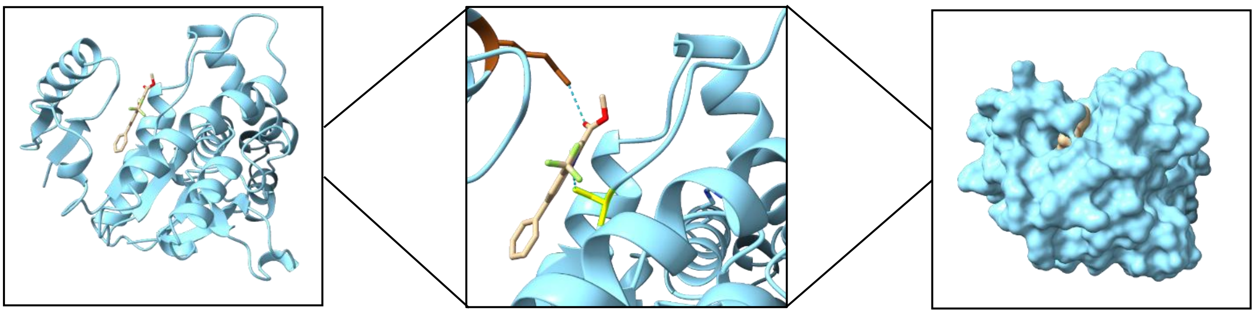

Figure 59. ChimeraX views of the binding between LDH and NHI-2.

Figure 59 displays the interactions between LDH and NHI-2. The inhibitor forms hydrogen bonds with the Lysine 12 (brown) and the Serine 50 (yellow) residues of the enzyme.

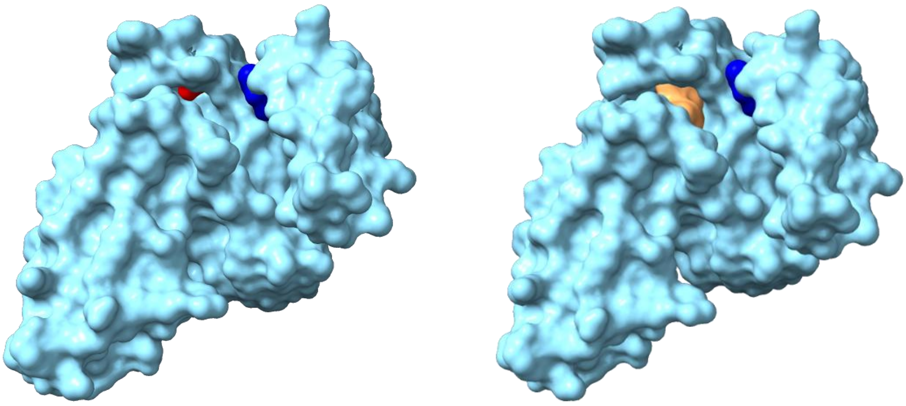

Figure 60. ChimeraX visual representation of LDH's surface with NHI-2, NADH and pyruvate binding.

Figure 60 demonstrates that NHI-2 (blue) binds to an allosteric site on LDH, distinct from the active site. Consequently, the inhibition mechanism cannot be competitive, regardless of whether the substrate or cofactor concentration is varied.

Reviewing the pyruvate parameters in Table 26 and 27, the observed decrease in V_{max} coupled with an undefined trend for K_m but lower values compared to the uninhibited one, indicates a mixed-type inhibition mechanism [15]. It is important to emphasize that, despite an apparent decrease in K_m, suggesting enhanced enzyme-substrate affinity, the overall effect remains inhibitory. This is due to a substantial decrease in V_{max}, which effectively compensates for the improved binding, resulting in a net inhibitory impact on the reaction. This kind of inhibition is confirmed by the binding of NHI-2 to an allosteric site.

For the cofactor, the results in Table 28 point to non-competitive inhibition, as V_{max} diminishes while K_m remains constant, excluding the value at 20 μM [15].

However, the final interpretations of the NADH kinetic curves are not entirely reliable. As illustrated in Figure 25, the high absorbance peak of NHI-2 significantly overlaps with NADH signal at low concentrations, making it challenging to accurately discern the NADH signal from the NHI-2 signal and limiting the reliability of the spectrophotometric method in accurately evaluating LDH kinetics. Therefore, while current data suggest an allosteric mechanism for pyruvate and non-competitive inhibition with respect to NADH, spectrophotometric analysis may not be the optimal method for elucidating the precise interaction between NHI-2 and LDH. Further structural studies, such as X-ray crystallography, might be necessary to conclusively determine the interaction mode.

Table 29. Summary of the identified mechanism of inhibition and the correspond values of Ki.

	Pyruvate	NADH
Inhibition mechanism	Mixed	Non-competitive
Ki [μM] (Analytical)	0 – 187	0 – 88
Ki [μM] (GraphPad Prism)	148	15

Table 29 summarizes the inhibition constant values, which were calculated using both non-linear regression and an analytical approach following the identification of the inhibition mechanism. A clear coherence is observable between the K_i values determined with GraphPad Prism and those derived from the analytical range.

3.2.4.5 Oxamate

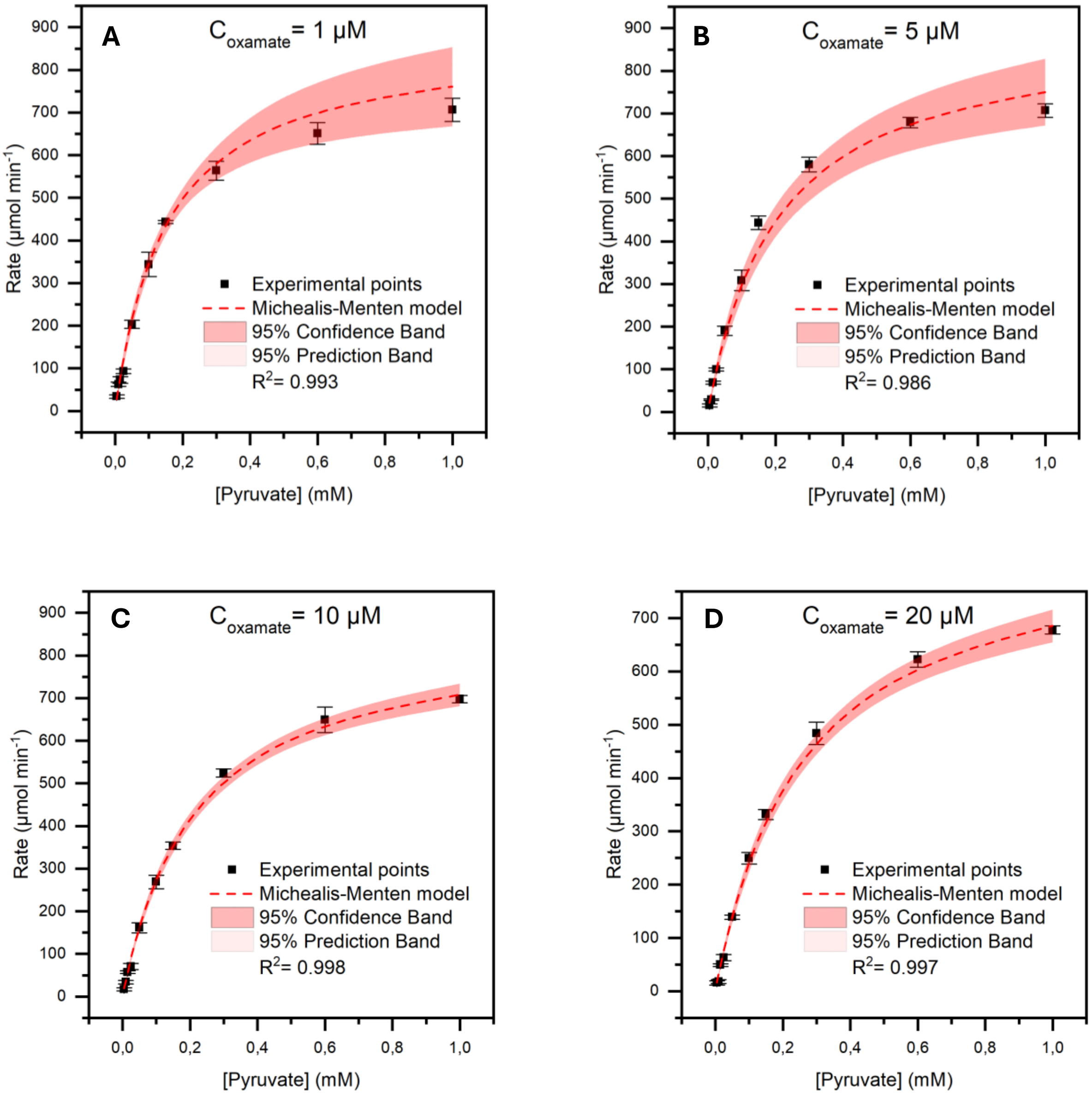

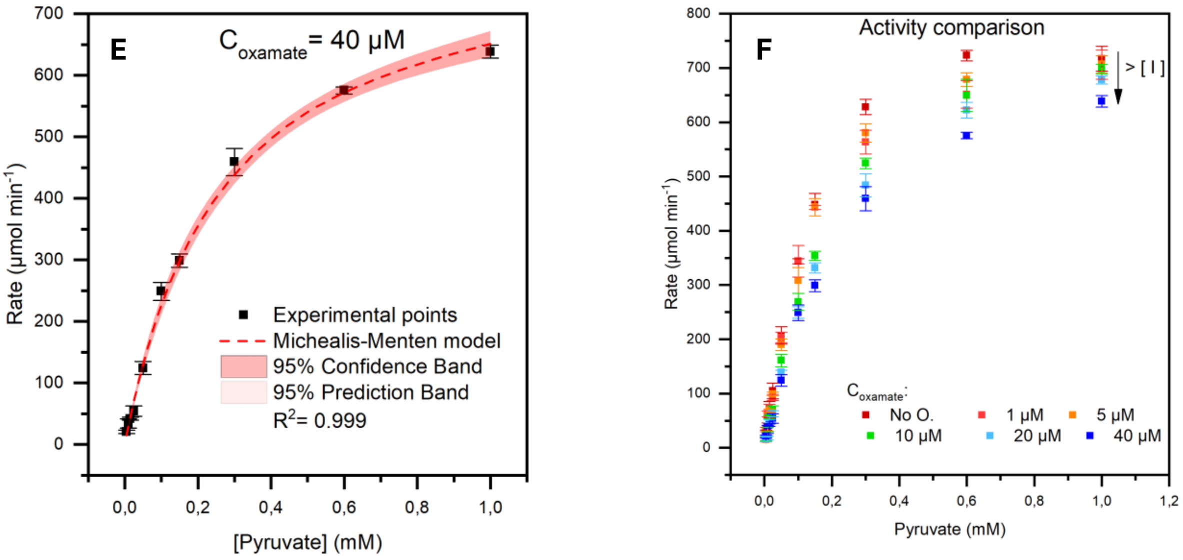

Figure 61. Kinetic results using Oxamate inhibitor.

Figure 61 presents the LDH kinetic curves obtained with pyruvate as the variable substrate, in the presence of increasing Oxamate concentrations. The experimental data were fitted using the Michaelis-Menten model, yielding high-quality fits across all the tested concentrations.

Figure 61F compares the enzyme activity at various inhibitor concentrations, revealing that the curves follow a consistent trajectory and appear to approach comparable saturation values, indicating that Vmax remains unaffected by the presence of Oxamate.

Table 30. Summary of the kinetic parameters in presence of Oxamate inhibitor, obtained with OriginPro.

	PYRUVATE KINETIC PARAMETERS		
$C_{Oxamate}$ [µM]	**V_{max} [µmol min^{-1}]**	**K_m [mM]**	**R^2**
No Oxamate	861 ± 5	0.147 ± 0.004	0.998
1	877 ± 25	0.153 ± 0.008	0.993
5	904 ± 17	0.205 ± 0.008	0.986
10	860 ± 14	0.215 ± 0.009	0.998
20	863 ± 13	0.259 ± 0.009	0.997
40	822 ± 15	0.263 ± 0.013	0.999

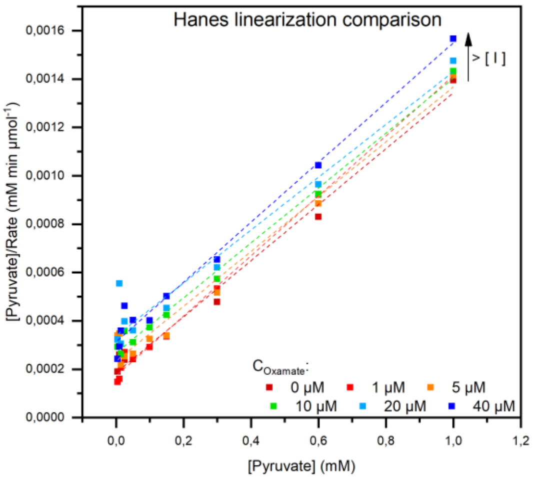

Figure 62. Hanes-Woolf linearization.

Table 31. Summary of the kinetic parameters in presence of Oxamate inhibitor, obtained with Hanes-Woolf linearization.

	PYRUVATE KINETIC PARAMETERS		
	Hanes-Woolf		
$C_{Oxamate}$ [µM]	**V_{max} [µmol min^{-1}]**	**K_m [mM]**	**R^2**
No Oxamate	864	0.160	0.989
1	807	0.140	0.995
5	883	0.207	0.974
10	881	0.236	0.993
20	916	0.310	0.948
40	809	0.253	0.982

The parameters presented in Table 30 and Table 31, obtained respectively through OriginPro non-linear regression and via Hanes-Woolf linearization shown in Figure 62, confirm the previous observations: the V_{max} value remained essentially constant, regardless Oxamate concentration, whereas the K_m values showed a gradual increase.

The values across both tables were consistent, with the exception of the 20 μM data point, which appeared slightly higher when analyzed using Hanes-Woolf linearization. This minor inconsistency likely the lower goodness of fit at this concentration and the increased sensitivity of linearization methods to experimental variability.

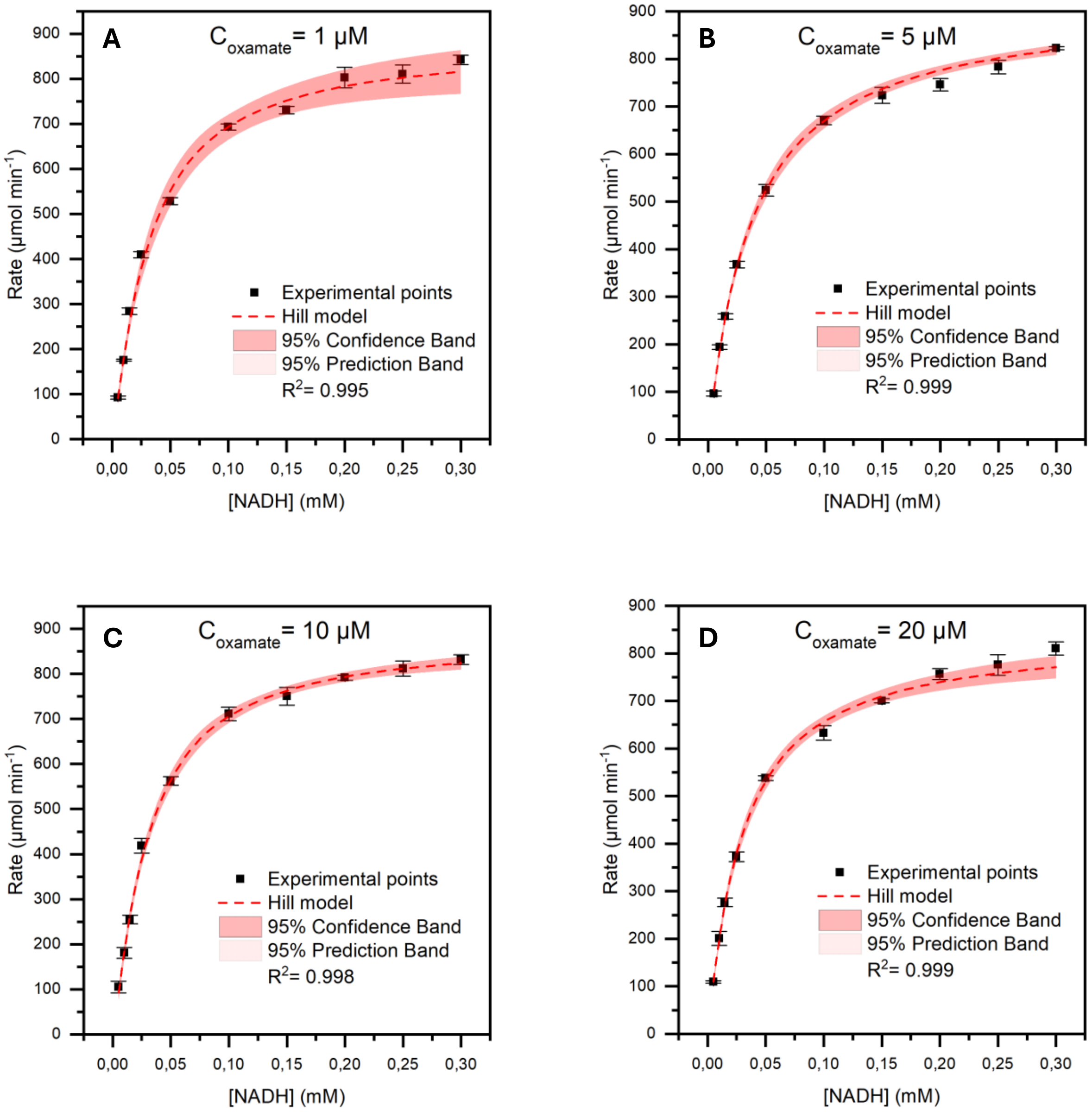

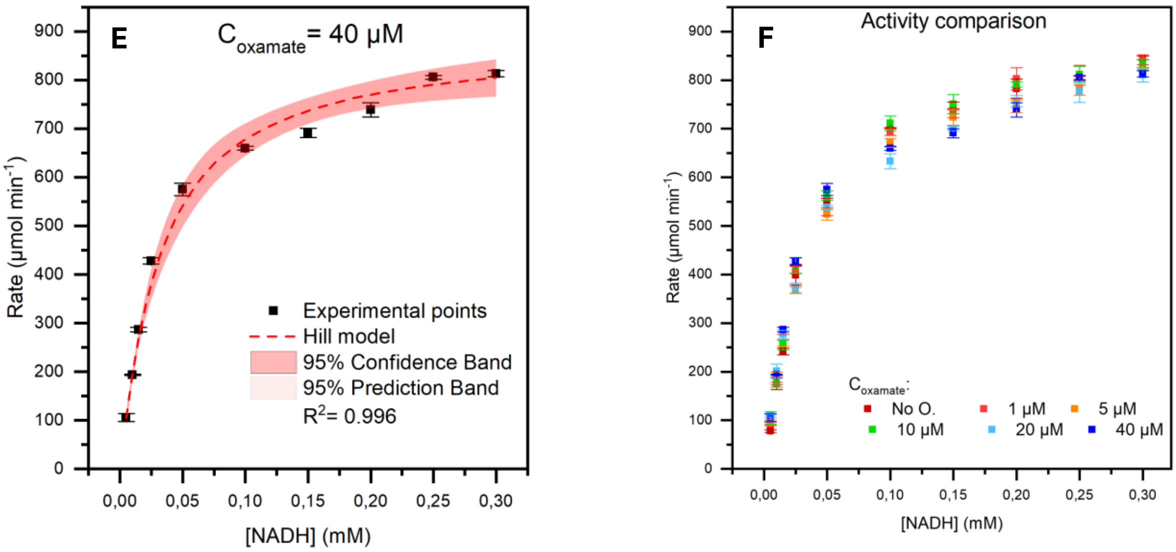

Figure 63. Kinetic results using Oxamate inhibitor.

Figure 63 depicts the LDH activity as a function of cofactor concentration. The experimental data were fitted to a Hill model, yielding good results as indicated by the high goodness of fit. The comparison of activities in Figure 63F suggests that increasing Oxamate concentrations did not significantly alter the shape or saturation behaviour of the curves.

Table 32. Summary of the kinetic parameters in presence of Oxamate inhibitor.

	NADH KINETIC PARAMETERS			
$C_{Oxamate}$ [μM]	**V_{max} [μmol min^{-1}]**	**K_m [mM]**	**n**	**R^2**
No Oxamate	891 ± 6	0.034 ± 0.001	1.21 ± 0.02	0.999
1	875 ± 12	0.032 ± 0.001	1.16 ± 0.03	0.995
5	919 ± 12	0.038 ± 0.002	1.02 ± 0.03	0.999
10	880 ± 14	0.031 ± 0.001	1.18 ± 0.05	0.998
20	839 ± 12	0.030 ± 0.001	1.06 ± 0.02	0.999
40	878 ± 9	0.032 ± 0.001	1.07 ± 0.02	0.996

Table 32 further summarizes the kinetic parameters derived from the preceding curves, obtained through a non-linear regression performed with OriginPro software. A slight decrease in V_{max} values was observed, with no meaningful change in K_m or Hill coefficient. The cooperativity parameter remains quite stable across all inhibitor concentrations, suggesting that Oxamate does not impact the enzyme's allosteric regulation with respect to NADH binding.

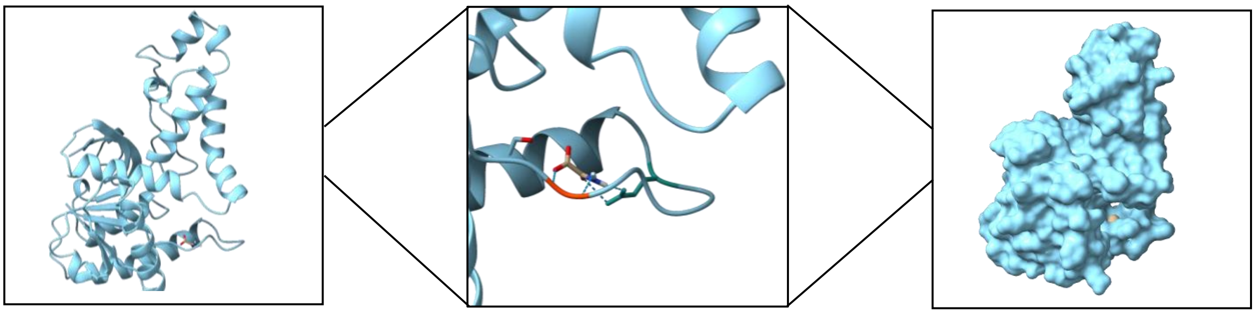

Figure 64. ChimeraX views of the binding between LDH and Oxamate.

Molecular docking results, presented in Figure 64, demonstrated the interactions between Oxamate and LDH. It forms two hydrogen bonds with the Methionine 53 (orange) and two with the Glutamine 59 (water green) residue, within LDH active site.

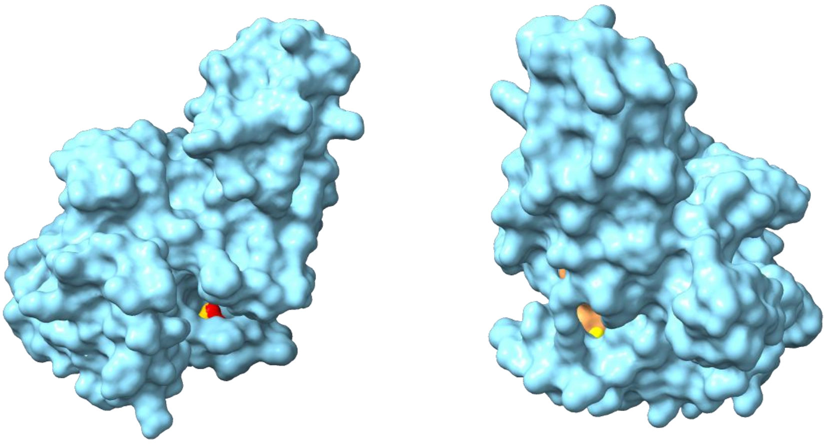

Figure 65. ChimeraX visual representation of LDH's surface with Oxamate, NADH and pyruvate binding.

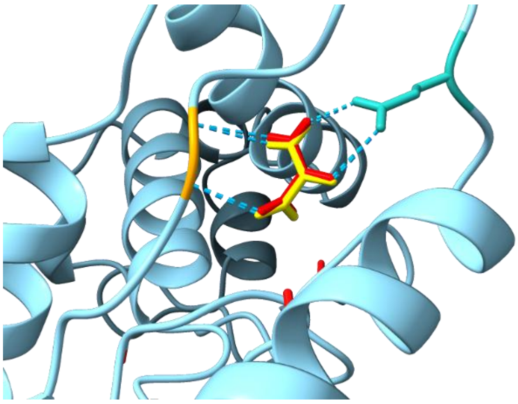

Figure 66. Enlarged view of the binding of pyruvate and Oxamate with LDH; obtained with ChimeraX.

Figure 65 presents a surface view illustrating the binding interactions of Oxamate (light yellow) with both pyruvate (red) and NADH (sandy brown) within the active site of LDH. Notably, the surface of Oxamate is observed to overlap partially with that of pyruvate (red), suggesting direct competition for the binding.

Furthermore, the binding residues for pyruvate (Methionine 53 and Glutamine 59) were identical to those involved in this interaction, as confirmed by Figure 66. This structural evidence suggested a competitive inhibition mechanism, with respect to pyruvate, which was confirmed by the kinetic parameters in Table 24, where V_{max} remains constant while K_m increases [15].

Regarding the interactions with the cofactor, despite its binding to the active site, Oxamate did not interfere with NADH binding. Kinetic data corroborated this, showing a slightly decrease of V_{max} and unchanged K_m, which is characteristic of a non-competitive inhibition mechanism towards NADH [15]. This suggests that Oxamate's inhibitory effect is substrate-specific and does not extend to NADH binding dynamics.

Table 33. Summary of the identified mechanism of inhibition and the correspond values of Ki.

	Pyruvate	NADH
Inhibition mechanism	Competitive	Non-competitive
Ki [µM] (Analytical)	13 – 51	0 – 2702
Ki [µM] (GraphPad Prism)	39	704

Table 33 presents the K_i values determined following the identification of the inhibition type. The range calculated by the analytical method and the value obtained from non-linear regression demonstrate good agreement.

Furthermore, it is important to note that the K_i value is considerably elevated when the kinetic curve is analyzed as a function of NADH concentration. This observation is attributed to the inhibitor's competitive interaction with pyruvate, rather than with NADH. As a result, a lower concentration of inhibitor is sufficient to elicit an effect when pyruvate is the varied substrate, whereas a higher concentration is required to observe inhibition when varying NADH. This is also due to the fact that, in the experiments where NADH concentration was varied, pyruvate was present at 1.63 mM, a concentration that is high enough to limit the inhibitory effect of the tested Oxamate concentrations.

3.2.4.6 Summary of the inhibition mechanisms

Table 34. Summary of the inhibition mechanism and the correspondent K_i.

PYRUVATE			
Inhibitor	Inhibition mechanism	Ki [µM] (Analytical)	Ki [µM] (GraphPad)
Galloflavin	Mixed	5 – 18	16
FX-11	Non-competitive	15 – 37	18
Gossypol	Mixed	4 – 44	10
NHI-2	Mixed	0 – 187	148
Oxamate	Competitive	13 – 51	39

Table 35. Summary of the inhibition mechanism and the correspondent K_i.

NADH			
Inhibitor	Inhibition mechanism	Ki [μM] (Analytical)	Ki [μM] (GraphPad)
Galloflavin	Non-competitive	55 – 195	140
FX-11	Mixed	28 – 45	31
Gossypol	Mixed/Competitive	0.14 – 10 / 0.45 – 7	4.92/1.36
NHI-2	Non-competitive	3 – 88	15
Oxamate	Non-competitive	54 – 2702	704

Tables 34 and 35 provide an overview of the inhibition mechanism identified for each tested compound, along with their corresponding inhibition constants, evaluated with pyruvate and NADH as variable substrate respectively. The data revealed diverse inhibition types: Galloflavin and Gossypol, as well as NHI-2, exhibited mixed-type inhibition with respect to pyruvate, while FX-11 behaved non-competitively and Oxamate competitively, consistently with its structural mimicry of pyruvate.

Concerning NADH, Galloflavin and NHI-2 showed non-competitive inhibition, FX-11 mixed-type and Gossypol presented a complex behaviour. Notably, the K_i values for Gossypol were evaluated considering both a mixed-type inhibition, which is supported by experimental kinetic data, and a competitive inhibition model, as suggested by molecular dynamics studies. Oxamate demonstrated a predominantly non-competitive mechanism with respect to NADH.

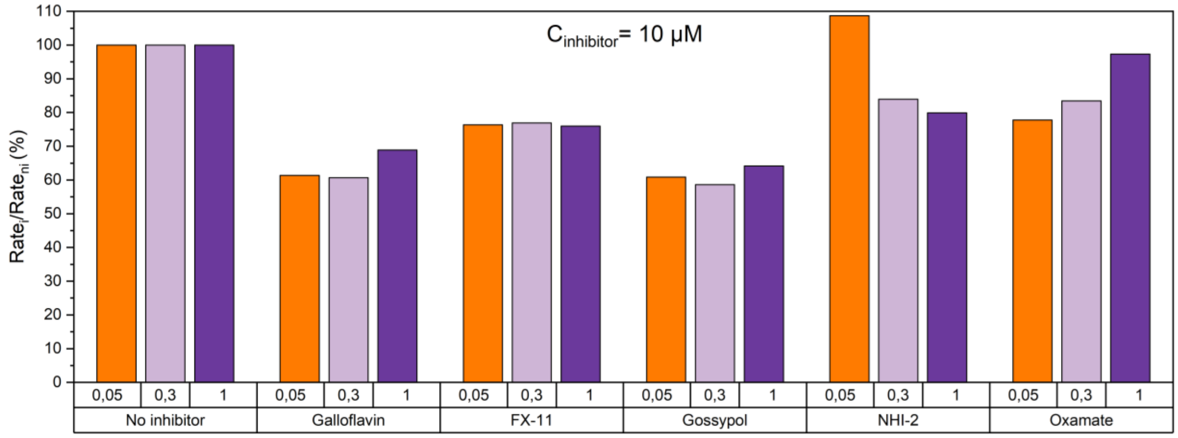

Figure 68. Bar graph of the percentage of inhibition of the compounds tested, having a concentration of 10 μM.

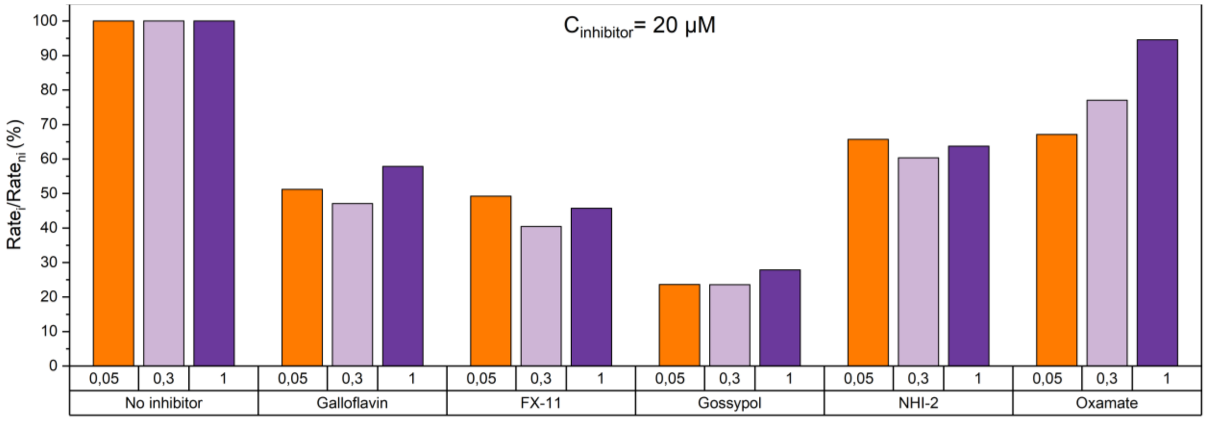

Figure 67. Bar graph of the percentage of inhibition of the compounds tested, having a concentration of 20 μM.

Figures 67 and 68 illustrate the percentage of inhibition exerted by each tested compound across various pyruvate concentrations. Three representative pyruvate concentrations were selected to reflect the overall trend of the kinetic curve. The bar plots were generated using two inhibitor concentrations that were employed across all tested compounds.

Notably, in Figure 67, the bar for NHI-2 at 0.05 mM exceeds that of the uninhibited control, potentially suggesting an activation mechanism. However, this value is more likely attributable to interference from NHI-2 during the measurements, particularly given its strong absorbance at 340 nm.

Galloflavin, FX-11, and Gossypol demonstrated superior inhibitory potential, as indicated by their greater deviation from the uninhibited control. To select the most promising candidate, reliance on existing literature data is warranted. As previously reported in the "Introduction" section, while FX-11 demonstrates some therapeutic potential, its highly reactive catechol moiety limits its suitability for further drug development. Furthermore, while Gossypol exhibits efficacy, it is also associated with notable cytotoxicity towards normal cells. In contrast, Galloflavin demonstrates negligible effects on non-cancerous cellular metabolism, positioning it as the most favourable candidate among those evaluated.

3.3 Incubation results

3.3.1 Thermal inactivation

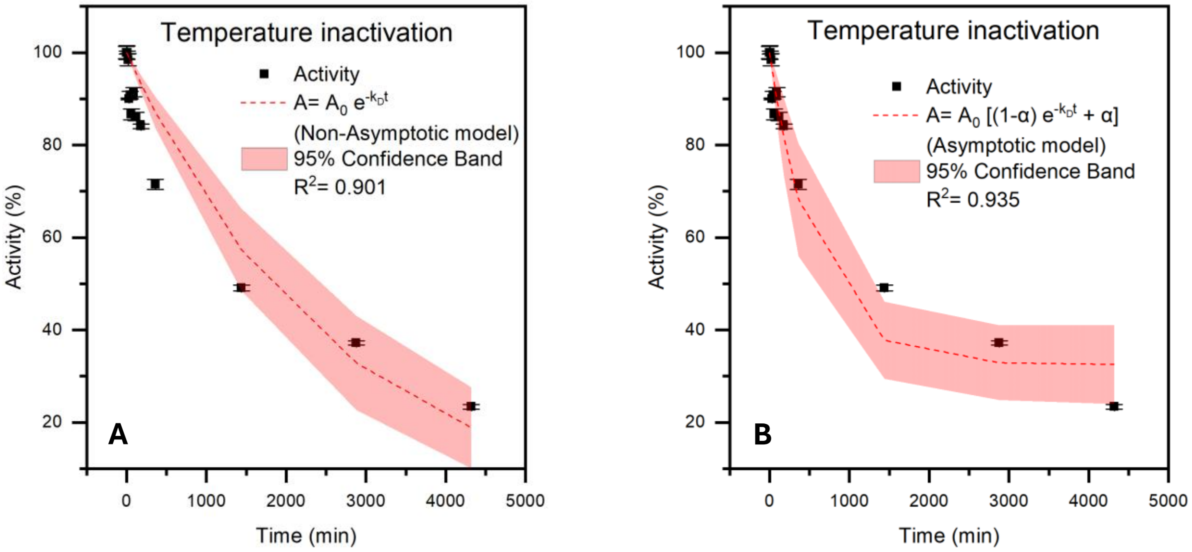

Figure 69. Graphical representation of the non-asymptotic and from the asymptotic model of thermal inactivation.

The experimental data from the incubation test at 37°C temperature are displayed in Figure 69. These measurements were fitted to two distinct models of enzyme thermal inactivation: a non-asymptotic and an asymptotic model.

Table 36. Parameters derived from the non-asymptotic and from the asymptotic model of thermal inactivation.

	Non-Asymptotic model		Asymptotic model		
Parameters	k_D [min^{-1}]	$t_{1/2}$ [min]	k_D [min^{-1}]	α [-]	$t_{1/2}$ [min]
Value	0.00034	1733	0.00177	0.325	763

Table 36 reports the parameters obtained from both models, including the rate constant of inactivation (k_D), the half-life time ($t_{1/2}$), which represent the time at which enzyme activity is halved, and the asymptote parameter (α) for the asymptotic model. Experimentally, as can be seen from Figure 69, approximately 49% of the enzyme activity was retained after 1440 minutes. When comparing this value to the half-life time estimated, the $t_{1/2}$ derived from the non-asymptotic model provides a better representation of the experimental decay.

Although the asymptotic model yielded a slightly better overall fit, as shown in Figure 69B, visual inspection of the latter time points of the curve suggests a continuous decline in the activity, rather than a stabilization at an asymptote. Therefore, the non-asymptotic model is considered more appropriate to describe the thermal inactivation process observed under the tested conditions.

3.3.2 DMSO inactivation

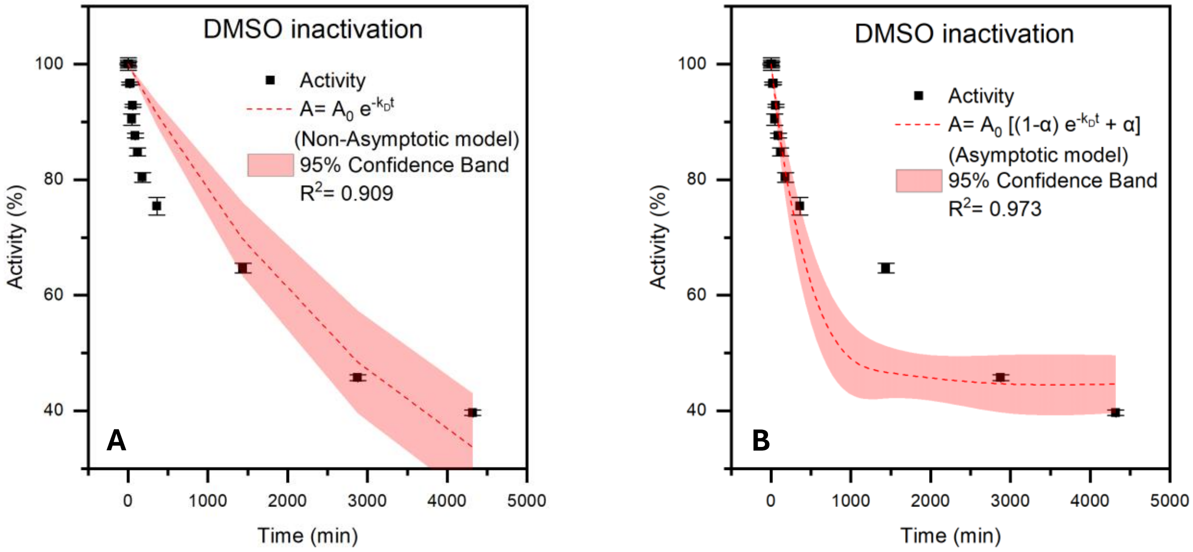

Figure 70. Graphical representation of the non-asymptotic and from the asymptotic model of thermal inactivation.

Figure 70 illustrates the experimental data, describing enzyme activity decay, obtained during incubation with 0.3% v/v DMSO. Similarly to the thermal inactivation data, the activity measurements were fitted using both non-asymptotic and asymptotic inactivation models.

Table 37. Parameters derived from the non-asymptotic and from the asymptotic model of thermal inactivation.

	Non-Asymptotic model		Asymptotic model		
Parameters	k_D [min^{-1}]	$t_{1/2}$ [min]	k_D [min^{-1}]	α [-]	$t_{1/2}$ [min]
Value	0.00026	2754	0.00228	0.446	1021

Table 21 summarizes the parameters derived from the respective models, along with their calculated $t_{1/2}$ values. The experimental data show that enzyme activity decreased from 65% to 46% between 1440 and 2880 minutes. Given this, the $t_{1/2}$ from the non-asymptotic model appears to better capture the experimental behaviour, consistently with the thermal inactivation behaviour. Additionally, the continuous decrease in the enzyme activity in the final portion of the curve contradicts the asymptotic assumption of activity stabilization. Hence, the non-asymptotic model is again favoured as the more accurate description of LDH inactivation in the presence of DMSO.

The better description provided by the non-asymptotic model in both thermal and DMSO inactivation cases suggests that LDH activity does not reach a plateau during the considered incubation times, but rather continues to decline. This indicates a progressive loss of enzyme function without a significant residual active fraction stabilizing over time. The observed half-life values also underscore the relative stability of LDH under both conditions, with longer half-lives in the presence of DMSO. This last finding suggests that the tested concentration of DMSO does not compromise LDH activity over prolonged incubation period at 37°C, as partially showed also by kinetic evaluations. However, it cannot be concluded that DMSO exerts a stabilizing effect on LDH thermal inactivation without further investigations.

4. Conclusions and future developments

The primary objective of this Master's thesis was to conduct a comprehensive kinetic characterization of the enzyme LDH, both in its uninhibited state and in the presence of selected and well-known inhibitors. This research aimed to establish a solid foundation for the development of an LDH-based biosensor for anticancer drug screening. All analyses were performed using UV-vis spectrophotometry. The specific inhibitors studied were: Galloflavin, FX-11, Gossypol, NHI-2, and Oxamate. Complementary experiments involving temperature and DMSO incubation, alongside molecular docking studies, further completed the investigation.

Initially, the absorbance spectra of all the involved compounds were recorded to identify the optimal wavelength for subsequent kinetic assays. A wavelength of 340 nm was selected, as NADH exhibited a distinct absorption peak at this point, free from interference by pyruvate, NAD+, or lactate.

Subsequently, the absorption spectra of DMSO and the inhibitors were also determined. All the spectra did not give a remarkable signal at 340 nm, with the exception of NHI-2. Its contribution was elevated, prompting further investigation at lower NADH concentrations to assess its potential interference. It was observed that at reduced NADH concentrations, the contribution of NHI-2 to the total absorbance even surpassed that of NADH itself. This observed interference was carefully accounted for in all subsequent kinetic analyses.

Kinetic assays were performed to evaluate enzyme activity. UV-vis measurements were conducted at 340 nm, generating absorbance-versus-time curves. The initial linear slope of these curves was used to determine the reaction rate. Kinetic curves were then constructed by measuring reaction rates across increasing concentrations of either substrate (pyruvate) or cofactor (NADH), while keeping the other component at a fixed concentration. This approach allowed for the extrapolation of Vmax and Km values, which are critical for characterizing the kinetic behaviour of LDH and assessing the impact of inhibitors.

For pyruvate-dependent assay, an apparent V_{max} of 861 µmol min^{-1} and an apparent K_m of 0.147 mM were obtained. Furthermore, assays conducted at various fixed NADH concentrations yielded true kinetic parameters, with a V_{max} of 833 µmol min^{-1} and K_m of 0.117 mM. The influence of DMSO, used as the solvent for inhibitor solubilization, on LDH kinetic behaviour was assessed as well. Results indicated no discernible effect of DMSO on LDH kinetics.

Kinetic assays were also conducted with increasing concentrations of pyruvate in the presence of varying inhibitor concentrations. These experiments allowed for the determination of V_{max} and K_m at increasing inhibitor concentrations. Analysis of the changes in these parameters, complemented by molecular docking simulations, elucidated the inhibition mechanism for each compound. Following the identification of the inhibition type, K_i was calculated to provide a quantitative measure of the inhibitory potential of each compound. Galloflavin, Gossypol, and NHI-2 were found to exhibit mixed-type mechanism of inhibition, while Oxamate displayed competitive behaviour and FX-11 showed non-competitive inhibition. It is important to note that the results for NHI-2 should be interpreted with caution due to its absorbance interference.

Complementary assays were performed with increasing NADH concentrations. For uninhibited LDH, an apparent V_{max} of 891 µmol min^{-1} and an apparent K_m of 0.034 mM. Furthermore, assays at various fixed pyruvate concentrations yielded the identification of the true kinetic parameters. V_{max} was equal to 847 µmol min^{-1}, while K_m was equal to 0.028 mM. Consistent with the pyruvate-dependent assays, DMSO exhibited no influence on the kinetic parameters when NADH concentration was varied.

Kinetic tests function of NADH concentration and at different inhibitors concentration were then conducted. Coupled with molecular docking simulations, these studies facilitated the elucidation of each compound's inhibition mechanism. NHI-2 and Oxamate demonstrated non-competitive inhibition. Given the previously observed high absorbance contribution of NHI-2 at low NADH concentrations, its results warrant careful consideration. FX-11 displayed mixed-type inhibition. Interestingly, for Gossypol, a discrepancy was noted: molecular docking suggested competitive inhibition, whereas kinetic analyses indicated mixed-type inhibition. This disparity might be resolved by exploring a broader range of NADH concentrations; however, spectrophotometer signal saturation precluded testing beyond the maximum NADH concentration.

Molecular modelling studies also revealed that Serine 50 was a key residue involved in the binding of four out of five inhibitors to LDH. This suggests the potential importance of Serine 50 in the LDH structure. However, the confirmation of this hypothesis requires further experimental validation.

To complete the characterization of LDH, temperature and DMSO incubation tests were performed. These experiments aimed to determine the residual enzyme activity over time, a critical aspect given LDH's potential application in a biosensor requiring long-term stability. They confirmed no harmful effect of DMSO at the tested concentration on LDH, but relatively small half-life period of the enzyme when used in its free form.

The future perspective of this research involves using the detailed kinetic profile of the free enzyme as a reference. This reference will be crucial for comparison with the behaviour of immobilized LDH, as enzyme immobilization is a key component of the proposed anticancer drug screening biosensor. The immobilization could represent an efficient and effective strategy to enable enzyme reuse over extended periods. By improving enzyme stability, immobilization is expected to increase the enzyme's half-life, thereby enhancing the durability and practicality of the proposed biosensor for long-term anticancer drug screening applications. Such comparative data will enable an assessment of the impact of immobilization on enzyme kinetics, thereby determining the reliability of the chosen method and whether it excessively alters enzyme behaviour.

The methods employed for LDH characterization are reliable, easy to use, non-destructive, and cost-effective. Moreover, the comprehensive kinetic characterization, supported by molecular docking insights, provides a robust framework to understand the inhibitory effects of these compounds on LDH activity and their potential therapeutic applications. Nevertheless, these methods proved insufficient in certain instances, such as the previously discussed cases of NHI-2 and Gossypol. Therefore, future investigations should be complemented by structural studies of the enzyme-inhibitor complex, such as X-ray crystallography. Despite these limitations, it can be concluded that these studies provide a strong foundational reference for the subsequent development of the biosensor prototype.

Bibliography

[1] "Cancer Tomorrow." Accessed: Apr. 24, 2025. [Online]. Available: https://gco.iarc.fr/tomorrow/en/dataviz/isotype

[2] E. Bidram *et al.*, "A concise review on cancer treatment methods and delivery systems," *J Drug Deliv Sci Technol*, vol. 54, p. 101350, Dec. 2019, doi: 10.1016/J.JDDST.2019.101350.

[3] B. Liu, H. Zhou, L. Tan, K. T. H. Siu, and X. Y. Guan, "Exploring treatment options in cancer: tumor treatment strategies," *Signal Transduction and Targeted Therapy 2024 9:1*, vol. 9, no. 1, pp. 1–44, Jul. 2024, doi: 10.1038/s41392-024-01856-7.

[4] "Types of Cancer Treatment - NCI." Accessed: May 10, 2025. [Online]. Available: https://www.cancer.gov/about-cancer/treatment/types

[5] M. V. Liberti and J. W. Locasale, "The Warburg Effect: How Does it Benefit Cancer Cells?," *Trends Biochem Sci*, vol. 41, no. 3, p. 211, Mar. 2016, doi: 10.1016/J.TIBS.2015.12.001.

[6] H. Yao, F. Yang, and Y. Li, "Natural products targeting human lactate dehydrogenases for cancer therapy: A mini review," *Front Chem*, vol. 10, p. 1013670, Sep. 2022, doi: 10.3389/FCHEM.2022.1013670/BIBTEX.

[7] F. Jafary, M. R. Ganjalikhany, A. Moradi, M. Hemati, and S. Jafari, "Novel Peptide Inhibitors for Lactate Dehydrogenase A (LDHA): A Survey to Inhibit LDHA Activity via Disruption of Protein-Protein Interaction," *Sci Rep*, vol. 9, no. 1, Dec. 2019, doi: 10.1038/s41598-019-38854-7.

[8] M. L. Habte, E. A. Beyene, M. L. Habte, and E. A. Beyene, "Biological Application and Disease of Oxidoreductase Enzymes," *Oxidoreductase*, Sep. 2020, doi: 10.5772/INTECHOPEN.93328.

[9] R. Chaudhry and M. A. Varacallo, "Biochemistry, Glycolysis," *StatPearls*, Aug. 2023, Accessed: Jun. 23, 2025. [Online]. Available: https://www.ncbi.nlm.nih.gov/books/NBK482303/

[10] X. Chen, S. Li, and L. Liu, "Engineering redox balance through cofactor systems," *Trends Biotechnol*, vol. 32, no. 6, pp. 337–343, Jun. 2014, doi: 10.1016/J.TIBTECH.2014.04.003/ASSET/81AD2C07-DCAD-4E1B-8F1D-700652A50E5D/MAIN.ASSETS/GR2.SML.

[11] A. Farhana and S. L. Lappin, "Biochemistry, Lactate Dehydrogenase," *StatPearls*, May 2023, Accessed: Apr. 24, 2025. [Online]. Available: https://www.ncbi.nlm.nih.gov/books/NBK557536/

[12] W. Al Tameemi, T. P. Dale, R. M. K. Al-Jumaily, and N. R. Forsyth, "Hypoxia-Modified Cancer Cell Metabolism," *Front Cell Dev Biol*, vol. 7, p. 426290, Jan. 2019, doi: 10.3389/FCELL.2019.00004/XML/NLM.

[13] Y. Feng, Y. Xiong, T. Qiao, X. Li, L. Jia, and Y. Han, "Lactate dehydrogenase A: A key player in carcinogenesis and potential target in cancer therapy," Dec. 01, 2018, *Blackwell Publishing Ltd*. doi: 10.1002/cam4.1820.

[14] "8.7: Enzyme Inhibition - Chemistry LibreTexts." Accessed: Apr. 24, 2025. [Online]. Available: https://chem.libretexts.org/Courses/Georgia_Southern_University/CHEM_1152%3A_Survey_of_Chemistry_II_(Osborne)/08%3A_Proteins/8.07%3A_Enzyme_Inhibition

[15] A. Illanes, "Enzyme biocatalysis: Principles and applications," *Enzyme Biocatalysis: Principles and Applications*, pp. 1–391, 2008, doi: 10.1007/978-1-4020-8361-7/COVER.

[16] M. Manerba *et al.*, “Galloflavin (CAS 568-80-9): A Novel Inhibitor of Lactate Dehydrogenase,” *ChemMedChem*, vol. 7, no. 2, pp. 311–317, Feb. 2012, doi: 10.1002/CMDC.201100471,.

[17] F. Farabegoli, M. Vettraino, M. Manerba, L. Fiume, M. Roberti, and G. Di Stefano, “Galloflavin, a new lactate dehydrogenase inhibitor, induces the death of human breast cancer cells with different glycolytic attitude by affecting distinct signaling pathways,” *European Journal of Pharmaceutical Sciences*, vol. 47, no. 4, pp. 729–738, Nov. 2012, doi: 10.1016/J.EJPS.2012.08.012.

[18] M. A. Altinoz and A. Ozpinar, “Oxamate targeting aggressive cancers with special emphasis to brain tumors,” *Biomedicine & Pharmacotherapy*, vol. 147, p. 112686, Mar. 2022, doi: 10.1016/J.BIOPHA.2022.112686.

[19] J. L. Judge *et al.*, “The Lactate Dehydrogenase Inhibitor Gossypol Inhibits Radiation-Induced Pulmonary Fibrosis,” *Radiat Res*, vol. 188, no. 1, p. 35, Jul. 2017, doi: 10.1667/RR14620.1.

[20] M. S. Ha *et al.*, “Structural basis of lactate dehydrogenase A-gossypol complex,” *Biochem Biophys Res Commun*, vol. 733, p. 150721, Nov. 2024, doi: 10.1016/J.BBRC.2024.150721.

[21] E. J. Rellinger *et al.*, “FX11 inhibits aerobic glycolysis and growth of neuroblastoma cells,” *Surgery*, vol. 161, no. 3, pp. 747–752, Mar. 2017, doi: 10.1016/J.SURG.2016.09.009.

[22] S. Daniele *et al.*, “Lactate dehydrogenase-A inhibition induces human glioblastoma multiforme stem cell differentiation and death,” *Scientific Reports 2015 5:1*, vol. 5, no. 1, pp. 1–17, Oct. 2015, doi: 10.1038/srep15556.

[23] “Spectrophotometric Enzyme Assays - Creative Enzymes.” Accessed: Apr. 28, 2025. [Online]. Available: https://www.creative-enzymes.com/resource/spectrophotometric-enzyme-assays_5.html

[24] “29.9: The Michaelis-Menten Mechanism for Enzyme Catalysis - Chemistry LibreTexts.” Accessed: Jun. 27, 2025. [Online]. Available: https://chem.libretexts.org/Bookshelves/Physical_and_Theoretical_Chemistry_Textbook_Maps/Physical_Chemistry_(LibreTexts)/29%3A_Chemical_Kinetics_II-_Reaction_Mechanisms/29.09%3A_The_Michaelis-Menten_Mechanism_for_Enzyme_Catalysis

[25] S. Goutelle *et al.*, “The Hill equation: A review of its capabilities in pharmacological modelling,” *Fundam Clin Pharmacol*, vol. 22, no. 6, pp. 633–648, Dec. 2008, doi: 10.1111/J.1472-8206.2008.00633.X;PAGE:STRING:ARTICLE/CHAPTER.

[26] “10.5: Enzyme Inhibition - Chemistry LibreTexts.” Accessed: Jun. 28, 2025. [Online]. Available: https://chem.libretexts.org/Bookshelves/Physical_and_Theoretical_Chemistry_Textbook_Maps/Map%3A_Physical_Chemistry_for_the_Biosciences_(Chang)/10%3A_Enzyme_Kinetics/10.05%3A_Enzyme_Inhibition

[27] X. Yang *et al.*, “Classification of difference between inhibition constants of an inhibitor to facilitate identifying the inhibition type,” *J Enzyme Inhib Med Chem*, vol. 28, no. 1, pp. 205–213, Feb. 2013, doi: 10.3109/14756366.2011.645240;SUBPAGE:STRING:FULL.

[28] “Understanding the Drug Discovery Pipeline.” Accessed: Jul. 01, 2025. [Online]. Available: https://delta4.ai/drug-discovery-pipeline/

[29] T. I. Adelusi *et al.*, “Molecular modeling in drug discovery,” *Inform Med Unlocked*, vol. 29, p. 100880, Jan. 2022, doi: 10.1016/J.IMU.2022.100880.

[30] G. Yalcin-Ozkat, “Molecular Modeling Strategies of Cancer Multidrug Resistance,” *Drug Resistance Updates*, vol. 59, Dec. 2021, doi: 10.1016/j.drup.2021.100789.

[31] P. C. Agu *et al.*, “Molecular docking as a tool for the discovery of molecular targets of nutraceuticals in diseases management,” *Sci Rep*, vol. 13, no. 1, pp. 1–18, Dec. 2023, doi: 10.1038/S41598-023-40160-2;SUBJMETA=154,433,555,556,631;KWRD=PHARMACEUTICS,TARGET+IDENTIFICATION,TARGET+VALIDATION.

[32] D. R. Silva, J. de C. O. Sardi, I. A. Freires, A. C. B. Silva, and P. L. Rosalen, “In silico approaches for screening molecular targets in Candida albicans: A proteomic insight into drug discovery and development,” *Eur J Pharmacol*, vol. 842, pp. 64–69, Jan. 2019, doi: 10.1016/J.EJPHAR.2018.10.016.

[33] “Difference between Molecular Docking and Molecular Dynamics Simulation - Creative Proteomics.” Accessed: Jun. 30, 2025. [Online]. Available: https://www.iaanalysis.com/molecular-dynamics-simulation-docking-difference.html

[34] U. Jain *et al.*, “Emerging vistas on pesticides detection based on electrochemical biosensors – An update,” *Food Chem*, vol. 371, p. 131126, Mar. 2022, doi: 10.1016/J.FOODCHEM.2021.131126.

[35] N. Bhalla, P. Jolly, N. Formisano, and P. Estrela, “Introduction to biosensors,” *Essays Biochem*, vol. 60, no. 1, p. 1, Jun. 2016, doi: 10.1042/EBC20150001.

[36] C. Cocuzza, E. Antoniono, C. Ottone, V. Cauda, D. Fino, and M. Piumetti, “Preparation of a Mesoporous Biosensor for Human Lactate Dehydrogenase for Potential Anticancer Inhibitor Screening,” *ACS Biomater Sci Eng*, vol. 9, no. 11, pp. 6045–6057, Nov. 2023, doi: 10.1021/ACSBIOMATERIALS.3C00582/ASSET/IMAGES/LARGE/AB3C00582_0013.JPEG.

[37] G. Cheng, Z. Pi, Z. Zheng, S. Liu, Z. Liu, and F. Song, “Magnetic nanoparticles-based lactate dehydrogenase microreactor as a drug discovery tool for rapid screening inhibitors from natural products,” *Talanta*, vol. 209, p. 120554, Mar. 2020, doi: 10.1016/J.TALANTA.2019.120554.

[38] Y. Zhou *et al.*, “Development of novel human lactate dehydrogenase A inhibitors: High-throughput screening, synthesis, and biological evaluations,” *Eur J Med Chem*, vol. 177, pp. 105–115, Sep. 2019, doi: 10.1016/J.EJMECH.2019.05.033.

[39] “UV-Vis Absorption Spectroscopy - Theory.” Accessed: Jul. 06, 2025. [Online]. Available: https://teaching.shu.ac.uk/hwb/chemistry/tutorials/molspec/uvvisab1.htm

[40] “UV-Vis Spectroscopy: Principle, Strengths and Limitations and Applications | Technology Networks.” Accessed: Jul. 02, 2025. [Online]. Available: https://www.technologynetworks.com/analysis/articles/uv-vis-spectroscopy-principle-strengths-and-limitations-and-applications-349865

[41] “Potassium Phosphate (pH 5.8 to 8.0) Preparation and Recipe | AAT Bioquest.” Accessed: Apr. 28, 2025. [Online]. Available: https://www.aatbio.com/resources/buffer-preparations-and-recipes/potassium-phosphate-ph-5-8-to-8-0

[42] C. Cocuzza, E. Antoniono, C. Ottone, V. Cauda, D. Fino, and M. Piumetti, “Preparation of a Mesoporous Biosensor for Human Lactate Dehydrogenase for Potential Anticancer Inhibitor Screening,” *ACS Biomater Sci Eng*, vol. 9, no. 11, pp. 6045–6057, Nov. 2023, doi: 10.1021/acsbiomaterials.3c00582.

[43] C. Cocuzza *et al.*, “Synthesis and characterization of mesoporous silicas with dendritic and spongy-like structures: Potential supports for human lactate dehydrogenase-based microreactors aimed at anticancer inhibitor screening,” *Microporous and Mesoporous Materials*, vol. 376, p. 113182, Aug. 2024, doi: 10.1016/J.MICROMESO.2024.113182.

[44] J. R. E. T. Pineda, R. Callender, and S. D. Schwartz, “Ligand Binding and Protein Dynamics in Lactate Dehydrogenase,” *Biophys J*, vol. 93, no. 5, p. 1474, 2007, doi: 10.1529/BIOPHYSJ.107.106146.

[45] K. Tomohara *et al.*, “DMSO-Perturbing Assay for Identifying Promiscuous Enzyme Inhibitors,” *ACS Med Chem Lett*, vol. 10, no. 6, pp. 923–928, Jun. 2019, doi: 10.1021/ACSMEDCHEMLETT.9B00093/SUPPL_FILE/ML9B00093_SI_001.PDF.

[46] “What is an inhibitory constant (Ki) and how does it relate to understanding drug interactions?” Accessed: Jul. 06, 2025. [Online]. Available: https://www.ebmconsult.com/articles/inhibitory-constant-ki-drug-interactions

[47] “GraphPad Prism 10 Curve Fitting Guide - Equation: Mixed-model inhibition.” Accessed: Jul. 07, 2025. [Online]. Available: https://www.graphpad.com/guides/prism/latest/curve-fitting/reg_mixered_model.htm

[48] “UCSF Chimera Home Page.” Accessed: May 31, 2025. [Online]. Available: https://www.cgl.ucsf.edu/chimera/

[49] S. S. Butt, Y. Badshah, M. Shabbir, and M. Rafiq, “Molecular Docking Using Chimera and Autodock Vina Software for Nonbioinformaticians,” *JMIR Bioinform Biotech*, vol. 1, no. 1, p. e14232, 2020, doi: 10.2196/14232.

[50] “AutoDock Vina.” Accessed: May 31, 2025. [Online]. Available: https://vina.scripps.edu/

[51] M. Bugnon *et al.*, “SwissDock 2024: major enhancements for small-molecule docking with Attracting Cavities and AutoDock Vina,” *Nucleic Acids Res*, vol. 52, no. W1, pp. W324–W332, Jul. 2024, doi: 10.1093/NAR/GKAE300.

[52] O. Carugo and S. Pongor, “A normalized root-mean-spuare distance for comparing protein three-dimensional structures,” *Protein Sci*, vol. 10, no. 7, p. 1470, Jul. 2001, doi: 10.1110/PS.690101.

[53] “Dimethyl Sulfoxide for UV, IR, HPLC, GPC.” Accessed: Jul. 09, 2025. [Online]. Available: https://www.itwreagents.com/italy/en/product/dimethyl-sulfoxide-for-uv-ir-hplc-gpc/361954

[54] M. Taniguchi, C. A. LaRocca, J. D. Bernat, and J. S. Lindsey, “Digital Database of Absorption Spectra of Diverse Flavonoids Enables Structural Comparisons and Quantitative Evaluations,” *J Nat Prod*, vol. 86, no. 4, pp. 1087–1119, Apr. 2023, doi: 10.1021/ACS.JNATPROD.2C00720/SUPPL_FILE/NP2C00720_SI_001.PDF.

[55] “Gossypol (BL 193) | Bcl-2 Family Antagonist | MedChemExpress.” Accessed: Jul. 01, 2025. [Online]. Available: https://www.medchemexpress.com/Gossypol.html

[56] “Absorbance and Fluorescence Analysis of NAD and NADH - Chemistry LibreTexts.” Accessed: Jul. 09, 2025. [Online]. Available: https://chem.libretexts.org/Ancillary_Materials/Worksheets/Worksheets%3A_Analytical_Chemistry_II/Absorbance_and_Fluorescence_Analysis_of_NAD_and_NADH

[57] “Hill coefficient - Oxford Reference.” Accessed: Jul. 09, 2025. [Online]. Available: https://www.oxfordreference.com/display/10.1093/acref/9780199549351.001.0001/acref-9780199549351-e-4368

[58] A. A. Khan, K. S. Allemailem, F. A. Alhumaydhi, S. J. T. Gowder, and A. H. Rahmani, “The Biochemical and Clinical Perspectives of Lactate Dehydrogenase: An Enzyme of Active Metabolism,” *Endocr Metab Immune Disord Drug Targets*, vol. 20, no. 6, pp. 855–868, Dec. 2019, doi: 10.2174/1871530320666191230141110.

[59] N. S. Chandel, “Glycolysis,” *Cold Spring Harb Perspect Biol*, vol. 13, no. 5, 2021, doi: 10.1101/CSHPERSPECT.A040535,.

[60] “Galloflavin | Lactate Dehydrogenase Inhibitor | MedChemExpress.” Accessed: Jul. 01, 2025. [Online]. Available: https://www.medchemexpress.com/galloflavin.html?utm_source=google&utm_medium=CPC&utm_campaign=Europe&utm_term=HY-W040118&utm_content=Galloflavin&gad_source=1&gad_campaignid=19967430617&gbraid=0AAAAADnIT_bV1fqjqlAg8SrDhTmqt7c6V&gclid=Cj0KCQjwjo7DBhCrARIsACWauSmEY2yUALy9NBOkMMMbWad0cSmgkbUd7TfkUDQQN5d_WFuyiyf5cecaAhhjEALw_wcB

[61] “Oxamic acid sodium (Sodium oxamate) | LDH-A Inhibitor | MedChemExpress.” Accessed: Jul. 01, 2025. [Online]. Available: https://www.medchemexpress.com/oxamic-acid-sodium.html

[62] “FX-11 (LDHA Inhibitor FX11) | LDHA Inhibitor | MedChemExpress.” Accessed: Jul. 01, 2025. [Online]. Available: https://www.medchemexpress.com/FX-11.html

[63] “NHI-2 | LDHA Inhibitor | MedChemExpress.” Accessed: Jul. 01, 2025. [Online]. Available: https://www.medchemexpress.com/nhi-2.html

[64] J. Zurdo, “Developability assessment as an early de-risking tool for biopharmaceutical development,” *Pharm Bioprocess*, vol. 1, no. 1, pp. 29–50, Apr. 2013, doi: 10.4155/PBP.13.3.